EUMETSAT ECMWF

EUMETSAT Contract Report

EUMETSAT EUM/CO/22/4600002712/SLi

Contract Report to EUMETSAT

Revisiting the Direct Assimilation of Scatterometer ‘Sigma0’ over the Ocean

Final report for EUMETSAT contract no. EUM/CO/22/4600002712/SLi

Saleh Abdalla, Sean Healy,
Giovanna De Chiara and Matthew Chantry

June 2024

Series: EUMETSAT/ECMWF Contract Report Series

A full list of ECMWF Publications can be found on our web site under:

http://www.ecmwf.int/publications/

Contact: library@ecmwf.int

Table of Contents

List of Figures

List of Tables

1. The development of the ANN ASCAT σ^0 Observation Operator (WP 1)

1.1. Background

Precise knowledge of ocean surface roughness is important for a large range of applications, such as the computation of air/sea heat fluxes, assimilation in Numerical Weather Prediction (NWP) systems, for forcing ocean models and surface-wave models, as well as for climate studies.

At ECMWF scatterometer winds have been assimilated into the Integrated Forecasting System (IFS) since 1996, beginning with ERS-1 and ERS-2 Scatterometer data. Currently ASCAT wind products from Metop-B [7][24] and Metop-C, will be termed as ASCAT-B and ASCAT-C, respectively, satellites are assimilated together with HY-2B observations. The importance of scatterometer observations and their positive impact on NWP and wave models has long been recognized [10][27][28]. In particular, C-band scatterometers, like the ones onboard the ERS and the Metop satellite series, provide information in almost all-weather conditions. These observations are therefore important, often unique, for the analysis of extreme events (usually characterized by cloud and rainfall) such as tropical cyclones (TCs) and extra-tropical storms. It has also been confirmed that ASCAT observations have a substantial impact on the ocean variables in coupled ocean-atmosphere assimilation systems [10] 30].

The initial study 'Characterisation of ocean surface roughness in NWP' was performed by ECMWF under contract EUM/CO/18/4600002207/Sli (see [8]). This project was aimed at exploring how to increase the value of scatterometer observations in NWP, by assessing the assimilation of new geophysical variables closer to what the scatterometer actually measures over the ocean. The assimilation of surface stress and stress equivalent winds were tested. But the experiments performed with these new geophysical variables did not show any clear benefit on the quality of the analysis and forecast.

One difficulty with the stress assimilation may be related to the mapping of the ambiguous winds vectors provided by the geophysical model function (GMF) (currently the CMOD5.n [25] is used in operations) to stress space. This additional processing step is unlikely to change the real information content of the observation. An alternative approach is the direct assimilation of backscatter coefficient "sigma0" ($\boldsymbol{\sigma}^0$; also known as the normalized radar cross section, NRCS) triplets, thereby removing the GMF from the observation processing chain.

Extensive effort was dedicated to retrieve wind vector from $\boldsymbol{\sigma}^0$ (e.g., [25] [29] [34]) and use the retrieved wind vector in data assimilation (e.g. [27] [28] [33]). Very little work was carried out on the direct assimilation of $\boldsymbol{\sigma}^0$ for two main reasons: the wind direction ambiguity and the non-linearity of the wind - $\boldsymbol{\sigma}^0$ relationship (e.g. [29] [33] [35]). At ECMWF, for example, the GMF tangent-linear and adjoint codes required to assimilate $\boldsymbol{\sigma}^0$ were not available before the start of this project.

It is time to revisit these results. The 4D-Var assimilation approach naturally uses prior information to constrain ill-posed retrieval problems. Ill-posed problems are ambiguous by definition, because multiple atmospheric states can produce the same measured value. In addition, recent progress tackling non-linear problems in the "All Sky" assimilation of radiances [20] might suggest that some non-linearities considered problematic in the 1990's might now be overcome. However, this suggestion needs to be tested.

Preliminary results obtained at ECMWF with a $\boldsymbol{\sigma}^0$ forward operator based on a neural network have been presented with promising results during the final meeting of the initial study and during the ECMWF-EUMETSAT Science bilateral, on 26/04/2022. ECMWF has trained an artificial neural network (ANN) to forward model ASCAT-B scatterometer $\boldsymbol{\sigma}^0$ triplets. This work used ECMWF 10-m neutral equivalent wind vectors and measurement geometry parameters ("features" in ANN terminology) to simulate operational ASCAT-B $\boldsymbol{\sigma}^0$ triplet values ("targets"), using "trusted" measurements that have passed operational quality control and have been assimilated. The work was performed using the Keras/TensorFlow ([4] and [1]) software packages (in python). The early results are encouraging, and equally importantly the ANN approach seems to be very flexible, so that the impact of other variables on the fit to $\boldsymbol{\sigma}^0$ can also be tested. This could include atmospheric air density, sea-state information, rain-rate.

We note that an ANN approach was used more than 20 years ago to develop scatterometer forward models [5]. Furthermore, ANN is also being tested for scatterometer soil moisture applications [3].

1.2. Used Data

ASCAT backscatter data were retrieved from the ECMWF operational Observational Data Base (ODB) archived on ECMWF Meteorological Archival and Retrieval System (MARS) [15]. Only observations that were assimilated actively are used for training since training requires the best available data. Assimilated observations are usually of good quality. Scatterometer data including backscatter observations with their corresponding geometry (incidence and azimuthal angles) and model wind vectors from both background (first-guess, FG) and analysis (AN) and other related information are stored in ODB during data assimilation. Observations from ASCAT-B were mainly used for training purposes. Validation was carried out using observations from both ASCAT-B (but during different time windows) and ASCAT-C.

Several periods (mainly from 2020 and 2021) were used depending on the availability of the data. The final training, however, was based on ASCAT-B observations covering the whole year spanning from 1 August 2020 till 31 July 2021.

For other variables, IFS short forecasts (FC) from step 1 till step 12 (hours) from the ECMWF operational suite were used. Fields of those variable were retrieved from MARS and were collocated with the ASCAT data from ODB. Closest grid point and time were selected to reduce the impact of interpolation. Both atmospheric and ocean-wave data were used to examine their impact on the learning ANN process.

1.3. Artificial Neural Network (ANN) Model

An Artificial Neural Network (ANN) model of ASCAT backscatter ($\boldsymbol{\sigma}^0$) has been developed using Keras/TensorFlow ([4] and [1]) package. Model wind vector (in addition to other model variables that will be specified later) and the geometry of the scatterometer beam with respect to the wind vector are the input variables ("features"). ASCAT $\boldsymbol{\sigma}^0$ is the ANN model output "target".

ANN training is comparable to the traditional CMOD training (e.g. [25]) but with more flexibility and without the need of the precise knowledge regarding the underlying physics. Once enough existing features-target data are available, the ANN can extract the relation (~ physical laws) between the pair. In fact, ANN only figures out the "pattern" in the data. Therefore, the found "relation" cannot be written in a closed form. However, ANN model parameters are produced and stored for later usage for verification and implementation of the model.

The following ANN configuration is used:

- A Sequential ANN model is used since it is most appropriate for a plain stack of layers where each layer has exactly one input tensor and one output tensor (https://keras.io/guides/sequential_model/).
- The input layer is composed of, at least, four input nodes. There is one node for each wind vector component, one node for each of the scatterometer incidence and azimuthal angles. Other nodes are added for each additional physical variable to be used.
- Two identical hidden dense layers are implemented. The "dense layer" is a term used to describe a layer of nodes with each node receiving input from all the nodes of the previous layer.
- Each layer is composed of 64 nodes.
- The activation function transforms the input to the output (also called activation) at the node level. Linear activation functions are easy to implement and execute. However, to learn complex mappings, nonlinear activation functions are required. Two activation functions were tested:
    - The rectified linear (ReLU) activation function which is a piecewise linear function that will output the input directly if its argument is positive, otherwise, it will output zero. Its derivative is 1 for positive arguments and zero otherwise. These characteristics make ReLU the favoured activation function for many types of neural networks.
    - The hyperbolic tangent (tanh) activation function, which is an S-shaped function symmetric around 0 and saturates at the values of 1 and -1 for high positive and negative values, respectively. This saturation for high argument values is a challenge for the learning process. tanh activation function is much less efficient compared to the ReLU function. However, this function is the recommended one for data assimilation.
- The output layer is composed of a single node representing $\boldsymbol{\sigma}^0$.

- The loss function, which is the equivalent term for the cost function in data assimilation, is the sum of the errors to be minimised. ANN model training is achieved through an optimisation of the loss function. The loss is represented by the mean square error (MSE), which is the average of the squared differences between the predicted and actual values.
- The optimisation algorithm (optimiser) is selected as the stochastic gradient descent (SGD) which is a very efficient optimiser.

Summary of ANN model configuration is listed in Table 1.

Table 1: Summary of ANN model configuration.

Model Elements	**Description**
Model type	Sequential
Number of layers	1 input, 1 output and 2 hidden (3 hidden layers configuration was tested)
Type of hidden layers	Dense
Number of nodes	64 for each hidden layer (other number of nodes were tested)
Activation function	The following were used separately: - rectified linear (ReLU) - hyperbolic tangent (tanh)
Input layer	At least 4 nodes: - 2 nodes for model wind vector; - 2 nodes for scatterometer geometry; and - 1 or more nodes for each additional variable (if used)
Output layer	1 node for $\boldsymbol{\sigma}^0$
Loss function	Optimisation of mean square error (MSE)
Optimiser	Stochastic gradient descent (SGD)

Several deviations from the above configurations were considered. Networks that include 2 hidden layers with 16, 32, 64 and 128 nodes as well as 3 layers with 64 and 32 nodes were tested. The impact was marginal and, therefore, for the sake of efficiency and accuracy we decided to use the above configuration in terms of layers and nodes.

1.4. ANN Model Training and Validation

1.4.1. ANN Observation Operator Based on Wind Vector

ASCAT-B observations collocated with the IFS model wind vectors were used for the ANN training. The final training was based on data covering the whole year spanning from 1 August 2020 till 31 July 2021. First, only IFS model first guess (FG) wind vector was used for training and validation. The trained ANN model (ANN_{FG}) was used to estimate $\boldsymbol{\sigma}^0$ values corresponding to IFS model FG wind vector data covering the 9-month period from 1 August 2021 to 30 April 2022. Later this period was extended till the end of March 2023, i.e. a total of 20 months and the change in the statistics was marginal.

The scatter plot showing the correlation between validation results of $\boldsymbol{\sigma}^0$ values estimated using ANN_{FG} and FG winds and those measured by ASCAT-B for the 9-month validation period are shown in Figure 1. With most of the data pairs being narrowly scattered around the symmetric 45-degree line, the agreement is rather excellent. However, a small number of collocations show higher scatter. Another important observation in Figure 1 is the inability of ANN_{FG} model to produce $\boldsymbol{\sigma}^0$ values below -31.29 dB. Such low values, whose locations are shown in Figure 2, are associated with very light wind. This is in fact in agreement with available experimental evidence (e.g. [14]) that winds with speeds below a certain threshold (below around 2.0 m/s) is unable to produce any perturbation to the water surface. Therefore, any perturbations, which allow the radar signal to be scattered back to the scatterometer antennas, under very light winds are due to other variables like ocean swell. This is also clear in the variation of $\boldsymbol{\sigma}^0$ with respect to the wind speed shown in Figure 3.

Time series of the monthly standard deviation of the difference (SDD), mean absolute error (MAE), bias and correlation coefficient (C.C.) between ANN_{FG} estimated $\boldsymbol{\sigma}^0$ (based on FG wind input) and measured $\boldsymbol{\sigma}^0$ by ASCAT-B and ASCAT-C are shown in Figure 4. The monthly SDD, MAE and C.C. values are virtually constant for the whole training (in case of ASCAT-B) and validation periods (August 2020 till March 2023). The results from ASCAT-B and ASCAT-C are also the same with very minor advantage for ASCAT-C (smaller SDD values and higher C.C. values during few months). The differences are negligible. The validation against the ASCAT-B data set that was used for training does not give any advantage for that data set. The minor advantage of ASCAT-C results is still valid.

However, $\boldsymbol{\sigma}^0$ estimates by ANN_{FG} using FG wind show a small bias as can be seen from Figure 4. Bias with respect to ASCAT-B $\boldsymbol{\sigma}^0$ is zero during the training period, as expected. However, the bias shows an increasing trend afterwards. $\boldsymbol{\sigma}^0$ bias with respect to ASCAT-C shows a rather constant shift of about 0.07 dB compared to bias against ASCAT-B. Otherwise, the bias with respect to ASCAT-C follows the same pattern as that of ASCAT-B. This implies that ASCAT-C $\boldsymbol{\sigma}^0$ is higher than that of ASCAT-B. The increasing trend could be coming from the scatterometers or from the IFS model forecast. However, we are expecting that IFS model is the source of the increasing trend since a similar trend in both instruments is highly unlikely.

The $\boldsymbol{\sigma}^0$ bias (between ANN_{FG} estimates and the scatterometers) in Figure 4 shows a seasonal variation with peaks in January and August and troughs in April and October.

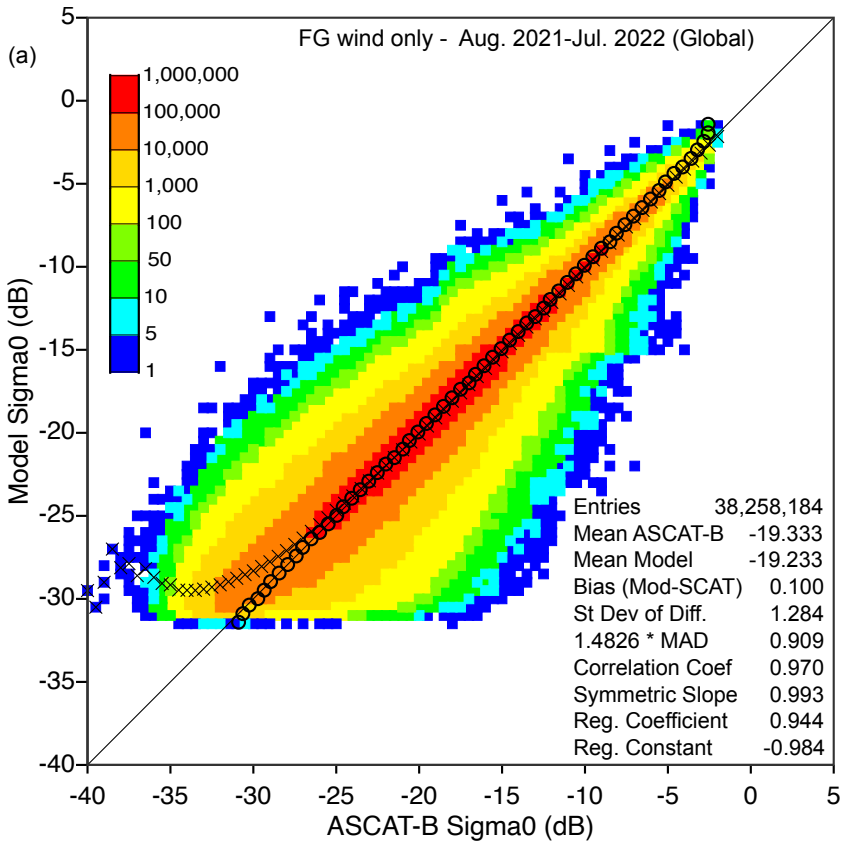

Figure 1: Validation of a year (1 August 2021 – 31 July 2022) of the ANN_{FG} model σ^0 estimates using IFS model FG wind vectors against measured σ^0 by ASCAT-B.

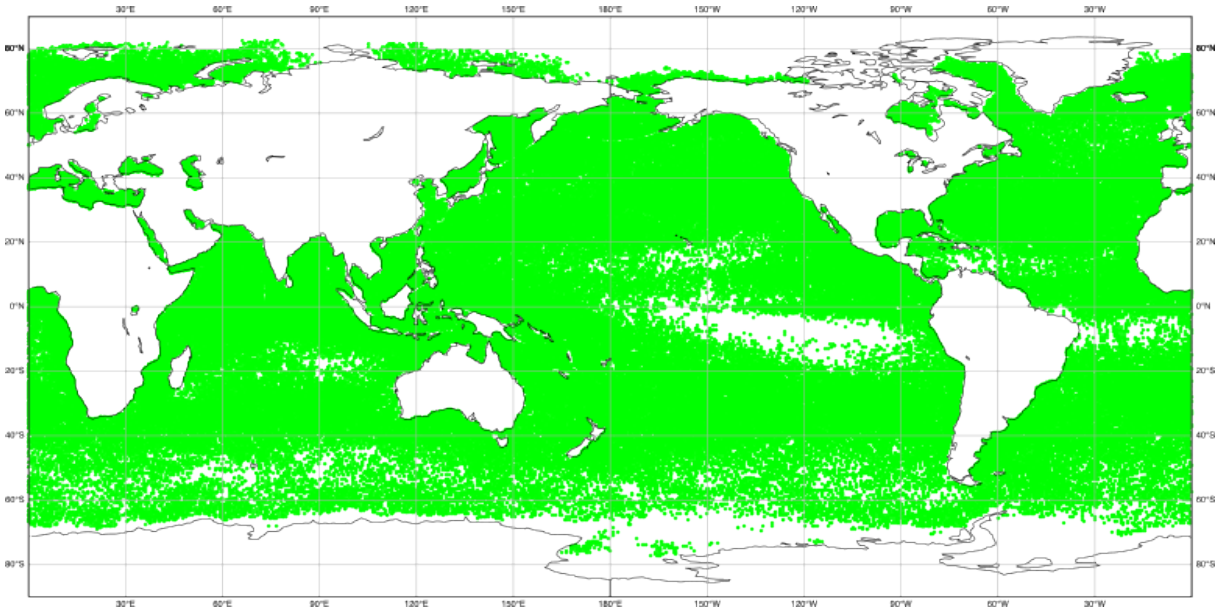

Figure 2: Geographical distribution of low (below -31.29 dB) values of measured σ^0 during the full year from 1 August 2021 – 31 July 2022.

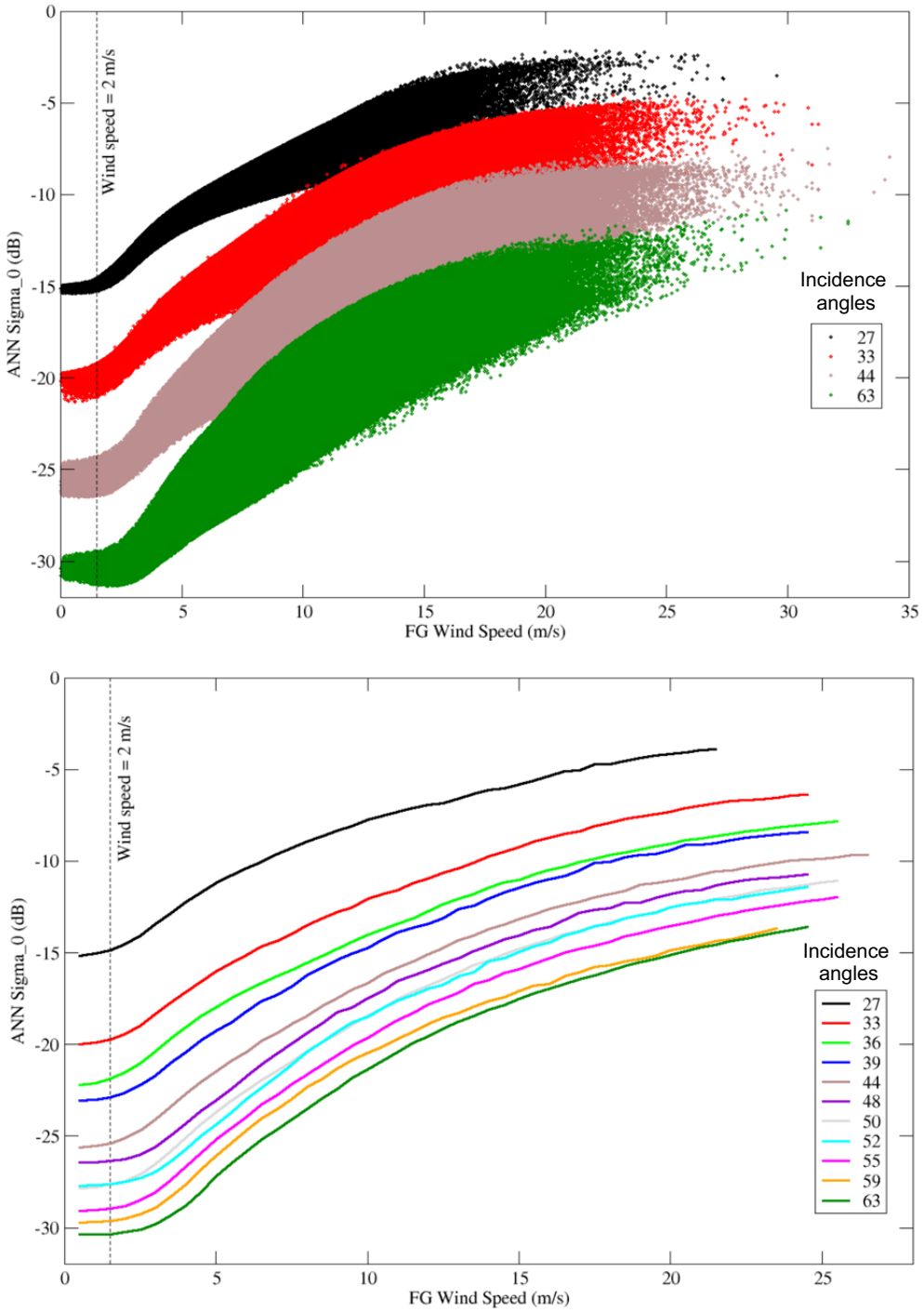

Figure 3: Relation between ANN sigma_0 and wind speed for different incidence angles (training using FG wind only). The left-hand panel shows the data clouds for 4 incidence angles. The right-hand panel shows the centreline of the data clouds of 11 incidence angles.

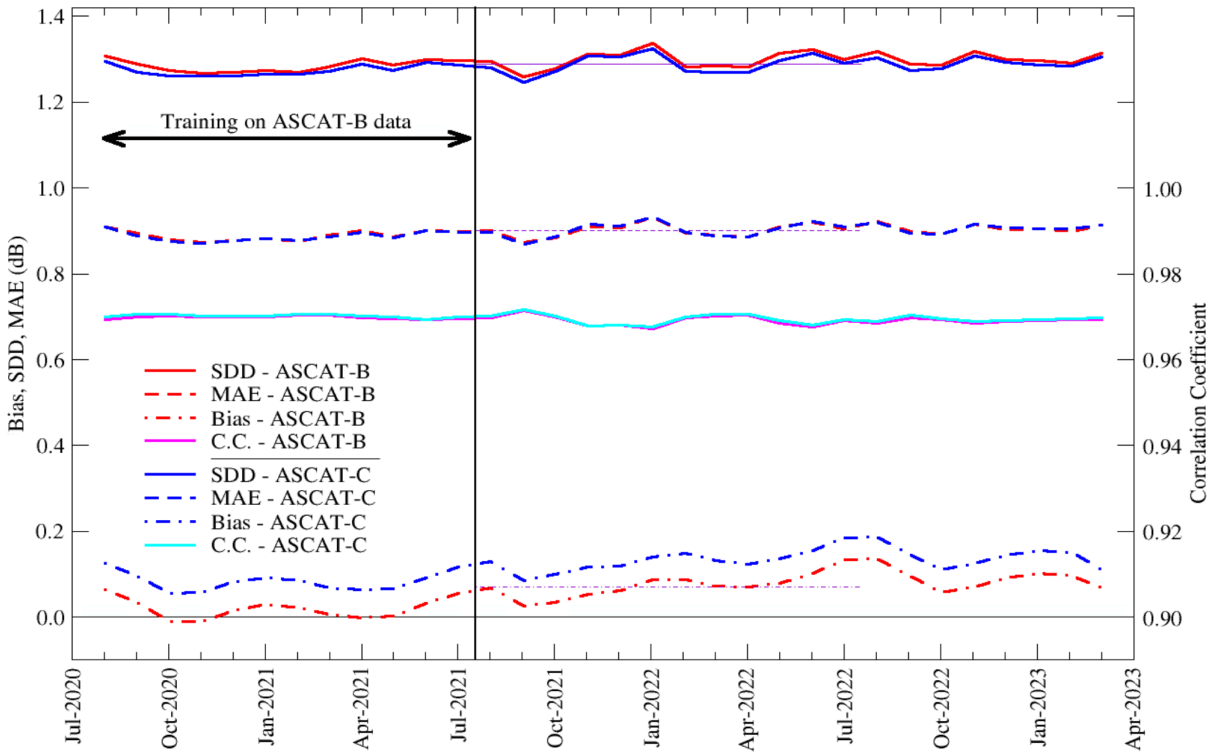

Figure 4: Time series of monthly standard deviation of the difference (SDD), mean absolute error (MAE), bias and correlation coefficient (C.C.) between ANN estimated $\boldsymbol{\sigma}^0$ (based on FG wind) and measured $\boldsymbol{\sigma}^0$ by ASCAT-B and ASCAT-C. Training was carried out using ASCAT-B data during the period shown by the two-sided arrow.

The geographical distribution of bias of ANN_{FG} model $\boldsymbol{\sigma}^0$ estimates using IFS model FG wind vectors with respect to the measured $\boldsymbol{\sigma}^0$ by ASCAT-B during the 1-year period from 1 August 2021 to 31 July 2022 is shown in Figure 5. The small bias (below 0.1 dB) dominates the map. However, there are higher bias values in the Tropics. It is possible to relate high biases with major ocean currents like: the Pacific South Equatorial Current, the Pacific Equatorial Counter-current, the Guinea Current, Kuroshio Current, Agulhas Current and, to less extent, the Gulf Stream.

The geographical distribution of SDD and scatter index (SI; which is the SDD normalised by the mean value) of ANN_{FG} model $\boldsymbol{\sigma}^0$ estimates using IFS model FG wind vectors with respect to the measured $\boldsymbol{\sigma}^0$ by ASCAT-B during the 1-year period from 1 August 2021 to 31 July 2022 are shown in Figure 6 and Figure 7, respectively. The SDD is predominantly below 1.5 dB. That corresponds to SI value of 8%. There are, however, some areas with high SDD and SI values like around the Indonesian Islands and the Pacific coast of Central America.

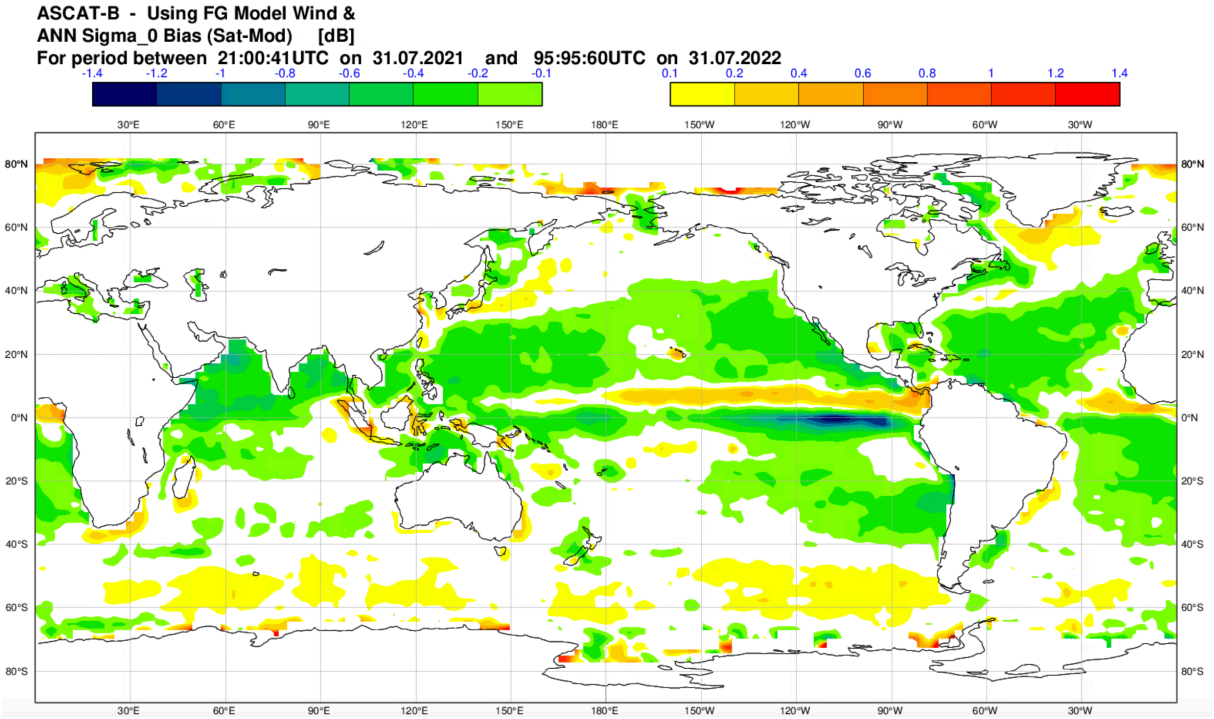

Figure 5: The geographical distribution of bias, in dB, between ANN_{FG} model σ^0 estimates using IFS model FG wind vectors and the measured σ^0 by ASCAT-B during the 1-year period from 1 August 2021 to 31 July 2022.

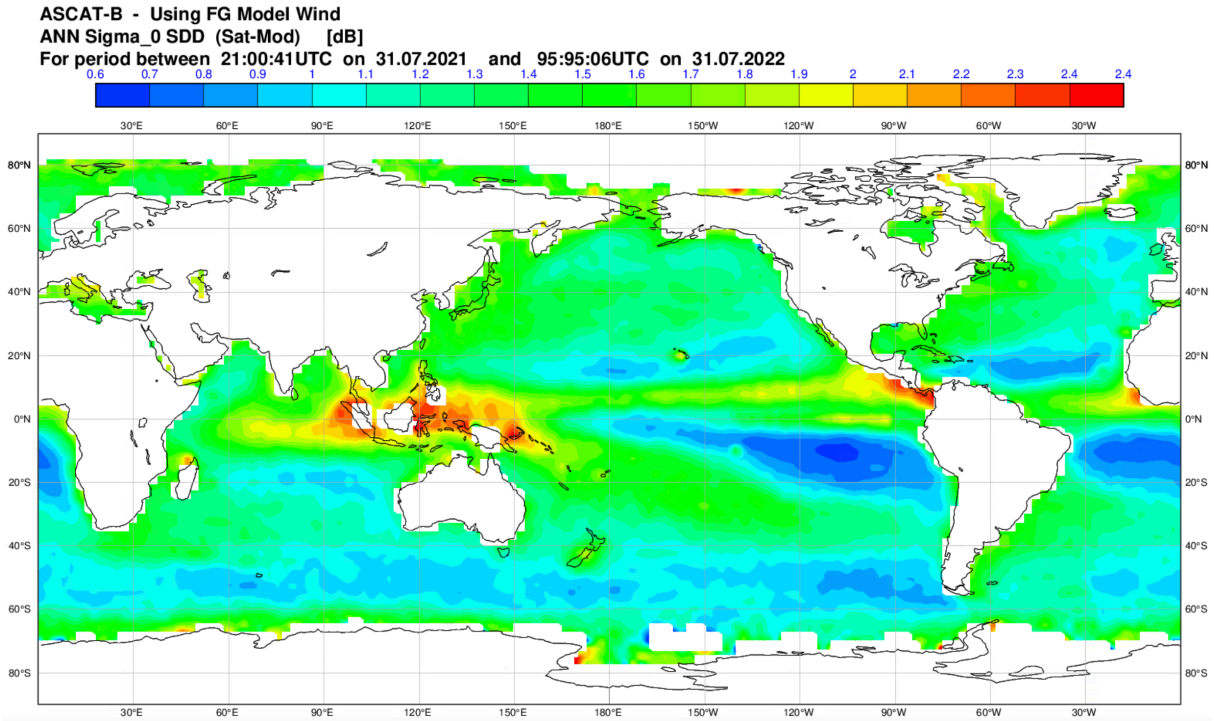

Figure 6: Same as for Figure 5 but for the standard deviation of the difference (SDD), in dB.

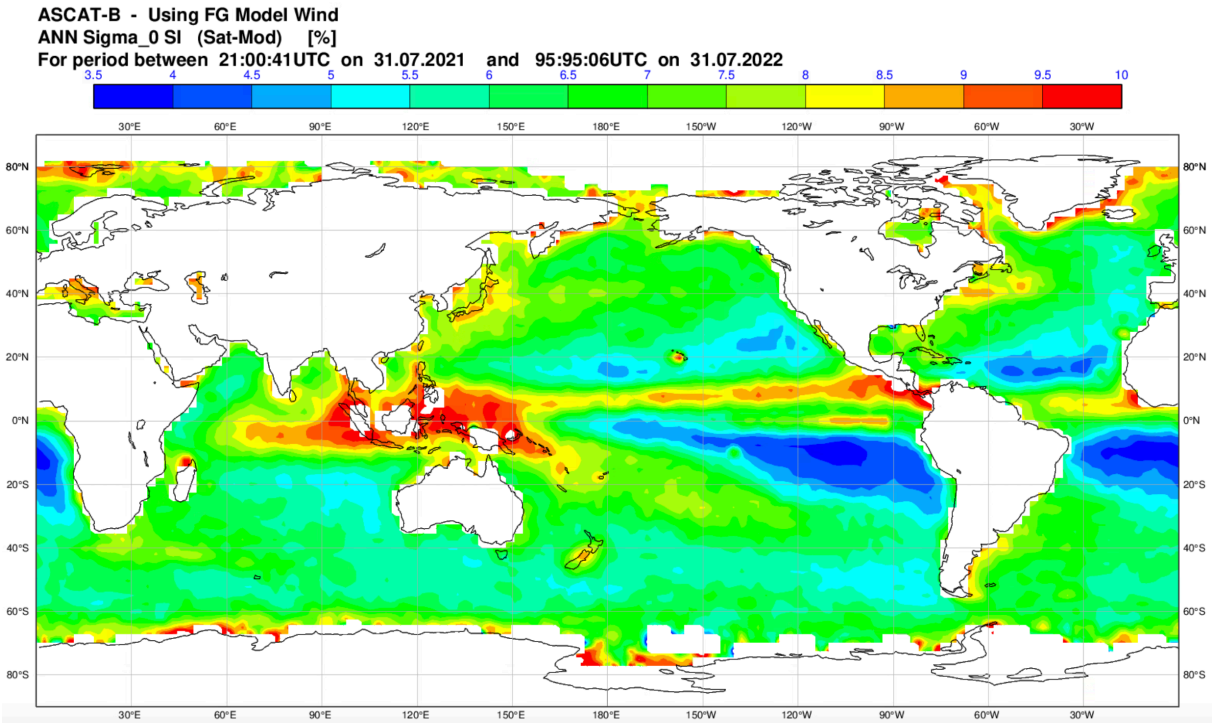

Figure 7: Same as for Figure 5 but for the scatter index (SI), in percentage, which is the SDD normalised by the mean value.

1.4.2. Use of Analysis versus First-Guess Wind Vector

Model analysis (AN) winds are in theory the best winds available from a numerical weather prediction (NWP) system like the ECMWF IFS. These AN model winds are the result of data assimilation (i.e. merging observations with the model) process. Currently, IFS assimilates ASCAT-B and ASCAT-C scatterometer winds after inversion. Therefore, the use of AN winds is usually not preferred to be used for training. This is the main reason behind starting with the use of the model first-guess (FG) winds, which are the results of model short forecasts that are needed to represent the model state (background) in the data assimilation system. Model FG data are not impacted by the observations within the same time window They are, however, impacted by data from previous time windows. This is not a real issue unless there is a "systematic error".

The ANN training presented so far was based on model FG winds (ANN_{FG}) and is represented schematically in Figure 8. Alternative training can be carried out using AN winds (ANN_{AN}) as shown in Figure 9. For the validation, it is possible to estimate $\boldsymbol{\sigma}^0$ values using either ANN model (ANN_{FG} or ANN_{AN}) and either wind type: FG wind as shown in Figure 10 or AN wind as shown in Figure 11. The statistics from all four combinations are listed in Table 2 for FG winds and in Table 3 for AN winds.

It is clear from Table 2 and Table 3 that both models perform equally well for any given wind type. In fact, the wind type used in the $\boldsymbol{\sigma}^0$ estimation dictates the performance. AN winds produce better $\boldsymbol{\sigma}^0$ values than FG winds irrespective of wind used in the model training. However, ANN_{AN} model produces slightly better $\boldsymbol{\sigma}^0$ values when used with AN wind.

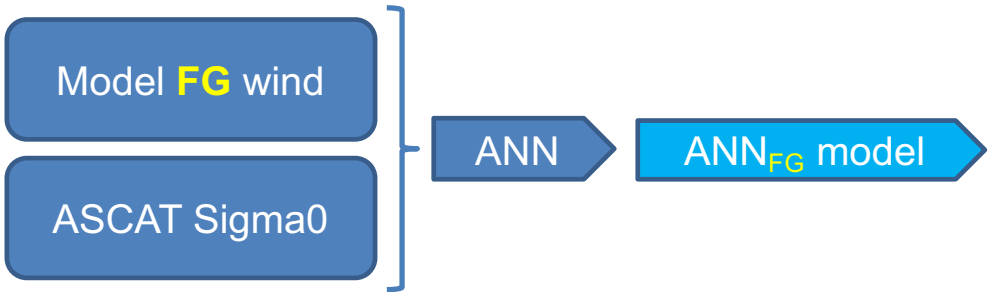

Figure 8: Schematic diagram showing the ANN_{FG} training.

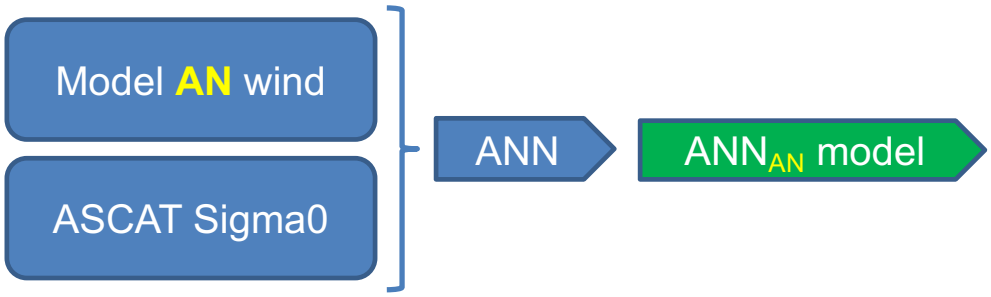

Figure 9: Schematic diagram showing the ANN_{AN} training.

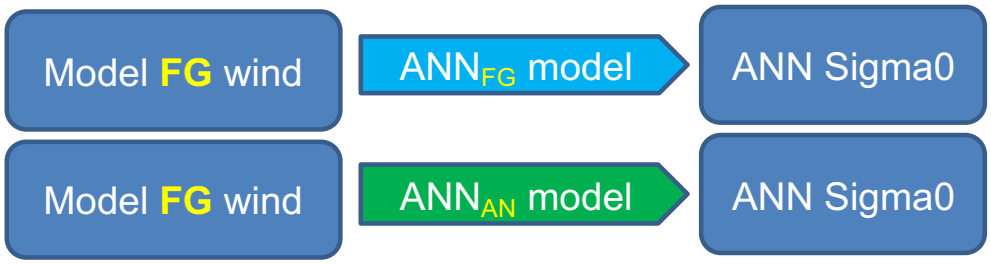

Figure 10: Schematic diagram showing the use of model FG wind to validate both ANN trained models; namely: ANN_{FG} and ANN_{AN}.

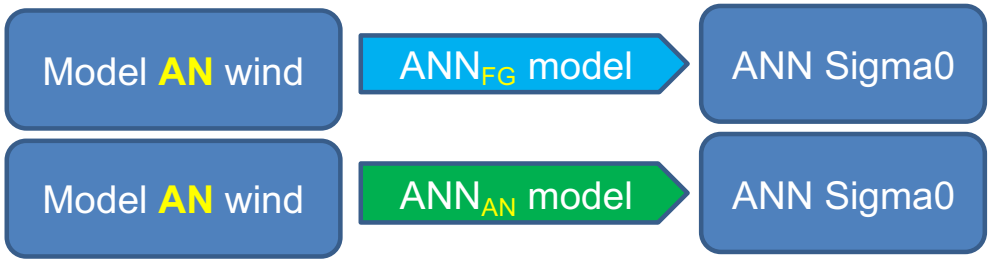

Figure 11: Same as Figure 10 but the use of model AN wind instead of model FG wind for validation.

Table 2: Verification of ANN models trained using FG (ANN_{FG}) and AN (ANN_{AN}) winds when used with FG winds.

N = 1266843	ANN model trained using FG wind (ANN_{FG})	ANN model trained using AN wind (ANN_{AN})
Bias	0.023	0.048
SDD	1.314	1.316
R	0.9682	0.9681

Table 3: Same as Table 2 but when used with AN winds.

N = 1266843	ANN model trained using FG wind (ANN_{FG})	ANN model trained using AN wind (ANN_{AN})
Bias	-0.012	0.005
SDD	1.012	0.980
R	0.9813	0.9824

1.4.3. Impact of Seasonality of Training Period

The sensitivity of the performance of the ANN model on the training duration and the period used for validation was tested. To do so, we divided ASCAT-B $\boldsymbol{\sigma}^0$ data collocated with the IFS model FG wind covering a period of 8 months into two equal parts: the first 4-month period between 1 August and 30 November 2020 was reserved for training while the following 4-month period from 1 December 2020 to 31 March 2021 was reserved for validation. (This was done at an early stage when there was not much data available).

Various durations and timings were selected to train ANN_{FG} $\boldsymbol{\sigma}^0$ models. In total 10 models were trained. The model durations and timings are schematically shown in the timeline in the left-hand panel of Figure 12 and Figure 13 (same timeline in both figures). All models were validated against the whole validation data set from the second 4-month period as shown in the same timeline. The SDD and correlation coefficient for each model are shown in the right-hand panels of Figure 12 and Figure 13, respectively.

It is clear that the best results are achieved with training using 4 months of data followed closely by training using the 3 months just before the start of the validation period (the top two horizontal bars in Figure 12 and Figure 13). The third best is the ANN model trained using the 3 months with a month gap from the validation start (third horizontal bar in the figures) followed closely with the model trained

using the closest two months to the validation period (fourth bar in the figures). The performance of the models based on the other two-month periods degrades as the gap to the validation period increases. The two models based on monthly data closer to the validation period perform better than the model based on the furthest 2-month period. The models based on monthly data show better performance when they are closer to the validation period. The only exception is the model based on data from October 2020.

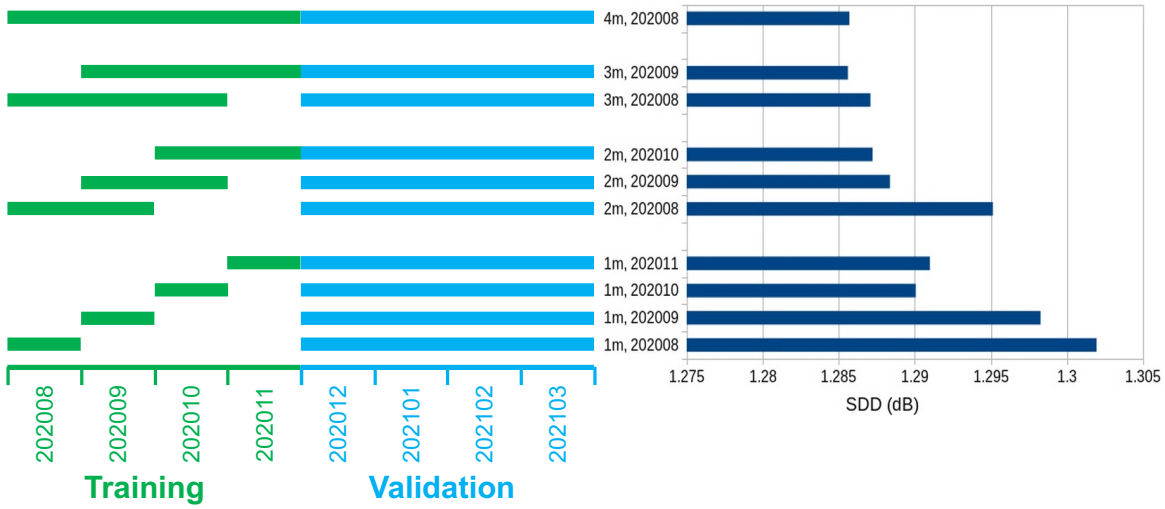

Figure 12: Impact of training duration and its timing with respect to validation period on SDD. Validation of ANN_{FG} model trained using datasets (FG wind and ASCAT-B σ^0) for various durations within 4-month period from 1 August to 30 November 2020 against ASCAT-B data covering the following 4-month period from 1 December 2020 to 31 March 2021. The labels next to the horizontal bars, represent the duration of training in months and the month at which the training duration commenced. Left-hand panel shows the corresponding timeline of the training and validation periods.

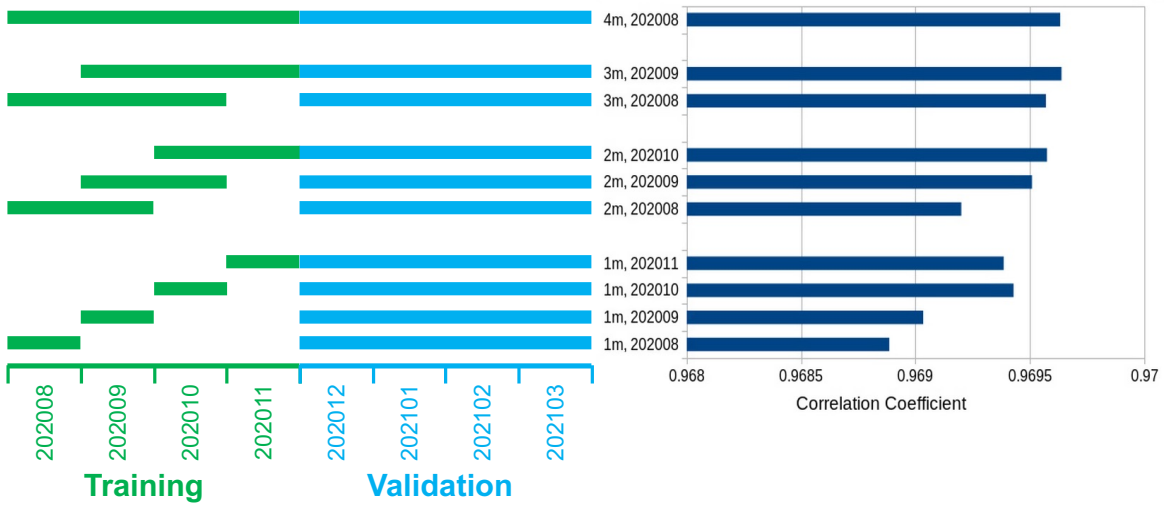

Figure 13: Same as Figure 12 but for impact on the correlation coefficient. The timeline on the left-hand panel is the same as that in Figure 12.

Although the duration of the training data seems like an important factor to produce better performance, it is in fact how much the data are closer to the validation period which is more important. It is important to recall from Figure 4 that a model based on a full year of data behaves equally good at all periods of time including those which are more than a year away. One can conclude that a year of data hopefully covering a wide range of weather conditions is needed for training a successful ANN model.

1.4.4. Impact of Including Air Density

Air density is one of the variables which influence the impact of wind speed on the water surface. This impact was studied and included in CMOD-7 [34]. The air density as computed from IFS was included as a feature (input) to the ANN model. Validation of $\boldsymbol{\sigma}^0$ values estimated by the ANN model against ASCAT-B $\boldsymbol{\sigma}^0$ data shows marginal impact on SDD and correlation coefficient. However, upon comparing the geographical distribution of the difference between ANN estimated $\boldsymbol{\sigma}^0$ and the ASCAT-B measurements (see Figure 14) to those produced using FG wind alone (Figure 5), it is possible to notice that the differences are getting smaller with the inclusion of air density.

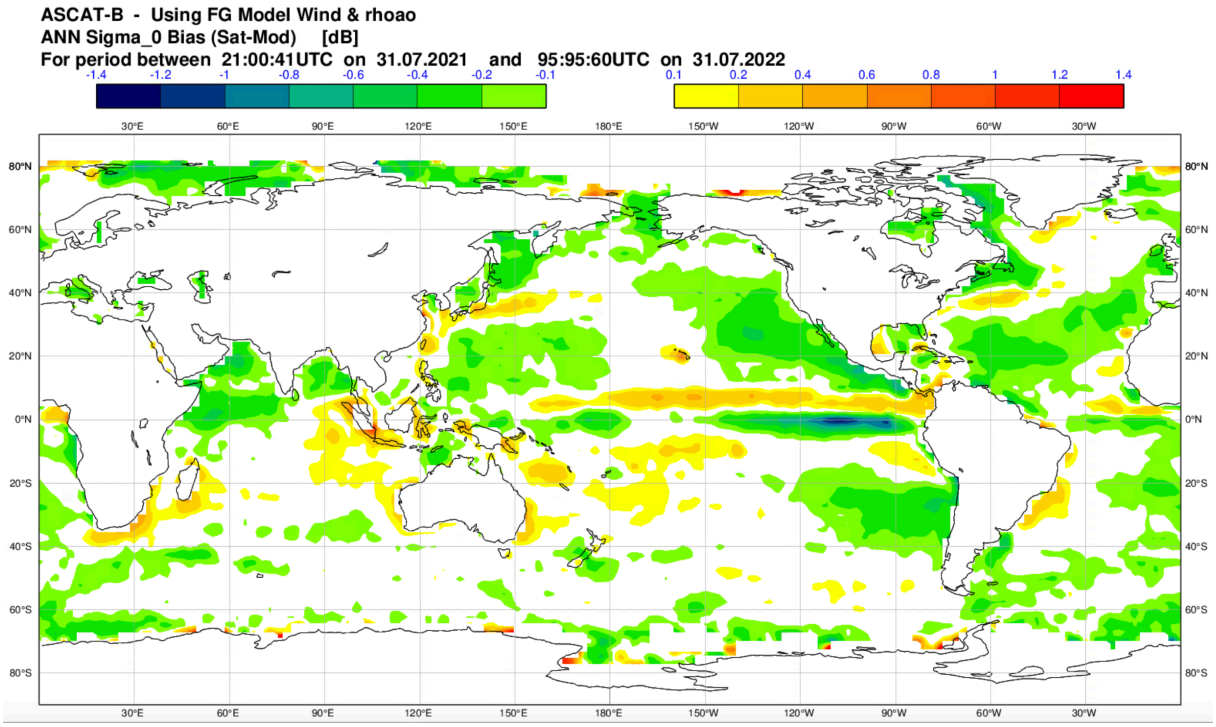

Figure 14: The geographical distribution of bias, in dB, between $\boldsymbol{\sigma}^0$ estimated by an ANN model that was trained using FG wind and air density and the measured $\boldsymbol{\sigma}^0$ by ASCAT-B during the 1-year period from 1 August 2021 to 31 July 2022.

1.4.5. Impact of Sea-State Variables

Since scatterometers detect the surface capillary gravity waves, other processes that contribute to (or hinder) the growth of such waves are needed to be considered while developing a scatterometer $\boldsymbol{\sigma}^0$ observation operator. The first candidate is the ocean waves. Although ocean waves have scales higher than the scale of the gravity-capillary waves, they do interact with each other. ECMWF runs an ocean wave model called ECWAM with IFS. The model predicts a wide range of sea-state variables. A list of some of those variables are listed in Table 4. The full list with description is available from [17]. The model short (up to 12 hours) forecast (FC) sea-state variables are used with the FG wind as well as model AN sea-state variables are used with AN wind.

Several combinations of sea-state variables were used for training and validation of the trained models. The training period runs from 1 August to 30 November 2020 while the validation period runs from 1 December 2020 to 31 March 2021. IFS FG model winds and ASCAT-B $\boldsymbol{\sigma}0$ measurements are used for both training and validation. The SDD, the percentage reduction in SDD and the correlation coefficient values for each model are shown in Figure 15, Figure 16 and Figure 17, respectively. The three plots suggest that the inclusion of significant wave height (SWH), mean zero-crossing wave period (also known as mean period based on second moment, MP2), normalized energy flux into waves (PHIAW), and normalized energy flux into ocean (PHIOC) to FG wind produces the best performance with a reduction of slightly less than 8% in SDD. The best performance for adding just two sea-state variables is for the inclusion of SWH and MP2 with about 5% reduction in SDD. For a single variable, the best sea-state variable to include is PHIOC with a reduction of about 2% in SDD.

The scatter plot comparing $\boldsymbol{\sigma}0$ from the ANN model that was trained using FG wind and the FC sea-state variables of significant wave height (SWH), mean zero-crossing wave period (MP2), normalized energy flux into waves (PHIAW), and normalized energy flux into ocean (PHIOC) to ASCAT-B $\boldsymbol{\sigma}0$ measurements is shown in Figure 18. The ANN model is now able to produce $\boldsymbol{\sigma}0$ values below 31.29 dB. This is quite an improvement compared to ANN models with wind-only training (see Figure 1).

The geographical distribution of bias between $\boldsymbol{\sigma}^0$ estimated by few ANN models that were trained using 1-year of data (1 August 2020 – 31 July 2021) and the measured $\boldsymbol{\sigma}^0$ by ASCAT-B during the 1-year period from 1 August 2021 to 31 July 2022 are shown in Figure 19, Figure 20 and Figure 21. The improvement that each sea-state variable combination on the bias clear.

Table 4: The used sea-state variables (sorted based on the short name).

Variable name	Short name	Units
Benjamin-Feir index	bfi	dimensionless
Coefficient of drag with waves	cdww	dimensionless
Mean wave period based on first moment	mp1	s
Mean zero-crossing wave period	mp2	s
Mean wave period	mwp	s
Mean wave direction of first swell partition	mwd1	degree
Mean wave direction of second swell partition	mwd2	degree
Mean wave direction of third swell partition	mwd3	degree
Mean wave period of first swell partition	mwp1	s
Mean wave period of second swell partition	mwp2	s
Mean wave period of third swell partition	mwp3	s
Mean square slope of waves	msqs	dimensionless
Normalized energy flux into waves	phiaw	dimensionless
Normalized energy flux into ocean	phioc	dimensionless
Peak wave period	pp1d	s
Air density over the oceans	rhoao	kg m^{-3}
Significant height of combined wind waves & swell	swh	m
Significant wave height of first swell partition	swh1	m
Significant wave height of second swell partition	swh2	m
Significant wave height of third swell partition	swh3	m
Normalized stress into ocean	tauoc	dimensionless
U-component stokes drift	ust	m s^{-1}
V-component stokes drift	vst	m s^{-1}
Wave spectral directional width	wdw	dimensionless
Wave energy flux magnitude	wefxm	W m^{-1}
Wave spectral kurtosis	wsk	dimensionless
Wave spectral peakedness	wsp	dimensionless
Wave spectral skewness	wss	dimensionless
Free convective velocity over the oceans	wstar	m s^{-1}

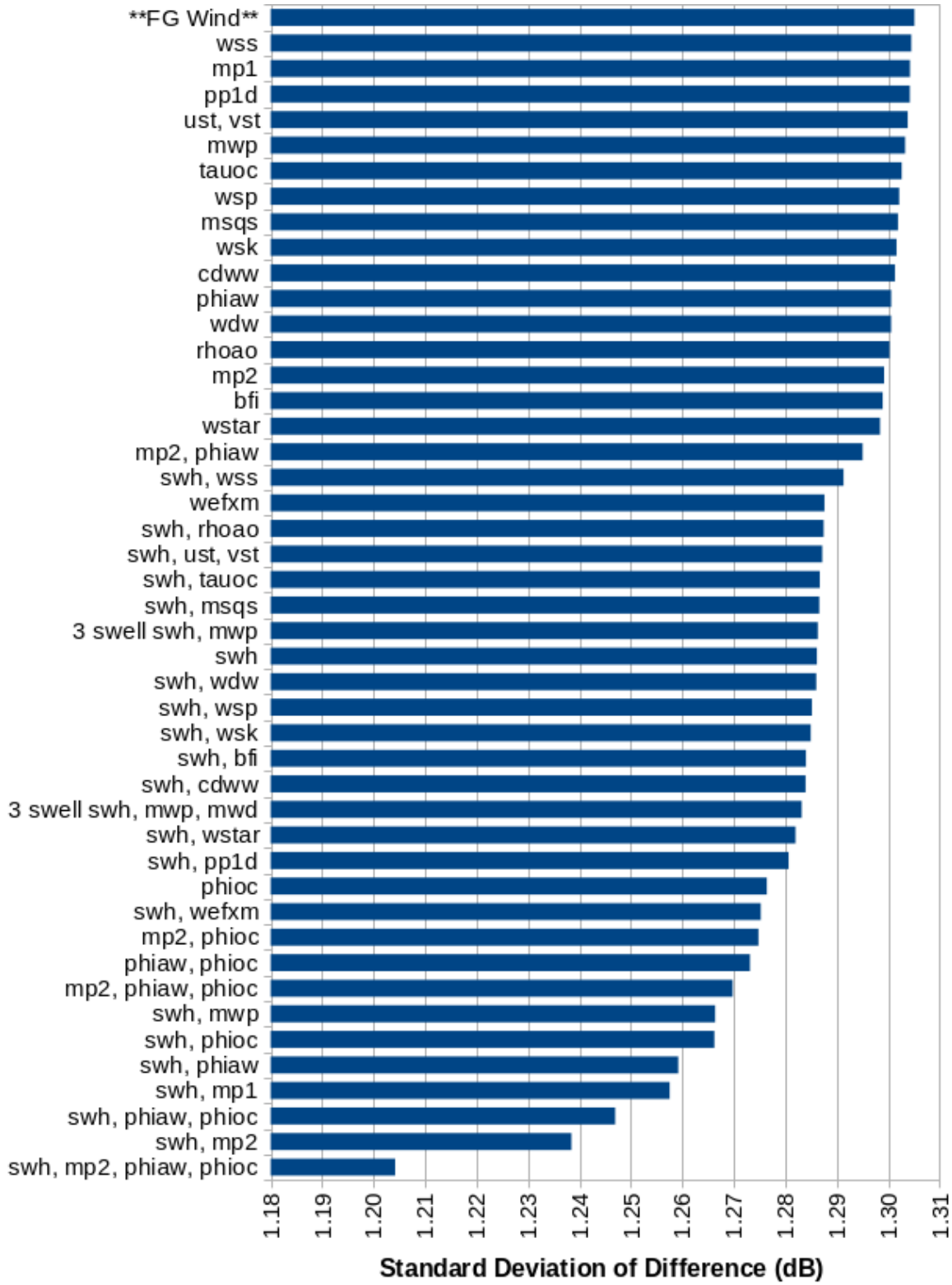

*Figure 15: Impact of adding sea-state variables to FG winds for training and validating the trained models against ASCAT-B σ^0 measurements in terms of SDD. Training period is from 1 August to 30 November 2020 while the validation period is from 1 December 2020 to 31 March 2021. The labels next to the horizontal bars represent the FC sea-state variables used for that model. The label "**FG wind**" refers to the reference FG-wind only model. Full names of variables are listed in Table 4.*

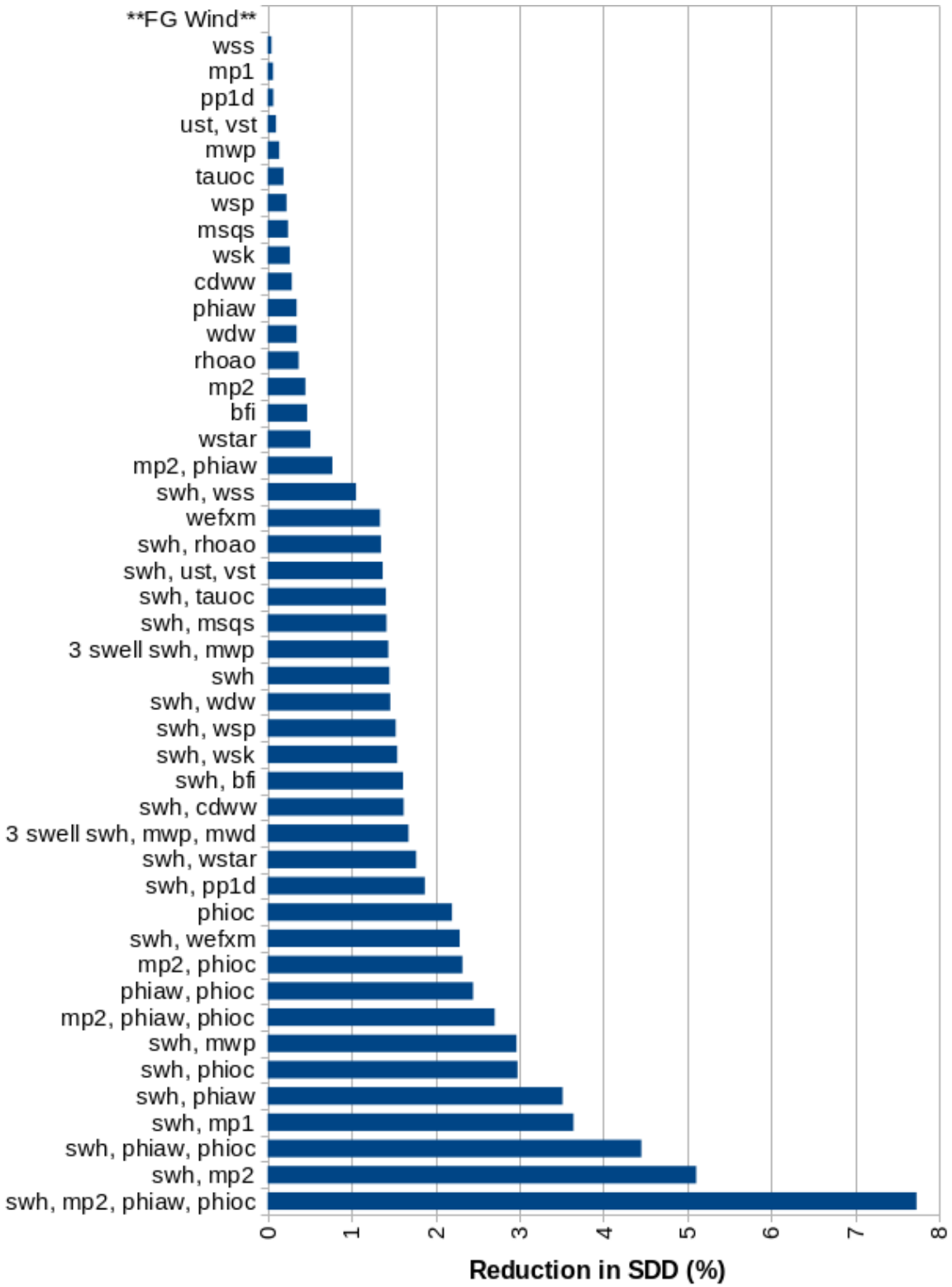

Figure 16: As Figure 15 but the impact is in terms of percentage reduction in SDD.

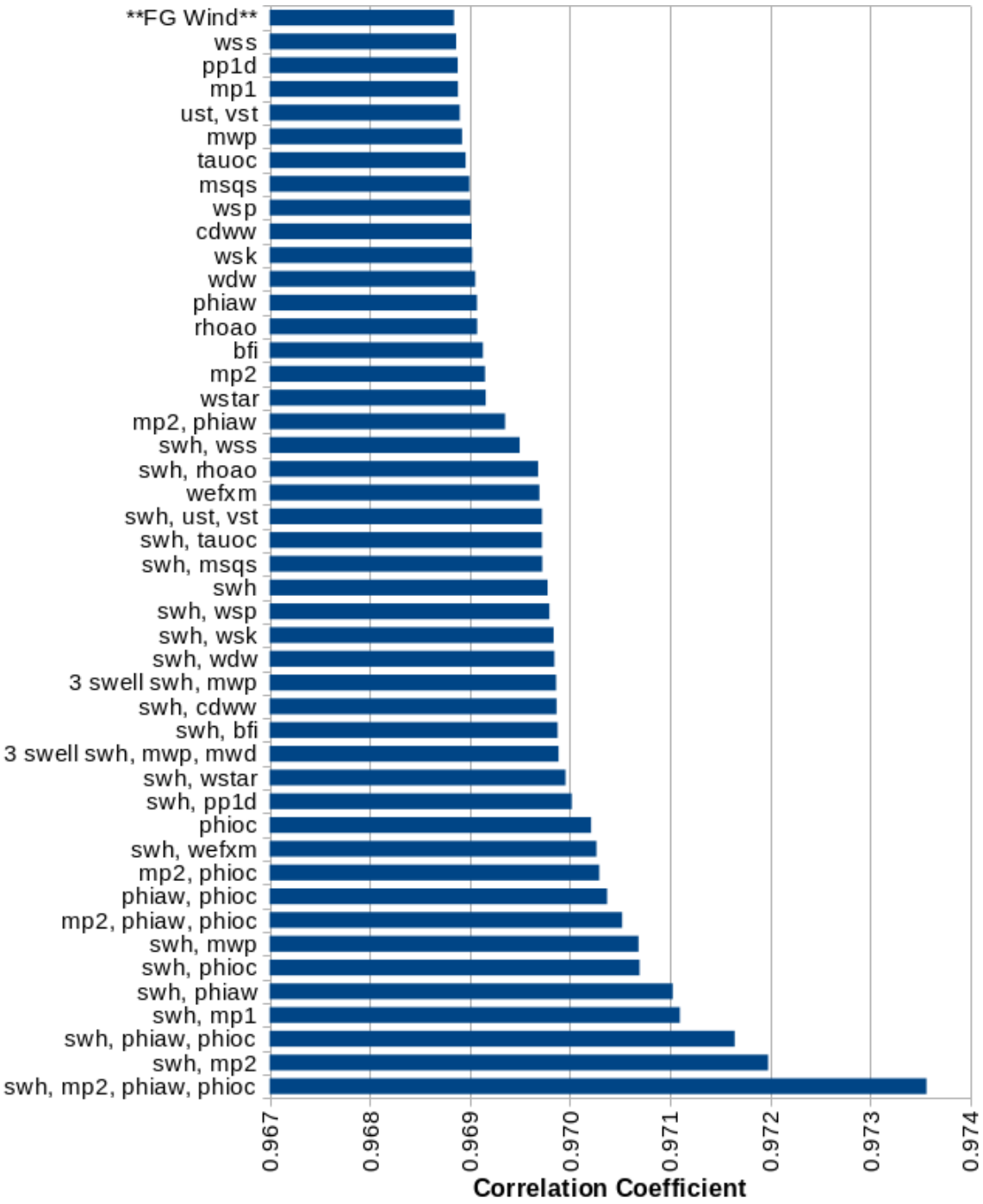

Figure 17: As Figure 15 but the impact is in terms of the correlation coefficient.

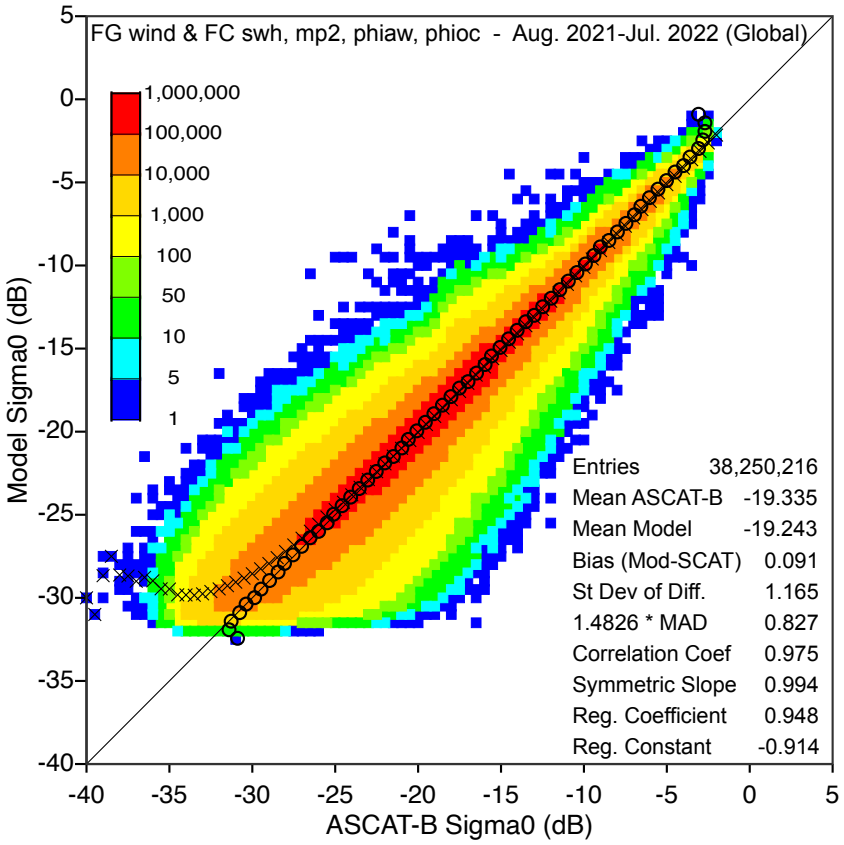

Figure 18: Comparison of $\boldsymbol{\sigma}^0$ estimated using an ANN model that trained using FG wind and the FC sea-state variables of significant wave height, mean zero-crossing wave period, normalized energy flux into waves, and normalized energy flux into ocean against ASCAT-B $\boldsymbol{\sigma}^0$ measurements over a year running from 1 August 2021 till 31 July 2022. The ANN model was trained on 1 year of FG wind vector and 4 FC sea-state variables covering the period from 1 August 2020 to 31 July 2021.

1.4.6. Impact of Atmospheric and Oceanic Variables

The development of surface capillary gravity waves, which impact the scatterometer backscatter signal, depends on several atmospheric and oceanic processes apart from wind strength. A (nonexclusive) list of some of these processes is provided in Table 5. The ECMWF IFS model provides global estimates of them. The oceanic variables considered here are sea surface temperature (sst), sea water practical salinity (so) and current velocity (eastward and northward sea water velocity, ocu and ocv, respectively). The remaining variables in Table 5, such as surface stress, surface roughness, precipitation, are all atmospheric variables. The full list with brief description is available from [17]. The model short forecast (FC up to 12 and 24 hours atmospheric and oceanic variables, in respective order) are used in addition to the FG wind. Note that the ANN modelling also requires the ASCAT incidence and azimuth angles for all cases even if they are not mentioned. As before, ASCAT-B $\boldsymbol{\sigma}^0$ values collocated with the IFS model variables covering the period from 1 August 2020 to 31 July 2021 (1 year) are used for training the ANN models. The data covering the following year (from 1 August 2021 to 31 July 2022) are used for the validation of the models.

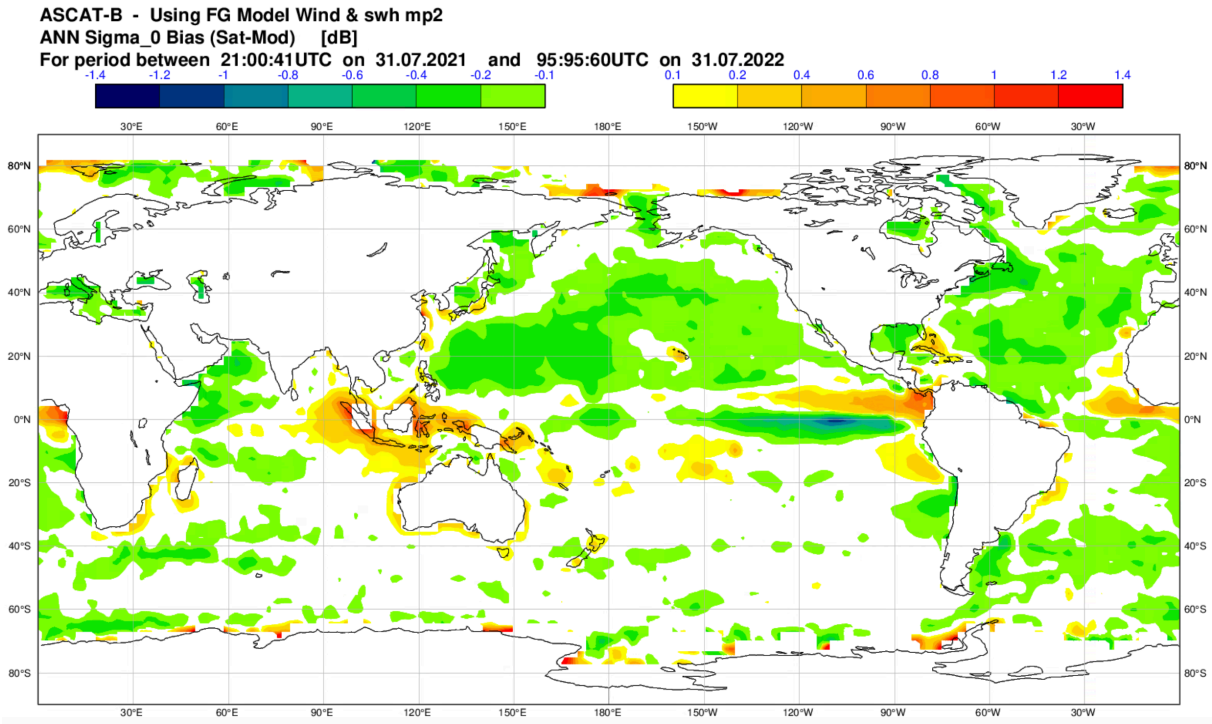

Figure 19: The geographical distribution of bias, in dB, between σ^0 estimated by an ANN model that was trained using FG wind and FC sea-state variables of significant wave height and mean zero-crossing wave period and the measured σ^0 by ASCAT-B during the 1-year period from 1 August 2021 to 31 July 2022.

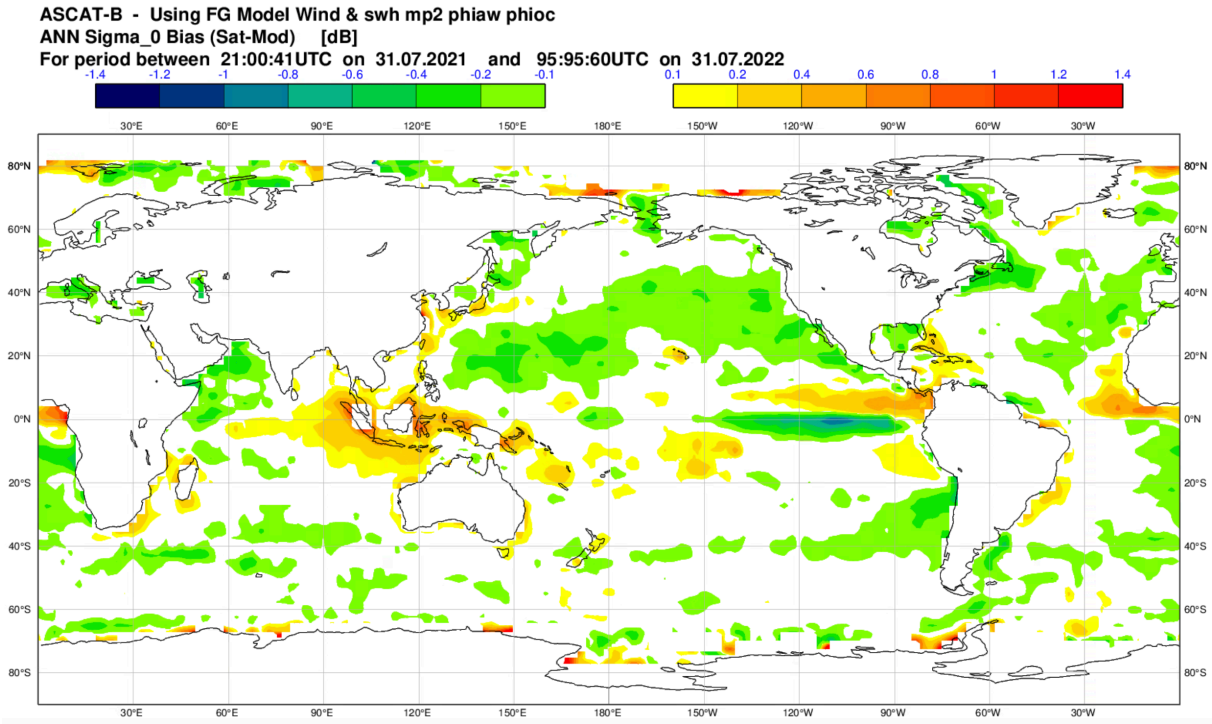

Figure 20: Same as Figure 19 but for the ANN model that was trained using FC energy flux into waves and energy flux into ocean on top of those used in the model of Figure 19 (i.e. FG wind and significant wave height and mean zero-crossing wave period).

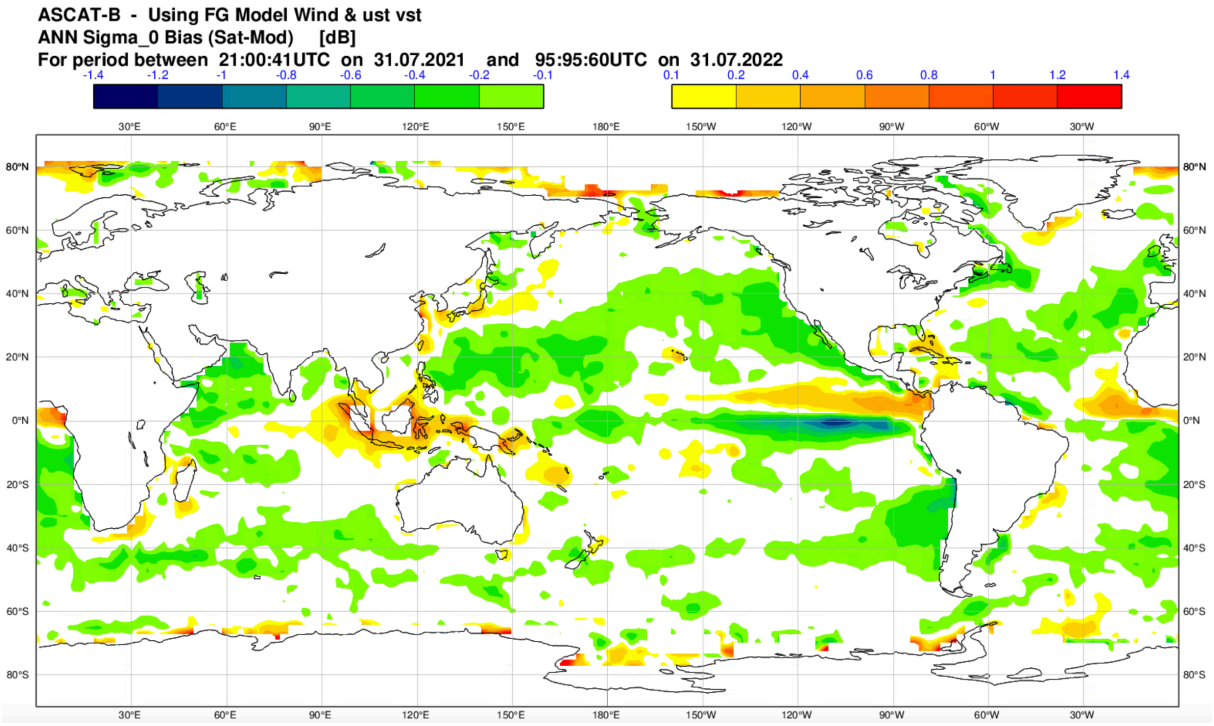

Figure 21: Same as Figure 19 but for the ANN model that was trained using FG wind and FC Stokes' drift vector.

The impact of using various combinations of atmospheric and oceanic variables on fitting the measured ASCAT-B $\boldsymbol{\sigma}^0$ values for the validation period compared to the use of wind velocity components only can be seen in Figure 22, Figure 23 and Figure 24. The impact in terms of standard deviation of the difference (SDD) between $\boldsymbol{\sigma}^0$ values from the ANN model and the ASCAT-B measurements is shown in Figure 22. The percentage of reduction of SDD compared to the computation of ANN $\boldsymbol{\sigma}^0$ using FG wind only is shown in Figure 23. The correlation coefficients of ANN model trained using various combinations of atmospheric and oceanic variables when compared against the measured ASCAT-B $\boldsymbol{\sigma}^0$ are shown in Figure 24.

The use of extra atmospheric variables improves the performance of the ANN model by up to ~10% reduction of SDD. This is the case of using IFS model forecast surface stress vector (iews and inss), surface roughness (fsr), magnitude of friction velocity (zust), instantaneous 10-m wind gust (i10fg) and large-scale precipitation (lsp) in addition to the usual IFS model FG wind vectors.

For a better visualisation of the impact, the combinations are grouped into three groups, from lower to top in Figure 22, Figure 23 and Figure 24:

- FG wind velocity in addition to others,
- FC surface stress in addition to others,
- Both FG wind velocity and FC surface stress in addition to others.

Table 5: The used atmospheric and oceanic variables (sorted based on the short name).

Variable name	Short name	Units
Charnock	chnk	dimensionless
Convective precipitation	cp	m
Forecast surface roughness	fsr	m
Instantaneous 10-metre wind gust	i10fg	m s^{-1}
Instantaneous eastward turbulent surface stress	iews	N m^{-2}
Instantaneous northward turbulent surface stress	inss	N m^{-2}
Large-scale precipitation	lsp	m
Mean sea level pressure	msl	Pa
Eastward sea water velocity	ocu	m s^{-1}
Northward sea water velocity	ocv	m s^{-1}
Sea water practical salinity	so	psu
Sea surface temperature	sst	K
Total cloud cover	tcc	(0.-.1)
Total column rain water	tcrw	kg m^{-2}
Total column snow water	tcsw	kg m^{-2}
Total column vertically-integrated water vapour	tcwv	kg m^{-2}
Total precipitation	tp	m
Friction velocity	zust	m s^{-1}

In general, the combinations in the group "FG wind & others" (lower) show lower impact than the other two groups. The combinations of the group "FC surface stress & others" (middle) show more impact than members of the "FG wind & others" group. The best results are obtained when both FG wind and FC stress are used in combination of other variables.

In general, the more variables included in the ANN model, the better the results are. However, including a member of each of the following group of variables improves the performance:

- FG (10-m) wind
- Surface stress, friction velocity, gust
- Surface roughness, Charnock parameter
- Precipitation (large scale)

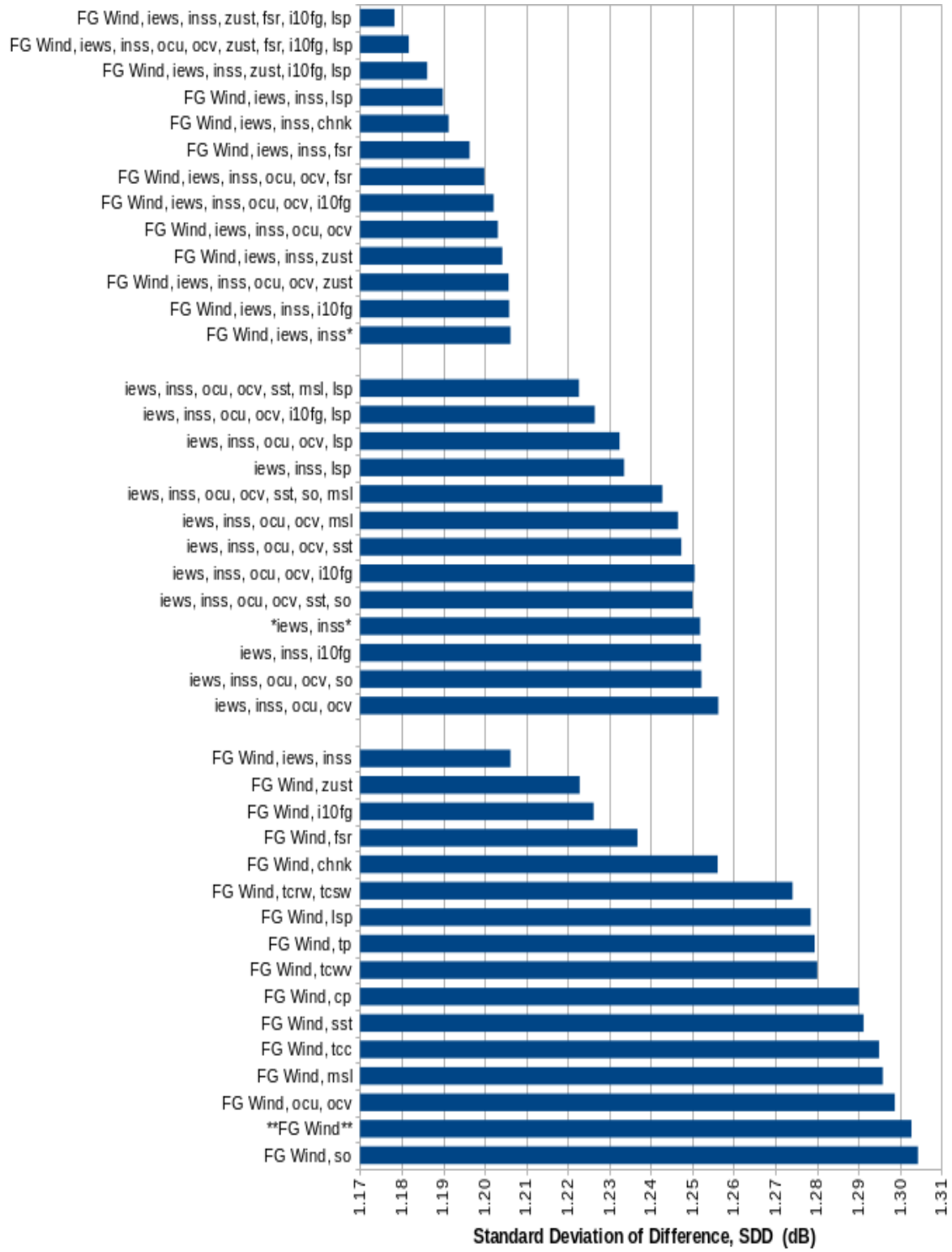

*Figure 22: Impact of using relevant atmospheric and oceanic variables (including FG winds) for training and validating the trained models against ASCAT-B σ^0 measurements in terms of SDD. Training period is between 1 August 2020 and 31 July 2021 while the validation period is between 1 August 2021 to 31 July 2022. The labels next to the horizontal bars represent the combination of atmospheric and oceanic variables used for that model. The label "**FG wind**" refers to the reference FG-wind only model. A list of variable full names is listed in Table 5.*

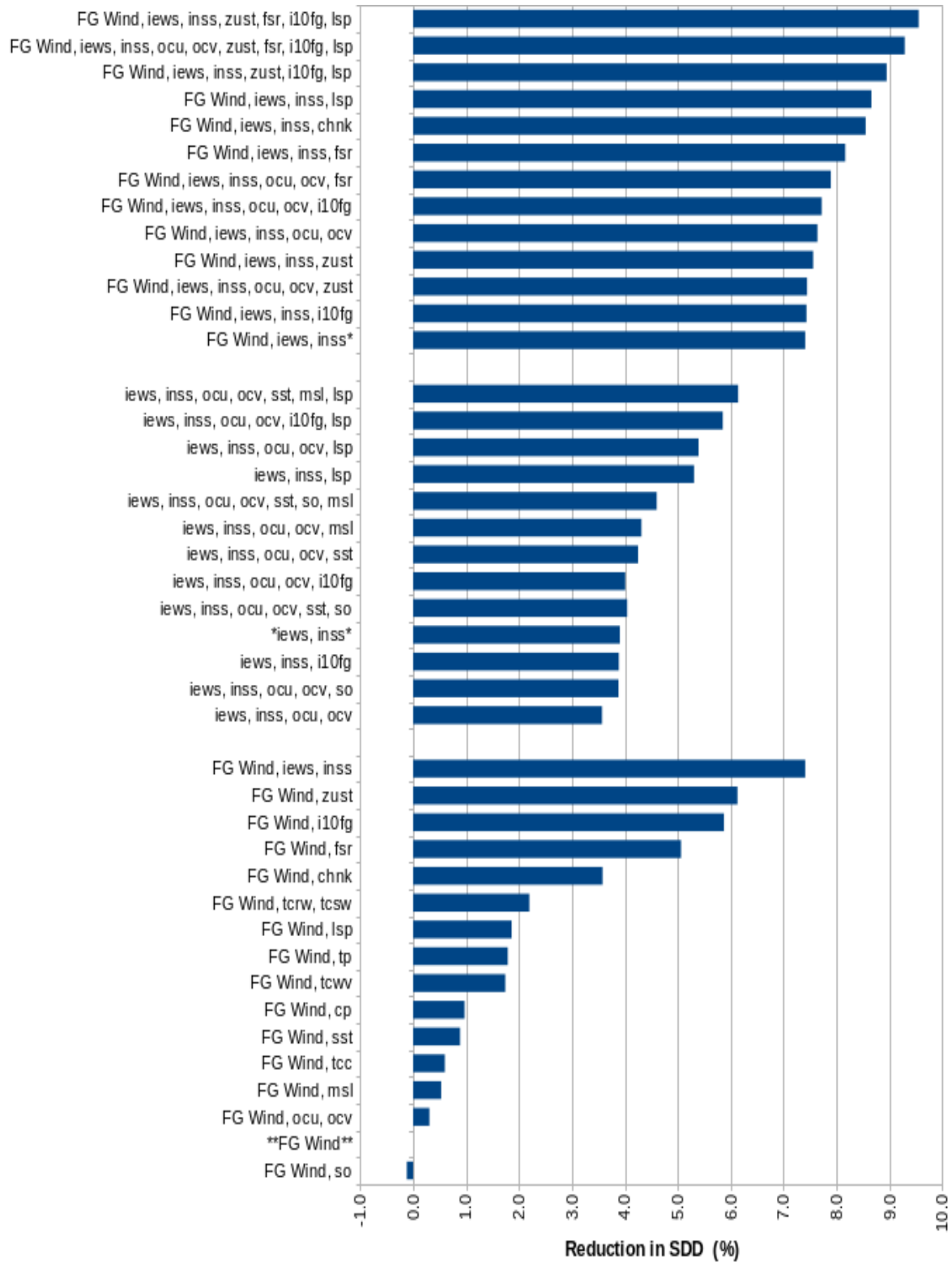

Figure 23: As Figure 22 but the impact is in terms of percentage reduction in SDD.

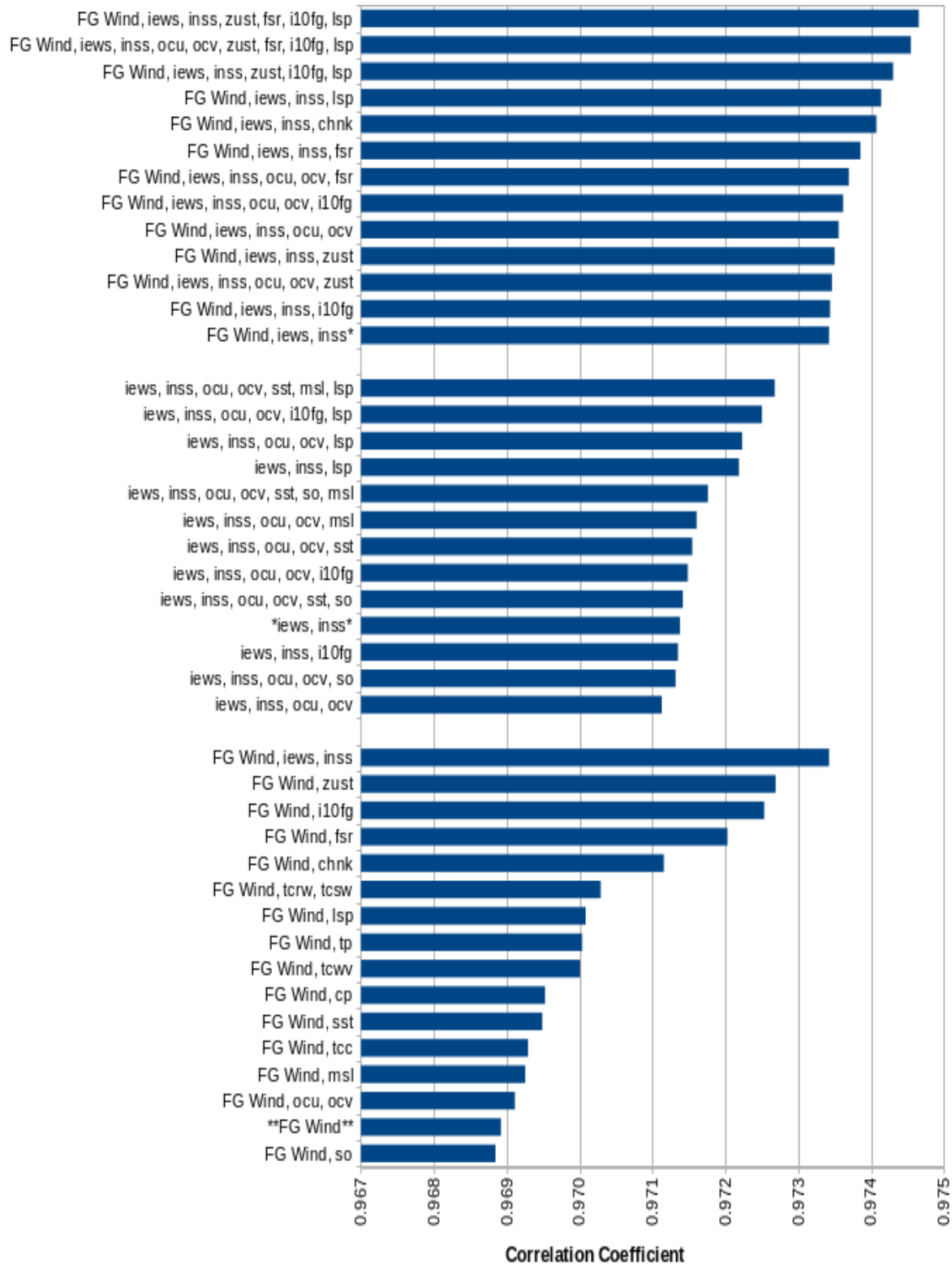

Figure 24: As Figure 22 but the impact is in terms of the correlation coefficient.

It seems that each of those groups includes intrinsic relevant pattern or patterns that complement the patterns in the other groups. The other atmospheric variables, not included in the groups above, introduce minor improvements. It was surprising that adding the oceanic variables, especially the surface current, show almost no impact. Adding the water salinity tends degrade the results slightly. This may be a consequence of the relatively poor ocean model resolution except for the tropical areas.

Figure 25 shows the scatter plot of ANN $\boldsymbol{\sigma}^0$ from FG wind only against ASCAT-B $\boldsymbol{\sigma}^0$ over one year (1 August 2021 to 31 July 2022). Figure 26 shows a similar scatter plot for ANN $\boldsymbol{\sigma}^0$ from the instantaneous surface stress components (iews, inss). Figure 27 shows the same but with adding surface roughness (fsr), magnitude of friction velocity (zust), 10-m wind gust (i10fg) and large-scale precipitation (lsp) to wind and stress vectors. The improvement can be seen by comparing Figure 27 (wind & stress & roughness & precipitation) to Figure 25 (wind only) and even to Figure 26 (wind & stress). The histograms of the three ANN $\boldsymbol{\sigma}^0$ cases: "wind only"; "wind & stress"; and "wind & stress & roughness & precipitation" are compared to the histogram of ASCAT-B $\boldsymbol{\sigma}^0$ and shown in Figure 28. Adding extra atmospheric variables to the wind produces smaller ANN $\boldsymbol{\sigma}^0$ values (below 31.29 dB) as can be seen in Figure 28, especially the lower panel. Nevertheless, those small $\boldsymbol{\sigma}^0$ values are less represented in the ANN models which suggests that there is still room for improvement.

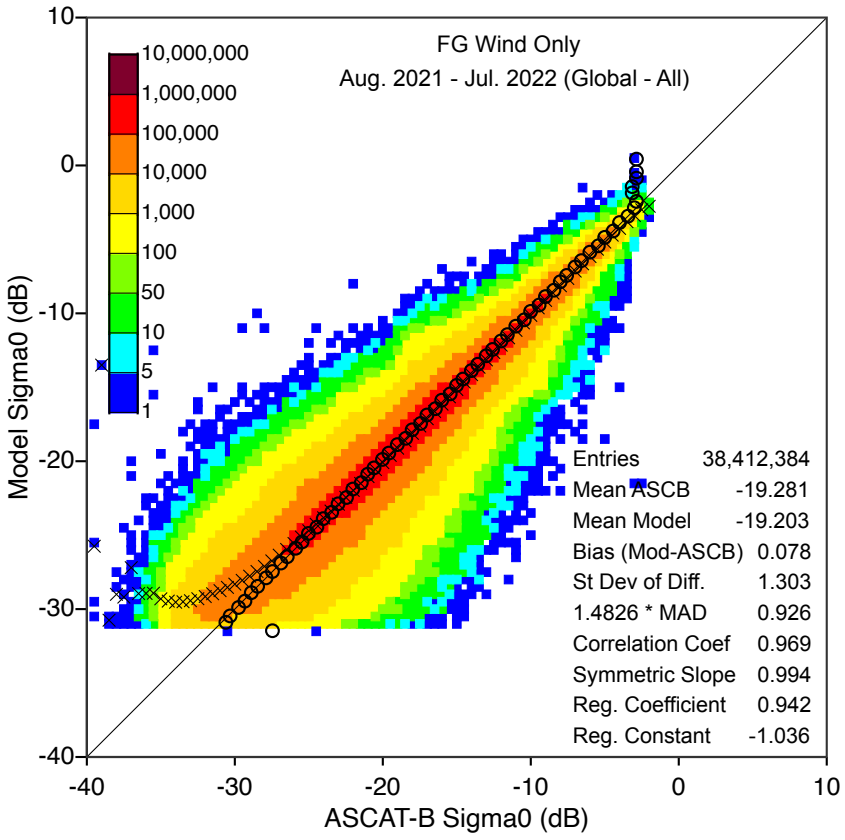

Figure 25: Validation of 12-month (1 August 2021 – 31 July 2022) of the ANN_{FG} model $\boldsymbol{\sigma}^0$ estimates using IFS model FG wind vectors against measured $\boldsymbol{\sigma}^0$ by ASCAT-B. Model training period is between 1 August 2020 and 31 July 2021.

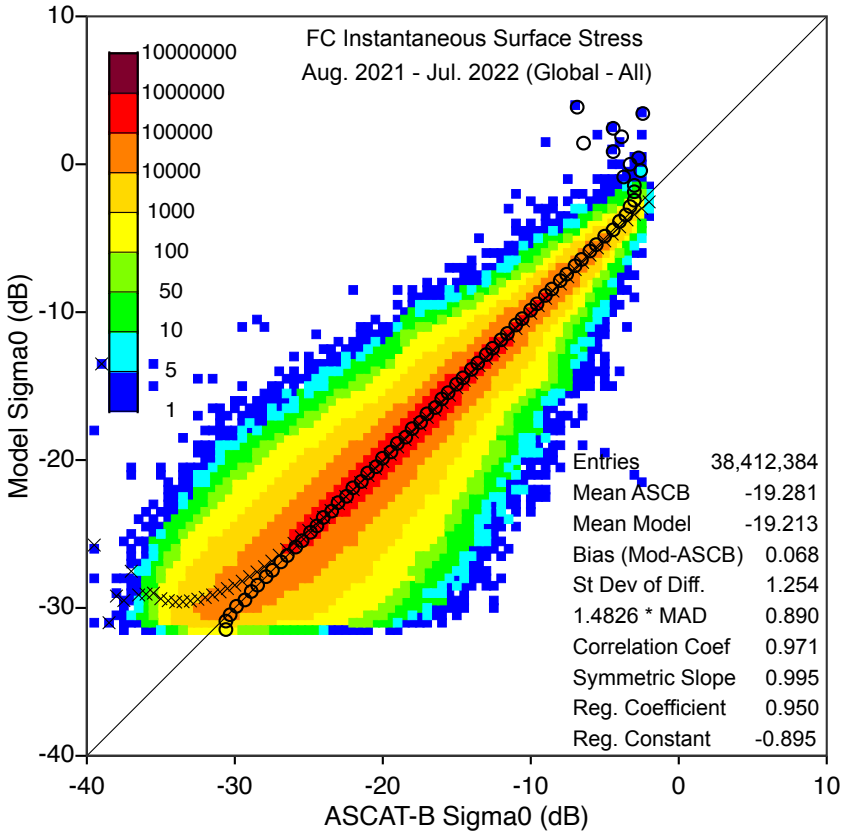

Figure 26: Same as Figure 25 but with the ANN_{FG} model $\boldsymbol{\sigma}^0$ estimates involves IFS model forecast instantaneous surface stress vector (iews and inss).

The geographical distribution of bias between $\boldsymbol{\sigma}^0$ estimated by three ANN models of "wind only" (whose scatter plot is shown in Figure 25); "wind & stress" (whose scatter plot is shown in Figure 26); and "wind & stress & roughness & precipitation" (whose scatter plot is shown in Figure 27) from one side and ASCAT-B $\boldsymbol{\sigma}^0$ measurements, on the other side, over the validation year (1 August 2021 to 31 July 2022) are shown in Figure 29, Figure 30 and Figure 31, respectively. The reduction in bias when more atmospheric variables are added can be clearly seen.

1.5. Discussion

1.5.1. Accuracy of the ANN Models

The value of the standard deviation of the difference (SDD) between $\boldsymbol{\sigma}0$ estimated by ANN models presented earlier and the measured $\boldsymbol{\sigma}0$ varied roughly between 1.0 and 1.3 dB. This seems to be a high value compared to the expected error in $\boldsymbol{\sigma}0$ measured by the ASCAT instruments. Potential contributors to the rather high SDD values are the ANN modelling and the wind used for training and validation.

The same IFS FG wind vector used for the validation of the various ANN models was used for various CMOD geophysical model functions. Note that only wind is used (i.e. the impact of air density was not

considered here). The resulted SDD values compared to ASCAT-B **σ**0 measurements are shown in Table 6. It is clear that the high SDD values are not due to the ANN training.

To demonstrate the impact of wind-speed error on the accuracy of **σ**0 estimation, a simple simulation was carried out by perturbing the model wind speed using Gaussian random noise with standard deviation (SD) of 1.0 m/s (to represent the model forecast error). The wind speed without perturbation is assumed to be the truth in this case. CMOD-5n, CMOD-6 and CMOD-7 GMF's were used to compute **σ**0 from both the unperturbed wind speed (the truth in this simulation test) and the perturbed wind speed. The SDD value from each mode (comparing **σ**0 values from the perturbed wind speed to the wind speed without perturbation) are shown in Table 7. Therefore, 1.0 m/s wind error leads to more than 1.2 dB error in **σ**0 according to various CMOD GMF's. Since the wind speed error of IFS model around 1.0 m/s, SDD in the ANN simulation of 1.3 dB is something to be expected.

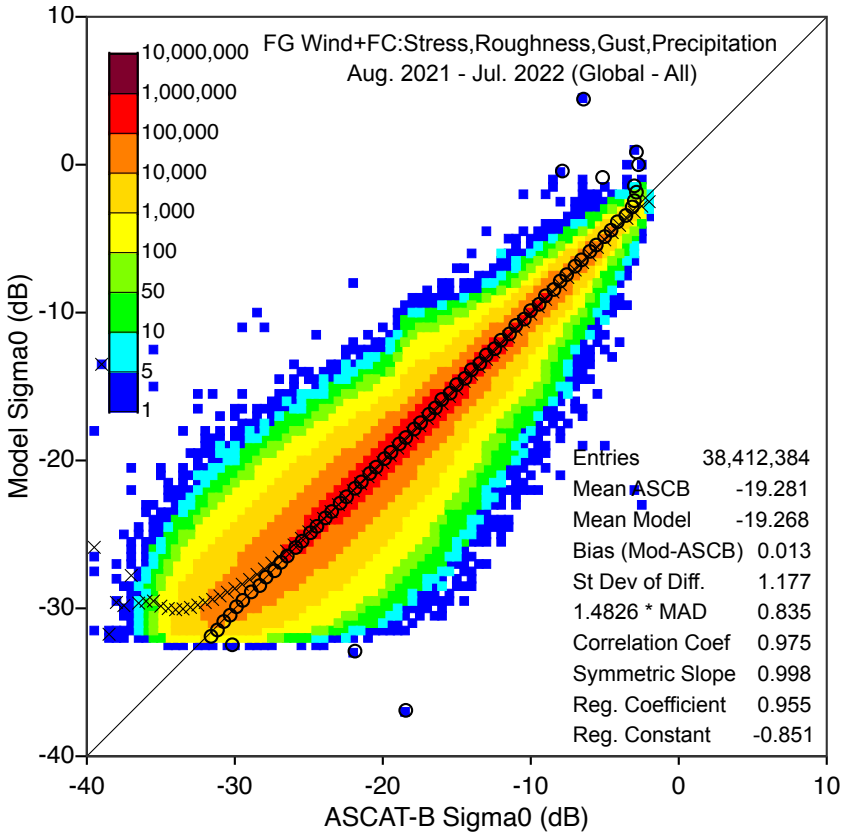

Figure 27: Same as Figure 25 but with the ANN_{FG} model σ^0 estimates involves IFS model forecast instantaneous surface stress vector (iews and inss) as in Figure 26, surface roughness (fsr), magnitude of friction velocity (zust), instantaneous 10-m wind gust (i10fg) and large-scale precipitation (lsp) in addition to IFS model FG wind vectors.

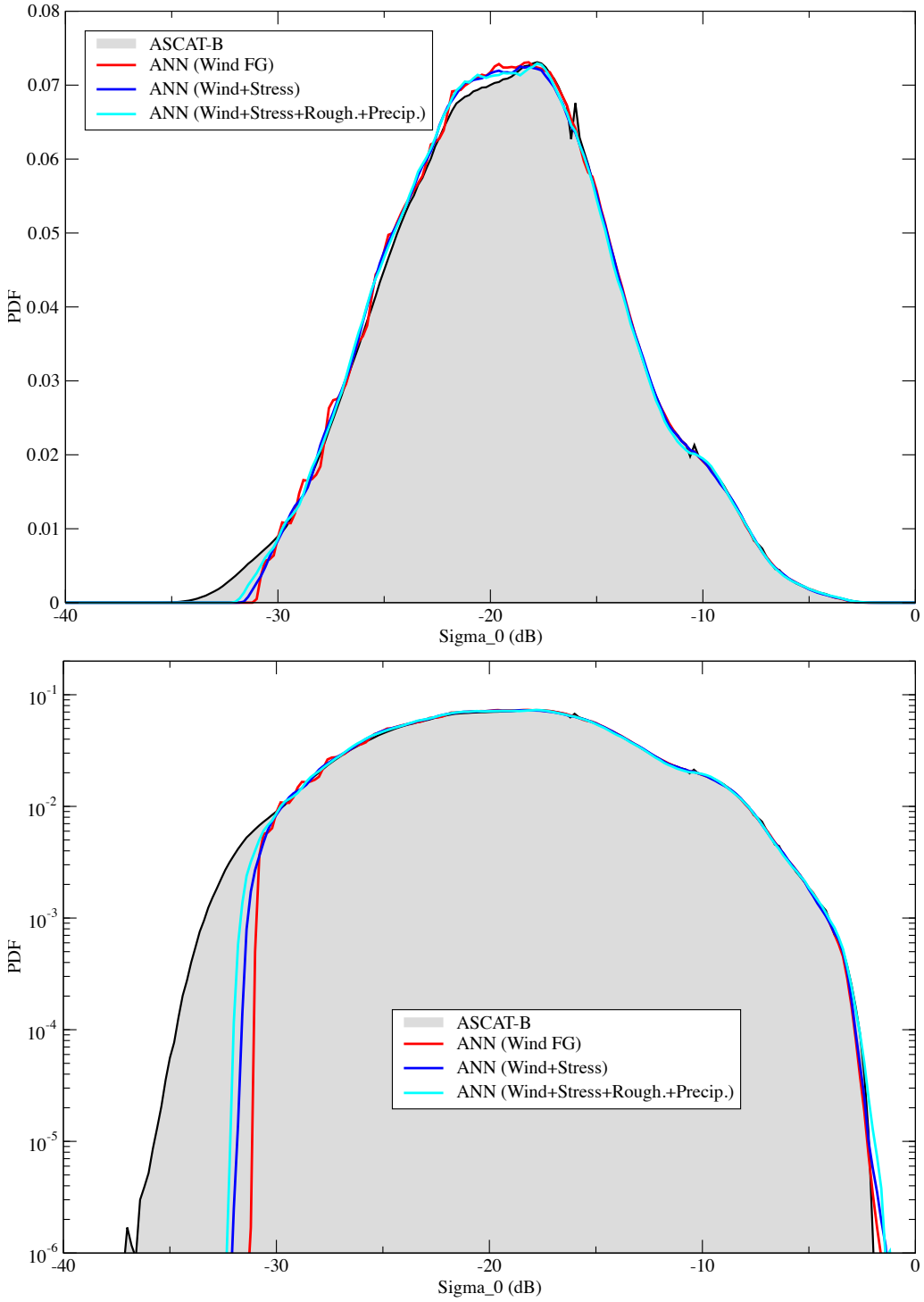

Figure 28: Histograms of ASCAT-B σ^0 measurements (black line and grey-shaded area) for the 1-year validation period (from 1 August 2021 to 31 July 2022). The corresponding histograms from the ANN models that use FG wind vector, and some other atmospheric variables like surface stress vector, surface roughness, … etc. Upper panel shows histograms on a linearly scaled y-axis while the lower panel shows the histograms on a logarithmically scaled y-axis.

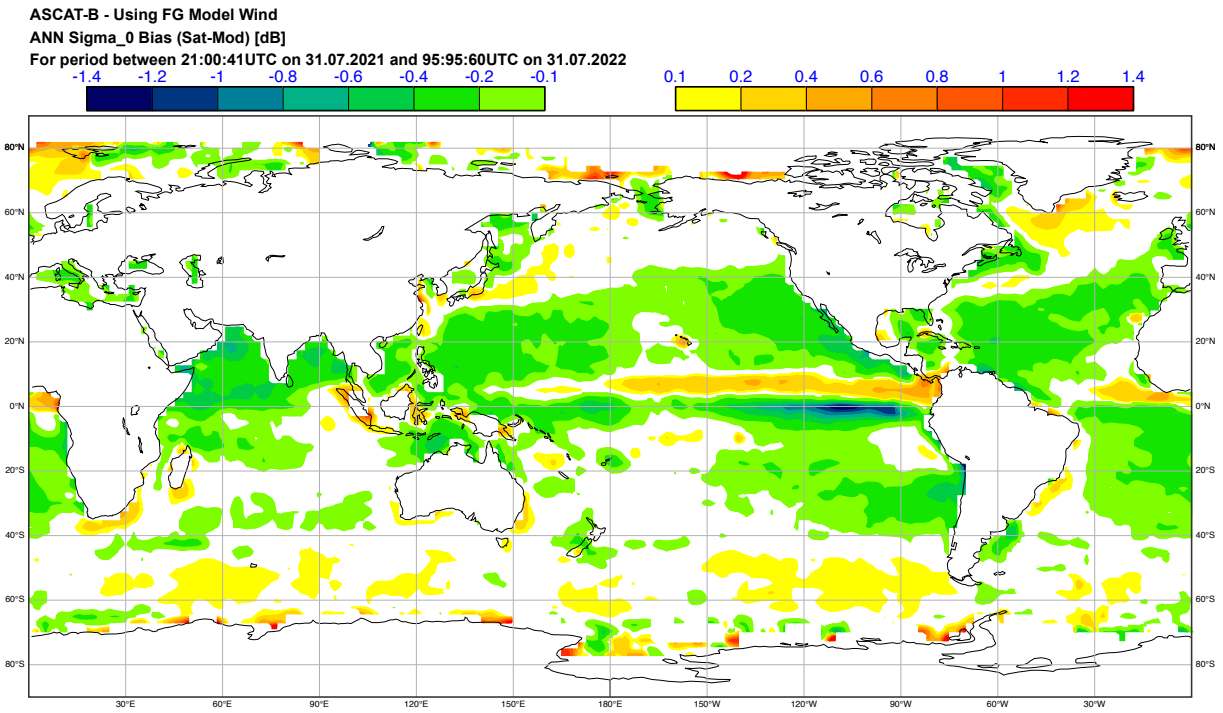

Figure 29: The geographical distribution of bias, in dB, between ANN_{FG} model σ^0 estimates using IFS model FG wind vectors and the measured σ^0 by ASCAT-B during the period from 1 August 2021 to 31 July 2022. Minor differences from Figure 5 are due to slightly different number of collocations.

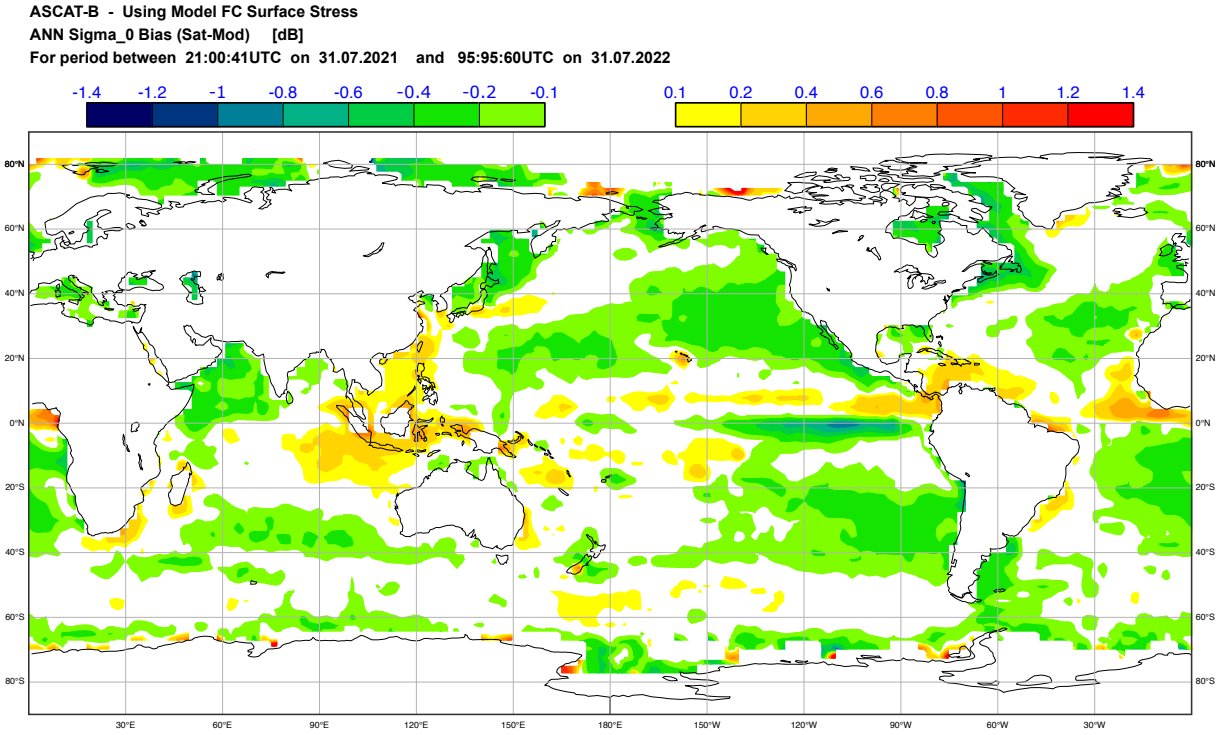

Figure 30: Same as Figure 29 but for the ANN model that was trained using FC instantaneous surface stress vector (iews and inss).

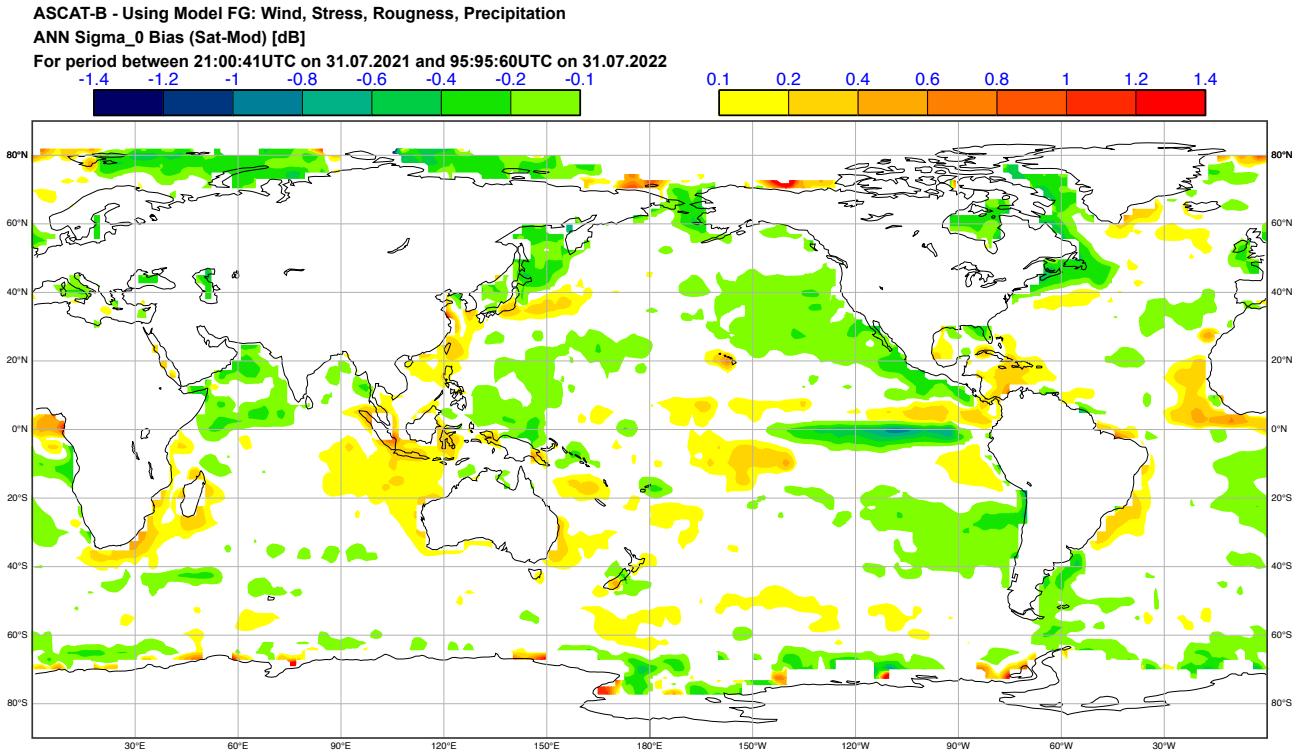

Figure 31: Same as Figure 30 but for the ANN model that was trained using FC surface roughness (fsr), magnitude of friction velocity (zust), instantaneous 10-m wind gust (i10fg) and large-scale precipitation (lsp) on top of those used in the model of Figure 30 (i.e. FG wind vector and FC instantaneous surface stress vector).

Based on the above, one can estimate the wind speed error for model FG to be smaller than 1 m/s and for the model AN to be smaller than 0.8 m/s (a separate simulation similar to the above was carried out by perturbing the wind speed data using random noise with SD of 0.8 m/s resulted in $\boldsymbol{\sigma}^0$ errors similar to those displayed in Table 3 for AN data).

Table 6: Standard deviation of the difference (SDD) of $\boldsymbol{\sigma}^0$ model estimates (using IFS model FG wind vectors) compared to $\boldsymbol{\sigma}^0$ measurements from ASCAT-B.

Model	SDD (dB)
ANN_{FG}	1.3299
CMOD-5n	1.4689
CMOD-6	1.4327
CMOD-7	1.4621

Table 7: Standard deviation of the difference (SDD) of $\boldsymbol{\sigma}^0$ model estimates from perturbed wind speeds compared to $\boldsymbol{\sigma}^0$ estimates from unperturbed wind speeds.

Model	SDD (dB)
CMOD-5n	1.226
CMOD-6	1.226
CMOD-7	1.319

1.5.2. Comparison Against CMOD5N and CMOD7 GMF's

The previous sub-section, in specific Table 6, provided a gross comparison between the ANNFG model and various CMOD GMF's. The ANNFG model is slightly better than the CMOD models evaluated.

Figure 32 shows a comparison of **σ**0 as estimated from ANNFG, CMOD-5n and CMOD-7 against **σ**0 as measured by ASCAT-B for wind vectors aligned with the scatterometer beams (within 2o) for incidence angles of 27o and 59o. In general, the agreement against the ASCAT-B measurements and among various models is quite good. However, contrary to CMOD-5n and CMOD-7 **σ**0 estimates, ANN **σ**0 estimates saturate below ~ 1.5 m/s. There is quite a support for this behaviour in the ASCAT-B data. Furthermore, this behaviour agrees with the available experimental evidence (e.g. [14]) that winds with speeds below a certain threshold (around 2.0 m/s) is unable to produce any perturbation to the water surface. Therefore, the saturation value of **σ**0 could be a result of noise.

The overall errors in the ANN and CMOD-7 estimations of **σ**0, represented in terms of the standard deviation of the difference (SDD) with respect to **σ**0 as measured by ASCAT-B over the whole training year (1 August 2020 to 31 July 2021) are shown in Figure 33. For wind speeds between 3 and 21 m/s, SDD from both ANN and CMOD-7 are very close to each other with SDD from ANN is slightly lower than that of CMOD-7. For wind speeds below 3 m/s, ANN has lower SDD values while for winds above 21 m/s CMOD-7 has lower SDD values. Note that the amount of data with wind speeds below 3 m/s is rather low and above 21 m/s is even lower.

1.5.3. Limitations of the ANN Models

Careful examination of the characteristics of the developed ANN model (appreciation to EUMETSAT) revealed that there are few shortcomings:

- The underestimation of high winds.
- Nonsymmetric behaviour of the observation operator around the 0º/360º edge (lack of periodicity).
- The non-physical undulations especially at extreme incidence angles and wind speeds.

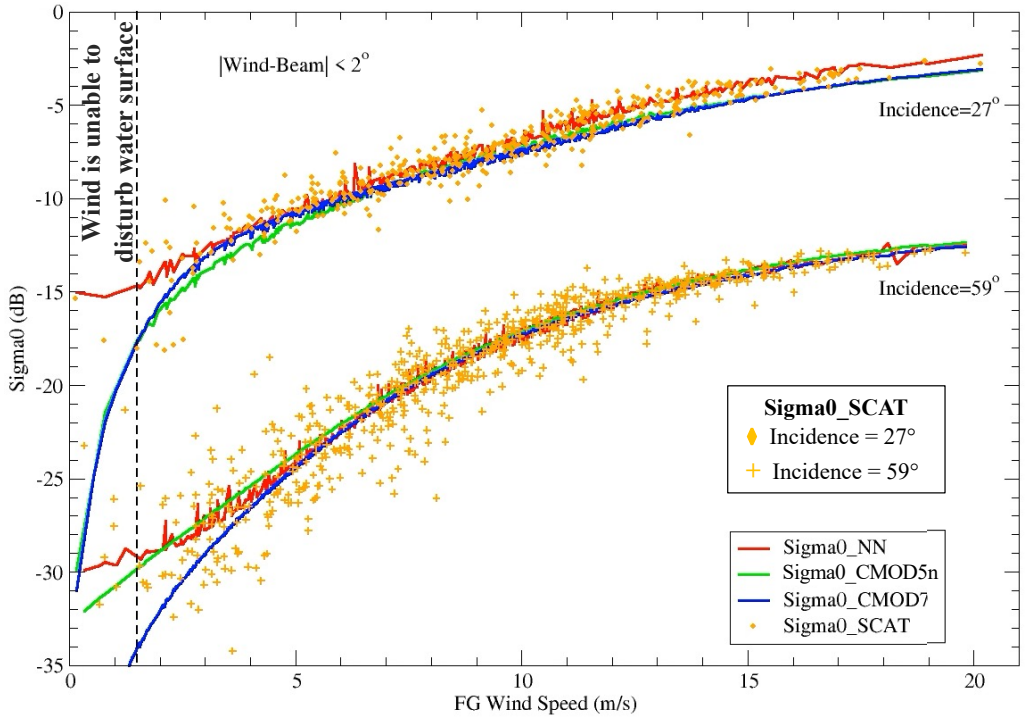

Figure 32: Comparison of σ^0 as estimated from ANN_{FG} (Sigma0_NN in the plot), CMOD-5n and CMOD-7 with σ^0 as measured by ASCAT-B (Sigma0_SCAT in the plot) for wind vectors aligned with the scatterometer beams (within 2°) for incidence angles of 27° and 59°.

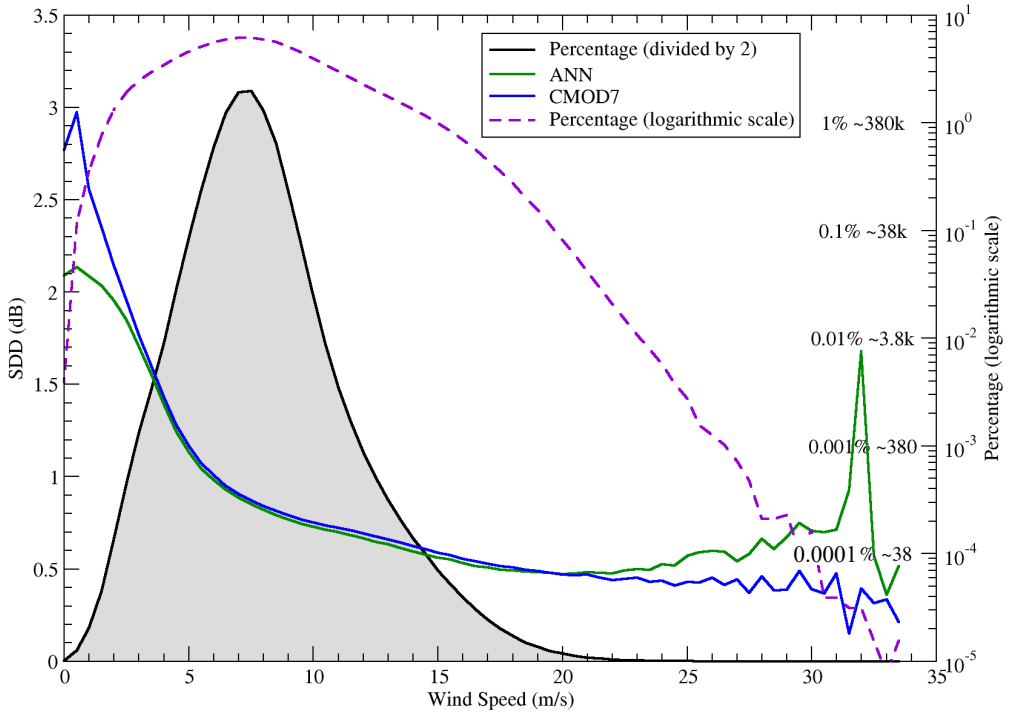

Figure 33: Standard deviation of the difference (SDD) between model σ^0 from ANN and CMOD7 compared to ASCAT-B as functions of wind speed. The PDF (as percentage of the data) of wind speed is plotted both on a linear y-axis and a logarithmic y-axis (both on the right-hand side of the plot).

Underestimation of High Wind Speeds:

There are 3 factors that contribute to the underestimation of high wind speed issue:

1. There are few observations available at wind speeds of 20 m/s and above as can be seen in Figure 34. About 0.3% of the data are wind speeds exceeding 20 m/s (see PDF in Figure 33). This issue can be alleviated by adding more observations in that regime. Increasing the period of the training data to cover multiple years is one option. Using data from both ASCAT-B and ASCAT-C for training could help. Another possibility is to use simulated data by using CMOD-7, for example. In any case, one needs to be careful to respect the distribution of the wind speed.
2. The IFS model tends to underestimate high winds compared to CMOD-5n or CMOD-7 as can be seen in Figure 35. This issue can be alleviated by bias correcting IFS model wind speeds, especially at high winds.
3. The ANN training seems to be not able to reproduce the targets very well towards the edge of data domain (we can call this the edge effect). Although more data near the edge could help, it is not clear what a good solution to this issue could be.

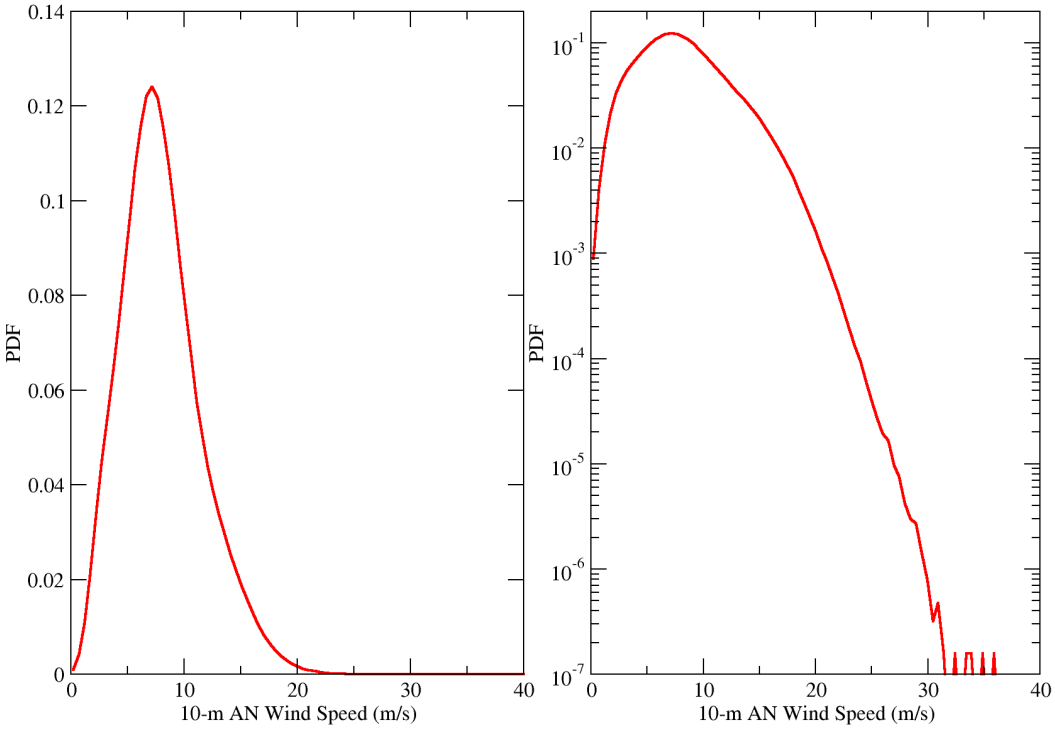

Figure 34: The probability density function (PDF) of the wind speed of the training data set. Left-hand side panel shows the PDF plotted using a linear y-axis while the right-hand side panel shows the same PDF plotted using a logarithmic y-axis.

Nonsymmetric Behaviour of the ANN Observation Operator:

The azimuth angle (with respect to North) and the absolute wind vector (components in east-west and north-south directions) were used as two features in training. The basic mathematical fact of periodicity (angles between 0° and 360° are repeated beyond 360°) of the azimuthal angle was not introduced to the ANN training. This caused some deviation between simulated sigma0 at azimuth angles of 0° and 360°. This issue can be sorted out by repeating the observations at the edges (0° and 360°) as follows:

- data with small angles are repeated beyond 360°;
- data with large angles (below 360 degrees) are repeated below 0°.

That safeguards the azimuth angle range between 0°-360° and ensures periodicity.

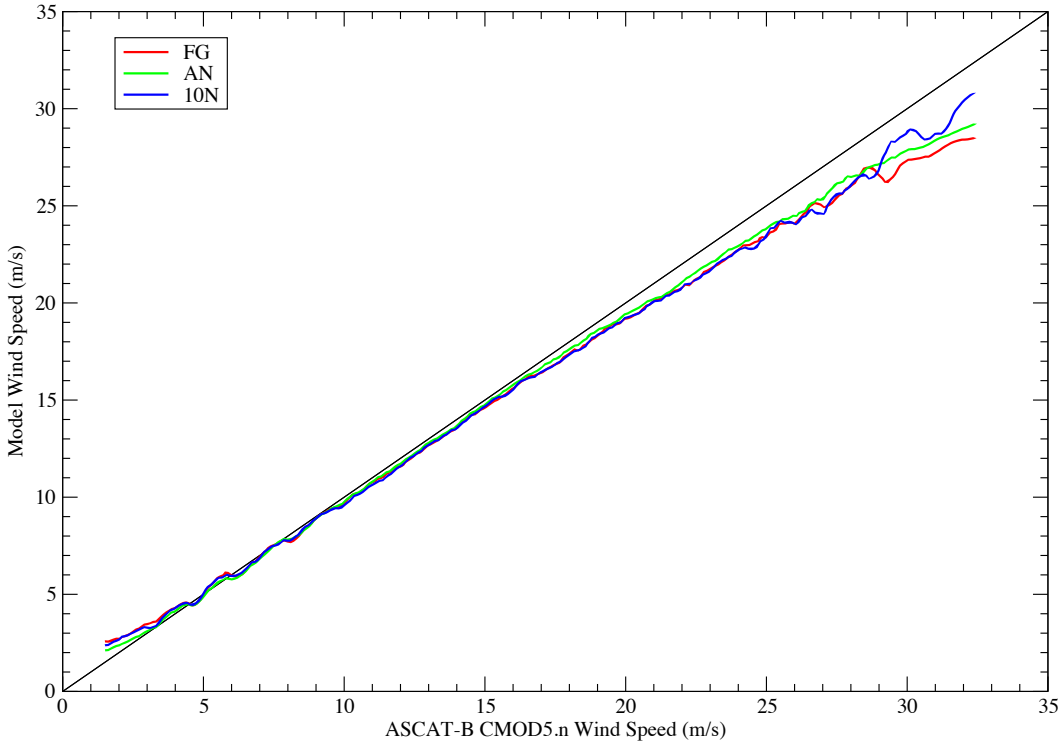

Figure 35: Comparison between the mean IFS model 10-m wind (from FG, AN and neutral FC wind) against wind speed from ASCAT-B CMOD5.n wind. Global wind covering the period from 1 August 2020 till 31 July 2021.

Non-Physical Undulations at Extreme Incidence Angles and Wind Speeds:

This issue seems to be mainly due to the edge effect (incidence angles and wind components). Using more data with extreme incidence angles and/or wind speeds for training could help. This issue needs further investigation (beyond this study).

1.5.4. Comparison Against PARMIO Model

We obtained the code for the Passive and Active Reference Microwave to Infrared Ocean (PARMIO) model [13]. After having it running, several model configurations were changed in order to produce results that are comparable to the scatterometer data. Figure 37 shows the variation of $\boldsymbol{\sigma}^0$ estimated by PARMIO model for C-band with respect to the wind speed for various incidence angles. The comparison between $\boldsymbol{\sigma}^0$ estimated by ANN^{FG} and that by PARMIO model for several incidence angles is shown in Figure 38. The comparison does not look very good. It seems that having PARMIO model working properly needs more work and experience that what we have available for this project. Furthermore, the outcome of this comparison will not contribute to the aims of this project. Therefore, we decided not to pursue this effort any further.

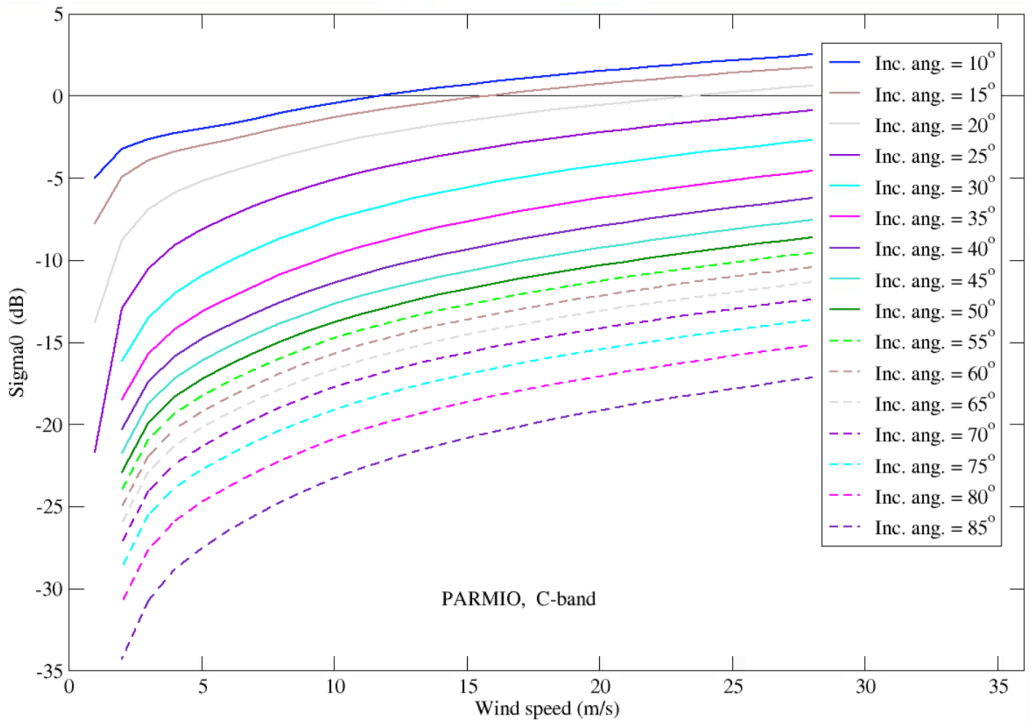

Figure 36: The variation of $\boldsymbol{\sigma}^0$ estimated by PARMIO model for C-band with respect to the wind speed for various incidence angles.

1.6. Conclusions

Artificial neural networks (ANN) is an attractive tool that can be used to develop numerical models based on the data without the need for a deep understanding of the detailed physical laws. Its flexibility to include extra features (input variables) with minimal effort is another strength.

A database consisting of collocations of ASCAT-B and ASCAT-C backscatter coefficients, $\boldsymbol{\sigma}^0$, and the corresponding ECMWF IFS model wind vectors and other related variables covering a period of more than 30 months was constructed for training and validation of the developed ANN models.

With $\boldsymbol{\sigma}^0$ as the target, ANN models based on first-guess (FG) surface wind vectors, analysis (AN) surface wind vectors and combinations of wind vectors and other variables as features were trained and validated. In general, 1-year of ASCAT-B data (together with their model collocations) were reserved for training. The rest of the data as well as the whole ASCAT-C data were used for validation. The 1-year of training data was needed to cover most of the atmospheric conditions.

ANN models, irrespective of being trained against FG or AN wind, were successful in predicting $\boldsymbol{\sigma}^0$ values for the data which they have not seen before. They compare very well with the values retrieved using different CMOD GMF's. ANN models based on wind vector only were not able to produce any $\boldsymbol{\sigma}^0$ values below 31.29 dB. This turned out to be the regime of wind speed below ~1.5 m/s, which is known to be the wind speed threshold value to produce any water surface gravity-capillary waves. This is the scale capable of generating a backscattering radar signal. ANN models based on wind vector and sea-state variables could produce $\boldsymbol{\sigma}^0$ values below 31.29 dB. This is an indication that such backscatter values are not produced by wind but other processes like the ocean swell.

The value of the standard deviation of the difference (SDD) between $\boldsymbol{\sigma}^0$ estimated by ANN models presented earlier and the measured $\boldsymbol{\sigma}^0$ varied roughly between 1.0 and 1.3 dB. This rather high value is due to the accuracy of the IFS model wind.

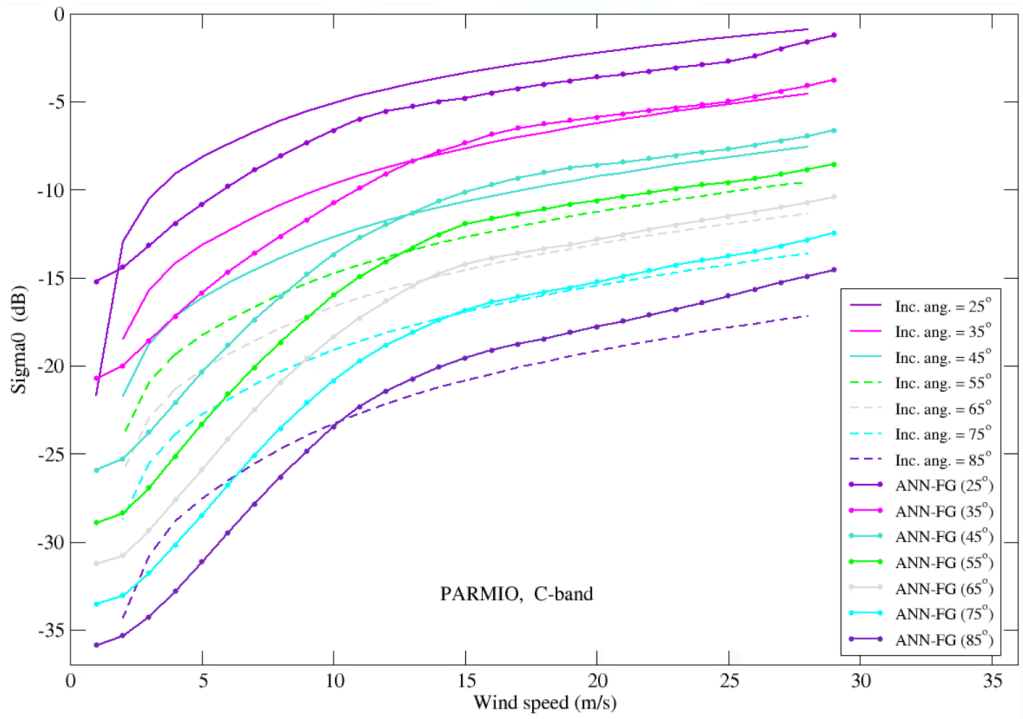

Figure 37: The comparison between ANN_{FG} and PARMIO $\boldsymbol{\sigma}^0$ estimates for various incidence angles.

1.7. Annex to Section 1

The geographical distribution of the IFS mean surface wind over one year from 1 August 2021 to 31 July 2022 is shown in Figure 38 for reference.

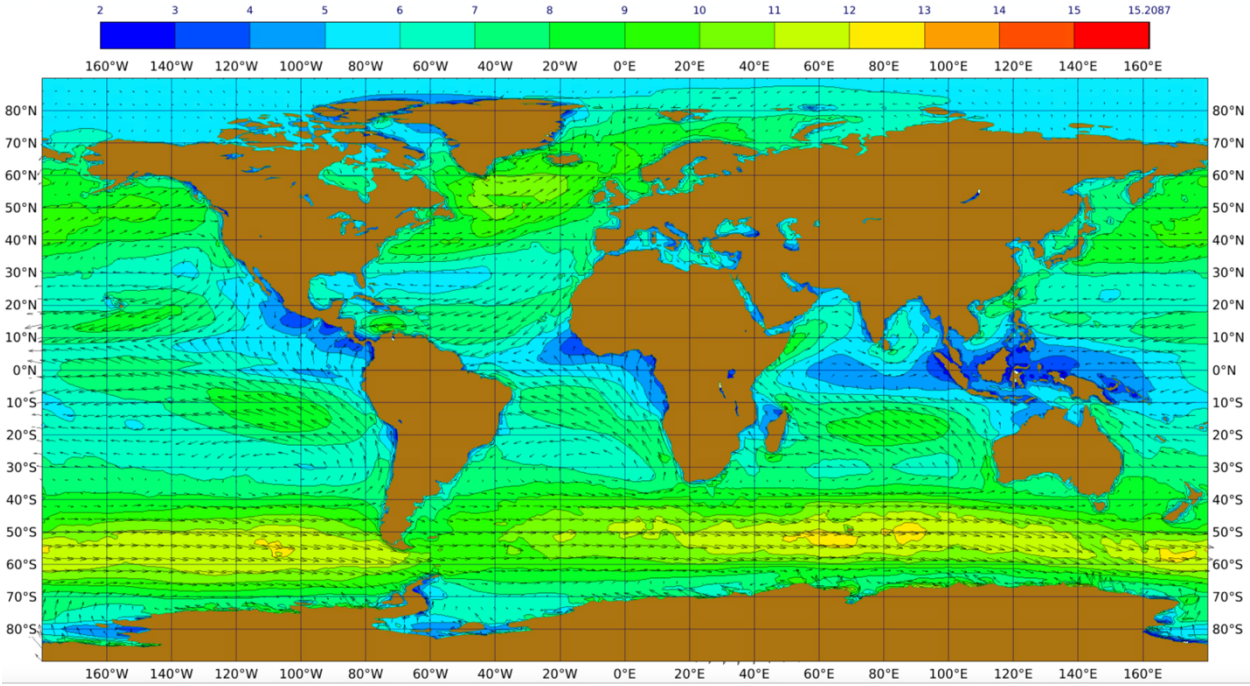

Figure 38: The geographical distribution of the IFS mean surface wind over one year (1 August 2021 – 31 July 2022).

2. The development of the ANN Radar Altimeter Wind Retrieval Algorithm (WP 2)

2.1. Introduction

Information about the surface wind velocity is very valuable for oceanic and atmospheric applications. Apart from its own applications, surface wind velocity is one of the most important driving forces for ocean waves and circulation.

Ocean surface wind generates ripples on the water surface. The stronger the wind is, the steeper the ripples are. These ripples diffuse radar, or any electromagnetic, signal that hits such surface. This can either enhance (for inclined signal) or reduce (for a nadir signal) the power of the backscattered signal. Therefore, there is a strong (direct or inverse) relation between the surface wind speed and the backscattered signal. This relation is not exclusive and is not known precisely. Therefore, empirical algorithms have been used for this purpose so far (e.g. [2] [19] [21] [22] [31] [36] and [37]).

A radar altimeter (RA) instrument is a nadir looking active device that is capable of measuring, with high precision, the time delay, the power and the shape of the radar pulses after reflection, called waveform, from the Earth surface. The time delay is proportional to the altitude of the instrument. The power and the shape of the reflected signal contain information on the characteristics of the surface that caused the reflection. Over the ocean, the shape of the waveform can be translated into significant wave height (SWH), H_s, while its power (the backscatter coefficient, σ^o) can be translated into ocean surface wind (defined here as the wind speed at a height of 10 m above the mean sea surface, U_{10}). Several satellites carrying RA instruments were launched during the last few decades. The list includes Jason-3, Sentinel-3A/B and Sentinel-6A. All those platforms carry at least a Ku-band (or Ka-band) altimeter. Most of satellites like Jason and Sentinel-3/6 families carry a second altimeter operating with a different radar frequency (usually at C-band). Hereafter, only Ku-band altimeter from Sentinel-6A is considered. The approach can be extended to other altimeters and may be generalised as well but that is beyond the scope of this work.

Although there are several satellite-borne instruments capable of measuring higher density wind vector fields across rather wide swath (e.g. scatterometers), RA wind speed is still of great value for several applications like the correction of the altimeter estimate of mean sea surface height (e.g. the electromagnetic bias correction). RA wind speed data are very useful for monitoring the quality of model wind speeds. For example, at the European Centre for Medium-Range Weather Forecasts (ECMWF) the scatterometer (ambiguous) wind vectors from Metops-B/C (ASCAT-B/C) are assimilated in the atmospheric model. Therefore, these sources of data cannot be used for totally independent verification of the model winds.

The history of the empirical models for translating Ku-band RA backscatter into ocean surface wind speed goes back to 1980's. The modified Chelton-Wentz (MCW) algorithm proposed by [36] was one of the mostly used in operational retrieval algorithms. It was adopted for several altimeters like the ones onboard TOPEX, ERS-1/2 and ENVISAT (before late October 2005). The algorithm, which was devised based on a limited number of GEOSAT altimeter-buoy collocations, consists of a look-up table

relating U_{10} to σ^o. Although this algorithm is generally performing rather satisfactorily, it was always felt that there was room for improvement. Some improvement attempts refined the existing one-variable algorithm (e.g. [19]) while others tried to introduce a sea-state dependence by including the measured H_s as a second variable (e.g. [22]) in retrieval algorithms. The sea-state dependence itself was the subject of several research efforts (e.g. [21] and [26]). The results of those studies show ranges of impacts from significant to no impact (e.g. [37]).

Artificial neural networks (ANN) approach was used by [22] to develop their two-variable algorithm. Due to its flexibility and the fact that a functional form is not needed, ANN is the chosen approach for training in this work.

2.2. Data Used

Near-real time (NRT) Sentinel-6A conventional Low-Resolution Mode (LRM) altimetry data in BUFR format have been retrieved from EUMETSAT and archived at the ECMWF archiving system since 17 June 2022. Only 1-Hz are considered for this work. From the experience gained from WP1 (scatterometer observation operator training), one full year of data is needed for proper training without introducing biases. So, the data covering the period from 17 June 2022 to 17 June 2023 are reserved for ANN training. The remaining data (from 17 June to 11 December 2023) are used for independent validation of the trained models. Although the period for the validation is not perfect since it does not cover a full year, it should give a good indication on the performance of trained ANN models.

Sentinel-6A LRM 1-Hz data are grouped in 6-hourly windows centred on 00, 06, 12 and 18 UTC. ECMWF model analysis fields of wind velocity at 10-m height are retrieved from the ECMWF Meteorological Archival and Retrieval System (MARS) [15] for the same time windows (each model field is valid at the middle of its corresponding 6-hour window). Linear interpolation both in space and time is used to estimate the model value at each observation. 10-m wind speed, U10, is computed from the interpolated wind velocity components.

The BUFR version of the data does not contain any reliable indicator of the quality of the altimeter data.

2.3. ANN Model Configuration

An Artificial Neural Network (ANN) model of wind retrieval from radar altimeter measurements like backscatter ($\boldsymbol{\sigma}^0$) has been developed using Keras/TensorFlow ([4] and [1]) package. The following altimeter measurements were considered:

- Ku-band
  - backscatter, *sigma0*;
  - Standard deviation (SD) of sigma0, *sigma0sd*;
  - significant wave height (SWH), *swh*;

  - SD of SWH, *swhsd*;
  - SD of range, *rangesd*;
- C-band
  - backscatter, *csigma0*;
  - SD of sigma0, c*sigma0sd*;
  - SWH, c*swh*;
  - SD of SWH, c*swhsd*;
  - SD of range, c*rangesd*;
- Mis-pointing of altimeter from nadir as derived from the trailing edge of the Ku-band waveform, also known as offnadir angle, *offnadir*.

Sigma0 (Ku-band backscatter) was either considered alone or with one or more of the remaining altimeter measured variables as the input variables ("features"). The collocated ECMWF model analysis 10-m wind speed is the ANN model output "target".

ANN training is equivalent to the traditional algorithm fitting (e.g. [2]) but with more flexibility and without the need of the precise knowledge regarding the underlying physics nor the functional form of the dependence. Once enough existing features-target data are available, the ANN can extract the relation (~physical laws) between the targets and the features. In fact, ANN only figures out the "pattern" in the data. Therefore, the found "relation" cannot be written in a closed form. However, ANN model parameters are produced and stored for later usage for verification and implementation of the model.

The following ANN configuration is used:

- A Sequential ANN model is used since it is most appropriate for a plain stack of layers where each layer has exactly one input tensor and one output tensor (https://keras.io/guides/sequential_model/).
- The input layer is composed of one or more input nodes depending on the used features (one node for each feature).
- Two identical hidden dense layers are implemented. The "dense layer" is a term used to describe a layer of nodes with each node receiving input from all the nodes of the previous layer.
- Each layer is composed of 32 nodes.
- The activation function transforms the input to the output (also called activation) at the node level. Linear activation functions are easy to implement and execute. However, to learn complex mappings, nonlinear activation functions are required. The activation function used for altimeter wind is the rectified linear (ReLU) activation function which is a piecewise linear function that will output the input directly if its argument is positive, otherwise, it will output

zero. Its derivative is 1 for positive arguments and zero otherwise. These characteristics make ReLU the favoured activation function for many types of neural networks.

- The output layer is composed of a single node representing the 10-m wind speed, U_{10}.
- The loss function, which is the equivalent term for the cost function in data assimilation, is the sum of the (square of) errors to be minimised. ANN model training is achieved through an optimisation of the loss function. The loss is represented by the mean square error (MSE), which is the average of the squared differences between the predicted and actual values.
- The optimisation algorithm (optimiser) is selected as the stochastic gradient descent (SGD) which is a very efficient optimiser.

Summary of altimeter wind ANN model configuration is listed in Table 8.

Several deviations from the above configurations were considered. Networks that include 2 hidden layers with 16, 32, 64 and 128 nodes as well as 3 layers with 64 and 32 nodes were tested. The impact was marginal and, therefore, for the sake of efficiency and accuracy we decided to use the above configuration in terms of layers and nodes.

Table 8: Summary of altimeter wind retrieval ANN model configuration.

Model Elements	**Description**
Model type	Sequential
Number of layers	1 input, 1 output and 2 hidden (configurations with 3 hidden layers were tested)
Type of hidden layers	Dense
Number of nodes	32 for each hidden layer (other number of nodes were tested)
Activation function	rectified linear (ReLU)
Input layer	Several configurations were tested from a single node with sigma0 only up to 10 nodes (one for each feature)
Output layer	1 node for wind speed (the target)
Loss function	Optimisation of mean square error (MSE)
Optimiser	Stochastic gradient descent (SGD)

2.4. Data Cleaning

This step was not necessary for scatterometer ANN models since clean data sets were used as they were composed of the data that had passed quality control and were used for data assimilation. The situation for the altimeter data is different. The initial trial was to use all the data without much cleaning (only obvious cleaning like rejecting missing or nonphysical values). As can be seen in Figure 39, the results were very disappointing, especially for low backscatter values which should result in high winds. In fact, running mean along the measured backs scatter values (after sorting ascendingly) would give very close result. The reason is that there is a limited number of observations corresponding to high winds. The erroneous data deteriorate the signal-to-noise ratio and confuse the training process.

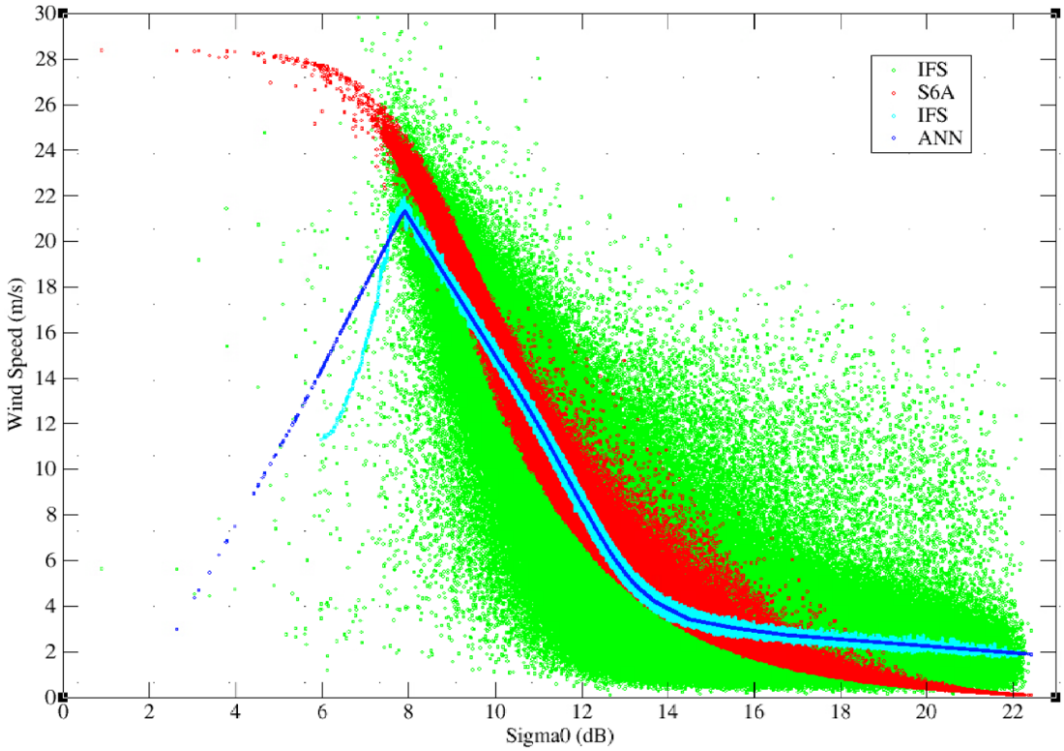

Figure 39: Sentinel-6A Altimeter σ^0 versus model 10-m wind speed from the ECMWF model (green dots) official Sentinel-6A product (red dots), an ANN model that uses all the data (blue dots). The running average of ECMWF model wind speed along Sigma0 is also shown (cyan dots).

Unfortunately, we could not find reliable quality flags in the BUFR version of Sentinel-6A data to make use for the rejection of bad data. Therefore, we had to develop a data cleaning procedure to improve the signal-to-noise ration of the data especially at high winds (low backscatter).

The following data cleaning procedure produced satisfactory results:

1. Remove records with missing, zero or unphysical values of vital data (Specifically: Sigma0 and its SD, SWH and its SD, SD of the range and the offnadir angle)

2. Remove the observation when it shows signs of noise:
    a. SD of Ku-band SWH > 1.0 m
    b. SD of Ku-band Sigma0 > 1.5 dB
    c. SD of Ku-band range > 0.12 m
    d. Noise along the track.
3. Distribute the data over a grid of altimeter SWH – model wind speed which are the most influential variables for wind speed retrieval.
4. Compute the mean (M) and the standard deviation (SD) of Ku-band Sigma0.
5. Discard all records with Sigma0 values outside the range between M - $\boldsymbol{\alpha}$ SD and M + $\boldsymbol{\alpha}$ SD (several values between 1 and 3 were tested for $\boldsymbol{\alpha}$ and finally the value of 2.2 was selected).
6. Repeat steps 3-6 with the data accepted so far. 20 iterations are used but in general ~10-12 iterations are usually enough as can be seen in Figure 40.

Although this procedure was not fully optimised, we did not find that there is a need for fine tuning.

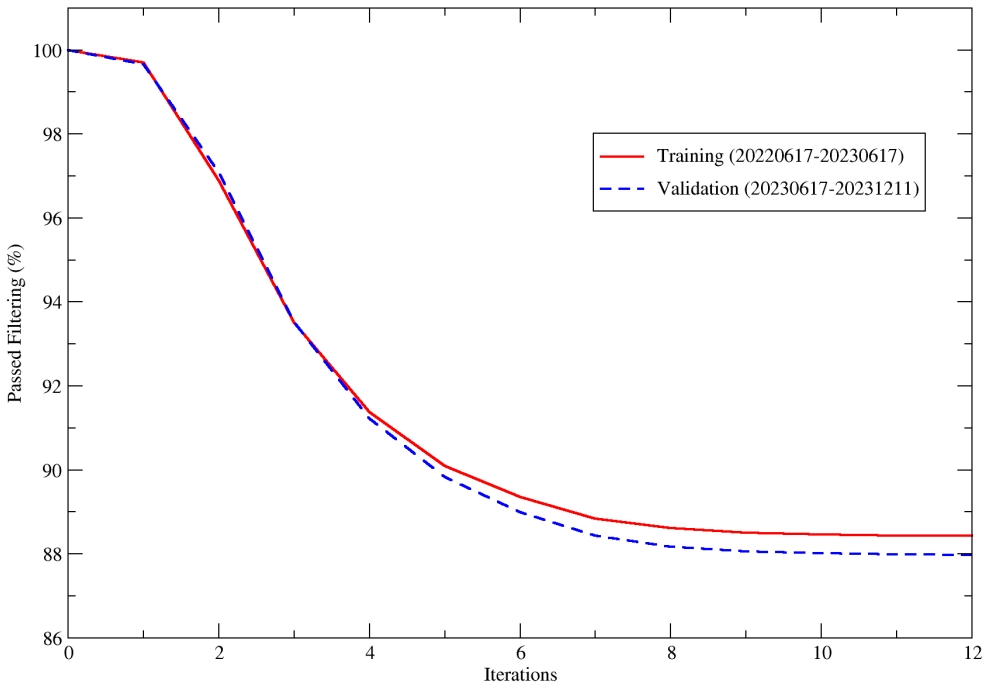

Figure 40: Percentage of Sentinel-6A data that pass filtering.

The impact of data cleaning can be clearly seen in Figure 41 which shows the standard deviation of the difference (SDD), which is a proxy of the random error, of official Sentinel-6A altimeter surface wind speed compared to IFS model during the period from 17 June to 11 December 2023. The upper panel of Figure 41 is plotted using the filtered data while the lower panel is plotted using the unfiltered data.

The filtered data (upper panel of Figure 41) show smaller areas with SDD values exceeding 1.6 m/s (yellow, orange, red) and larger areas with SDD values below 0.9 m/s (shades of blue) compared to the unfiltered data case displayed in the lower panel of Figure 41.

2.5. Results

2.5.1. ANN Model Utilising Sentinel-6A Sigma0 and SWH

An ANN model was trained using Sentinel-6A backscatter (Sigma0) and significant wave height (SWH) as input features and ECMWF model 10-m wind speed analysis over the period of training (one year running from 17 June 2022 till 17 June 2023). This choice was made to reflect the fact that both Sigma0 and SWH were used to fit the model used for wind speed computations in the official Sentinel-6A product.

Figure 42 shows wind speed comparison between Sentinel-6A altimeter and ECMWF model analysis over the whole global ocean during the period from 17 June to 11 December 2023 (independent validation period). The upper panel of Figure 42 is for Sentinel-6A wind data from the ANN model trained using Sentinel-6A Sigma0 and SWH for the period from 17 June 2022 to 17 June 2023 while the lower panel is for the official Sentinel-6A product (which was derived using Sigma0 and SWH). Only filtered data are used for both plots in Figure 42. The improved agreement between Sentinel-6A ANN data and the ECMWF model can be visually observed from the pattern of the data clouds in both plots of Figure 42. While the centre of gravity of the ANN cloud represented by the circles in the upper panel is aligned across the symmetric (45° line) line, the centre of gravity of the official product cloud represented by the circles in the lower panel shows visible deviations from the symmetric line.

Quantitatively, when validated against ECMWF model wind, the ANN model shows slightly lower bias, standard deviation of difference (SDD), which is a proxy to the random error, and scaled (i.e. multiplied by 1.4826) median absolute deviation (MAD), which is another proxy of the random error, and slightly higher correlation coefficient compared to the same statistics from the official wind Sentinel-6A product (as can be seen in the offset of the two plots in Figure 42). It is worth mentioning that only filtered data are used in both plots of Figure 42. Although the filtering procedure was able to discard a large number of outliers, some isolated outliers as well as a cloud of a small number (few hundreds out of 4 million) of outliers for model wind speeds of less than 8 m/s still exist.

Maps of the SDD between Sentinel-6A and the ECWMF model winds are shown in Figure 43. The upper panel shows the wind SDD for the ANN model trained using Sentinel-6A Sigma0 and SWH while the lower panel shows the SDD map for the official Sentinel-6A data. Although the same spatial distribution features can be seen in both maps, the intensity of the yellow-orange-red is higher, i.e. larger SDD values, in the lower panel (official product). At the same time, the shades of blue are stronger in the ANN map (upper panel) which indicates lower SDD values.

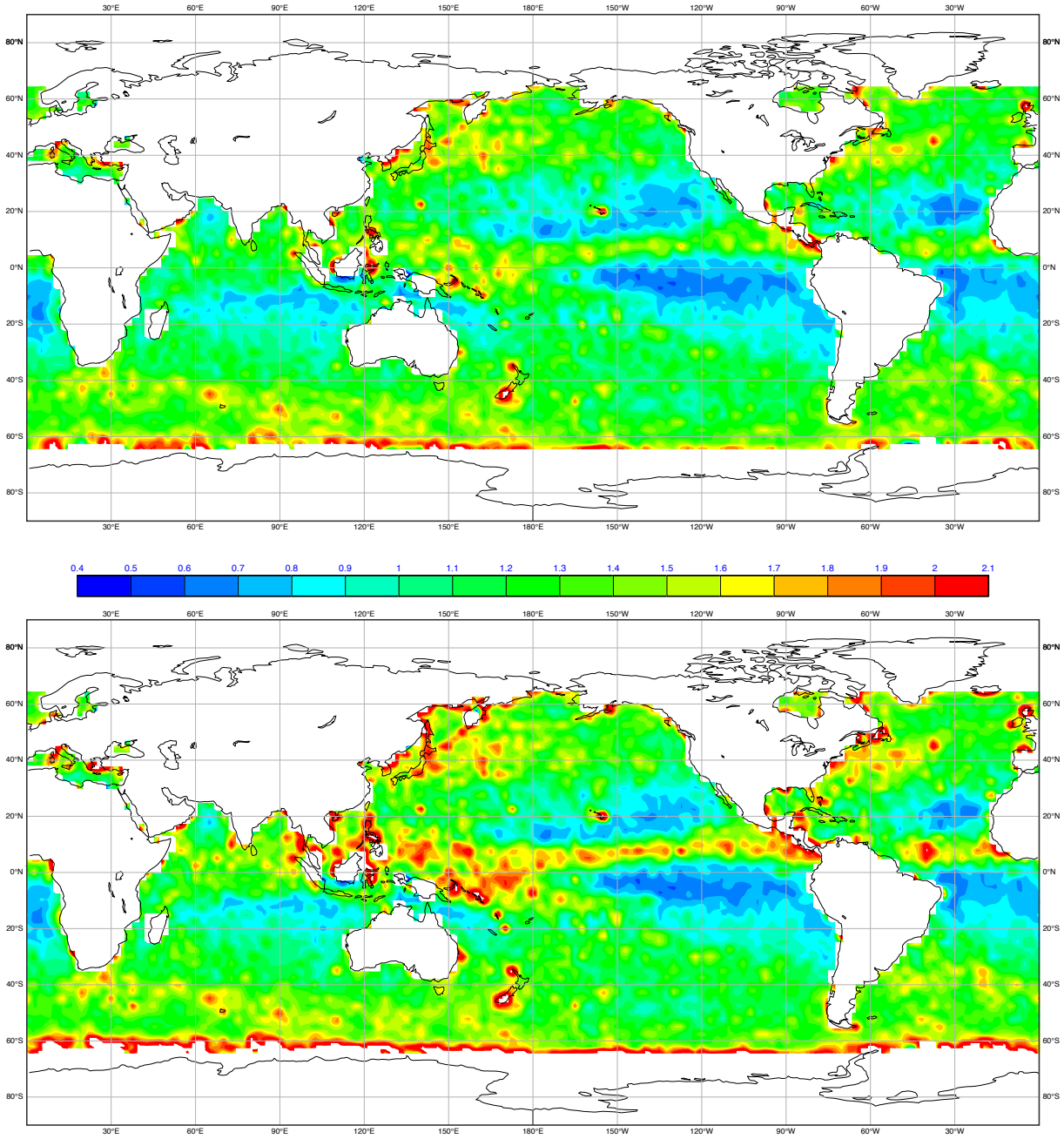

Figure 41: Standard deviation of the difference (SDD), in m/s, of official Sentinel-6A altimeter wind speed compared to IFS model during the period from 17 June to 11 December 2023. The upper panel is from filtered data while the lower panel is from the unfiltered data.

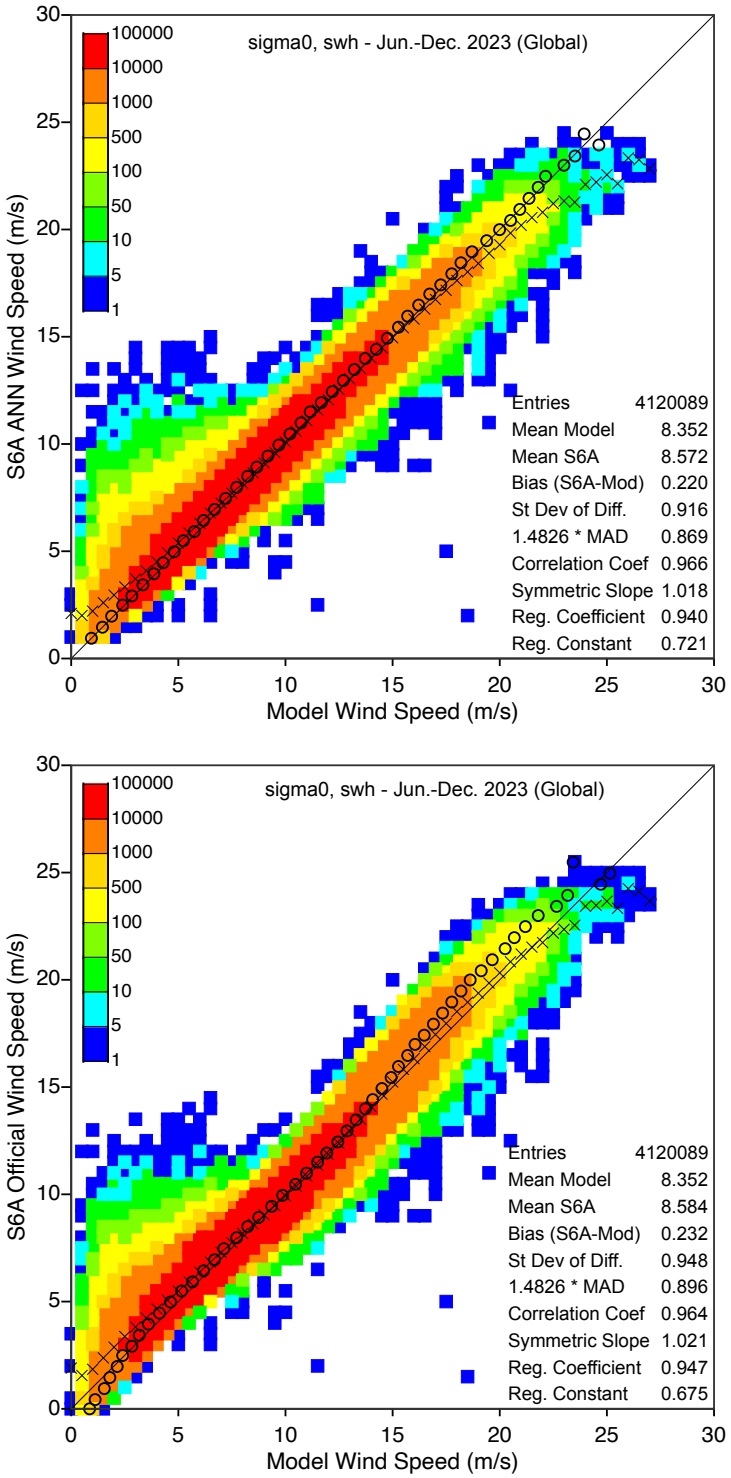

Figure 42: Wind speed comparison between Sentinel-6A altimeter and ECMWF model analysis over the global ocean during the period from 17 June to 11 December 2023. The upper panel is for Sentinel-6A wind from the ANN model with Sigma0 and SWH while the lower panel is for the official Sentinel-6A product (which was derived from Sigma0 and SWH). Only filtered data are used for both plots. ANN model training period is between 17 June 2022 and 17 June 2023. Number of collocations in each 0.5 m/s X 0.5 m/s 2-D bin is coloured-coded as in the colour bar in the legend. The crosses are the means of all bins with given x-axis values (model) while the circles are the means of all bins with given y-axis value (Sentinel-6A).

2.5.2. ANN Model Utilising Sentinel-6A Sigma0 Only

Another ANN model was trained using only Sentinel-6A Sigma0. Other details are the same as described earlier. Figure 44 shows the wind speed comparison between Sentinel-6A altimeter as computed using the Sigma0 only ANN model and ECMWF model analysis over the whole global ocean during the period from 17 June to 11 December 2023 (independent validation period). Only filtered data were used. Comparing Figure 44 to the upper panel of Figure 42 (the ANN model trained using Sentinel-6A Sigma0 and SWH), one can recognise a slight degradation as expected. SDD, scaled MAD and correlation coefficient changed from 0.916 m/s, 0.869 m/s and 0.966, respectively, in the case of Sigma0-SWH ANN model to 0.953 m/s, 0.873 m/s and 0.964, respectively, in the case of Sigma only ANN model. The latter set of values are very close to the corresponding values that emerge from the official Sentinel-6A wind product (0.948 m/s, 0.896 m/s and 0.964, respectively) as can be seen in the lower panel of Figure 42.

The map of the SDD between the ANN model that utilises Sentinel-6A Sigma0 only and the ECWMF model winds is shown in Figure 45. Comparing this map to that in the upper panel of Figure 43 which correspond to wind SDD for the ANN model trained using Sentinel-6A Sigma0 and SWH, one can notice that the same spatial distribution features are seen in both maps. However, the intensity of the yellow-orange-red is higher, i.e. larger SDD values, in Figure 45 (Sigma0 only model), which is expected given the better performance of the model utilising the additional SWH variable (upper panel of Figure 43). The surprise is that the blueish colours in the Sigma0 only SDD map (Figure 45) tend to be larger and more intense than those in the Sigma0-SWH map (Figure 43). The differences, however, are not large.

Maps of the Sentinel-6A wind bias defined as the mean difference between Sentinel-6A wind and the ECMWF model wind are shown in Figure 46. The upper panel of Figure 46 shows the wind bias of the ANN model trained using Sentinel-6A Sigma0 only while the lower panel shows the bias in the case of the ANN model trained using Sigma0-SWH pair. Both bias plots show overwhelmingly positive biases. The Sigma0 only model bias (upper panel) tends to have large areas with negative wind biases in the Northern Hemisphere but very little negative biases in the extra-tropical Southern Hemisphere. On the other hand, the Sigma0-SWH model (lower panel) shows fewer negative areas, but they tend to be balanced between the Northern and Southern Hemispheres. This feature is possible due to the impact of swell on the altimeter wind retrieval.

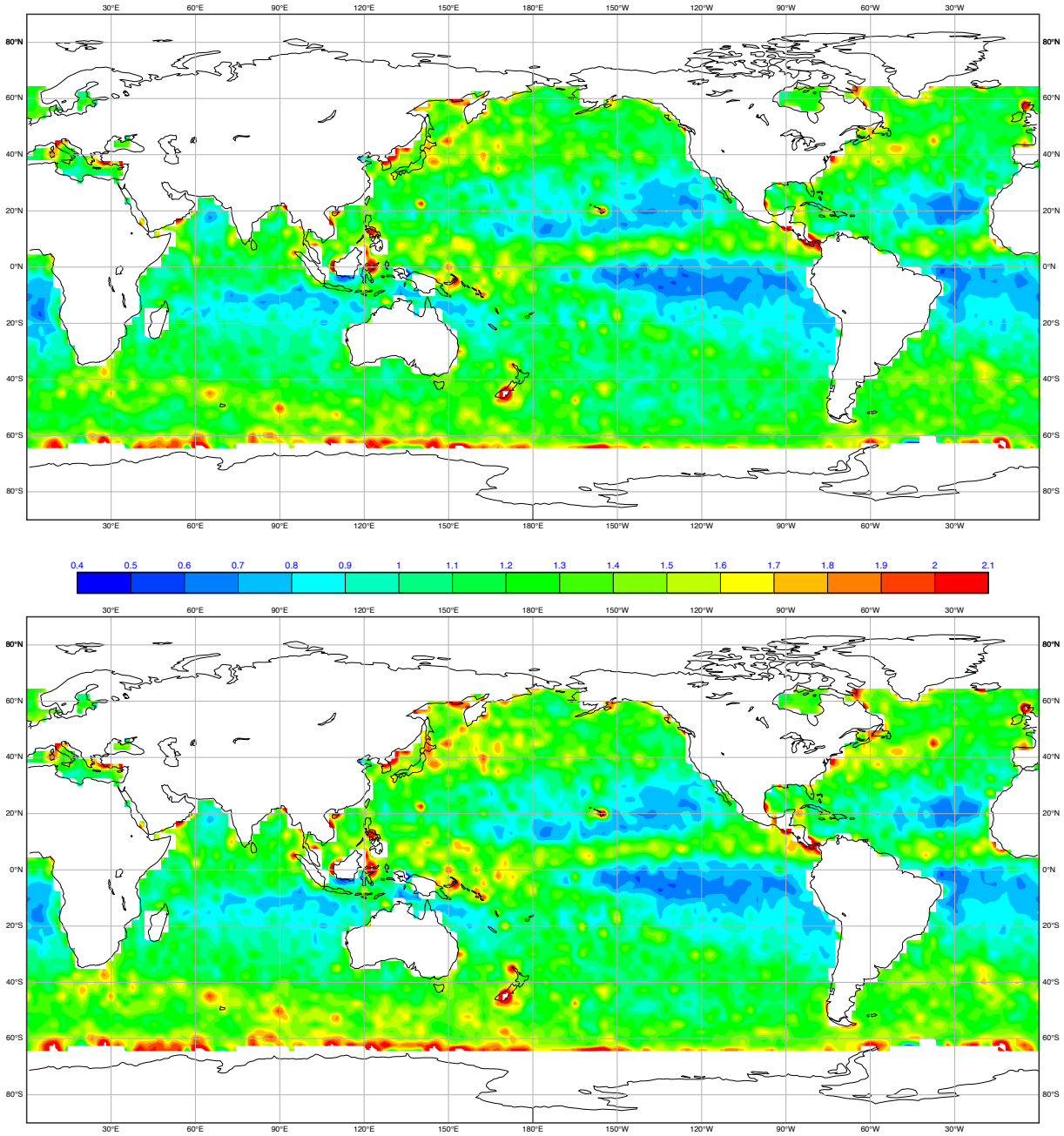

Figure 43: SDD of filtered Sentinel-6A altimeter wind speed, in m/s, compared to ECMWF model during the period from 17 June to 11 December 2023. The upper panel is from Sigma0 and SWH ANN model while the lower panel is from the official Sentinel-6A product.

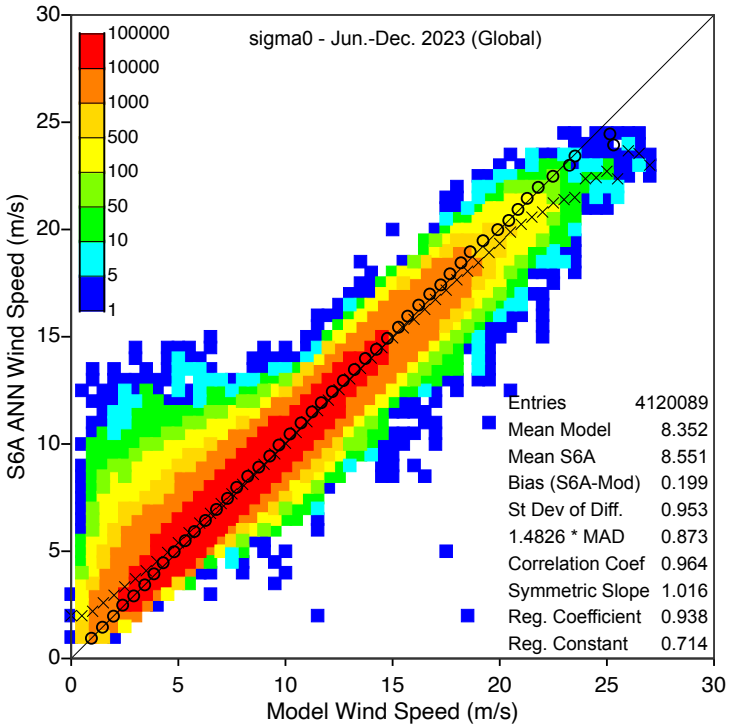

Figure 44: Wind speed comparison between ANN model that uses Sigma0 only from Sentinel-6A altimeter and ECMWF model analysis over the global ocean during the period from 17 June to 11 December 2023. Only filtered data are used. ANN model training period is between 17 June 2022 and 17 June 2023. See caption of Figure 42 for colour-coding, crosses and circles.

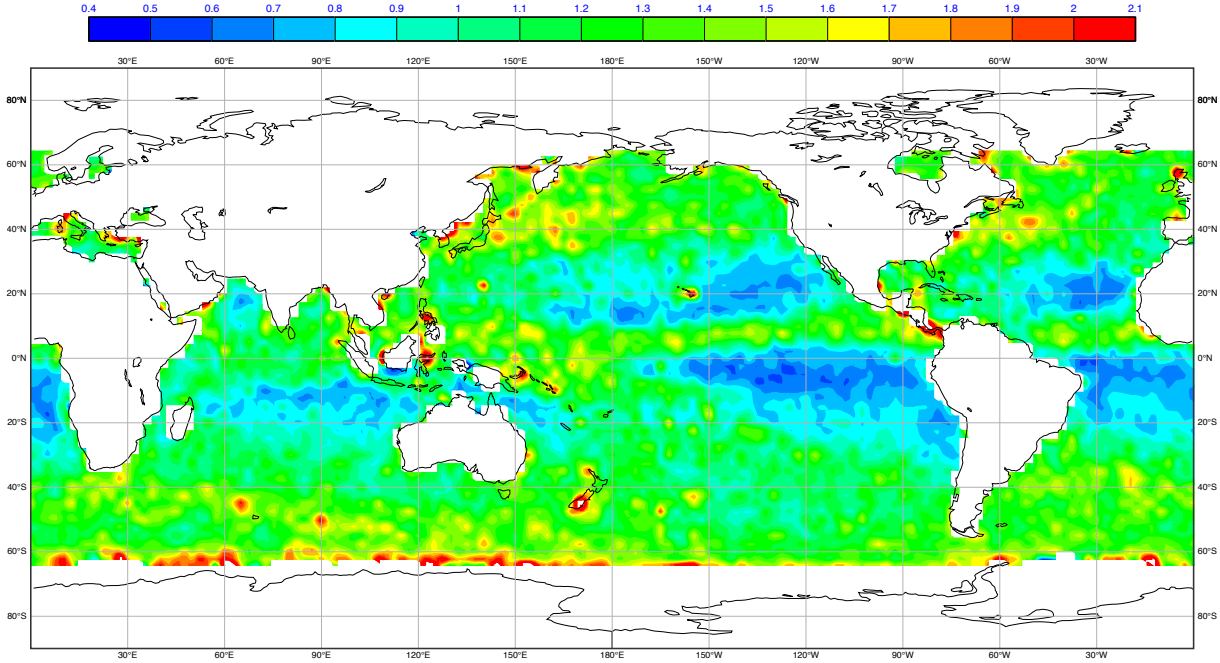

Figure 45: SDD of filtered Sentinel-6A altimeter wind speed, in m/s, computed using the Sigma0 only ANN model compared to ECMWF model during the period from 17 June to 11 December 2023.

2.5.3. ANN Model Utilising Sentinel-6A Sigma0, SWH and Altimeter Mis-pointing

Minor deviation of altimeters from nadir is usually tolerable for altimeter measurements. However, that might come at a price of slight degradation. Another model was trained that utilises, in addition to Sigma0 and SWH, the altimeter mis-pointing expressed in terms of the squared of off-nadir angle derived from the trailing edge of the altimeter waveform (will be referred to as Offnadir).

Figure 47 shows the wind speed comparison between Sentinel-6A altimeter as computed using the Sigma0-SWH-Offnadir ANN model and ECMWF model analysis over the whole global ocean during the period from 17 June to 11 December 2023 (independent validation period). Only filtered data were used. Comparing Figure 47 to the upper panel of Figure 42 (the ANN model trained using Sentinel-6A Sigma0 and SWH), one can recognise quite an improvement. SDD, scaled MAD and correlation coefficient changed from 0.916 m/s, 0.869 m/s and 0.966, respectively, in the case of Sigma0-SWH ANN model (upper panel of Figure 42) to 0.861 m/s, 0.796 m/s and 0.970, respectively, in the case of Sigma-SWH-Offnadir ANN model (Figure 47). Including the off-nadir angle introduced few (10's of) very low wind cases in more agreement with the model.

The map of the SDD between the ANN model that utilises Sentinel-6A Sigma0, SWH and Offnadir and the ECWMF model winds is shown in Figure 48. Comparing this map to that in the upper panel of Figure 43 which correspond to wind SDD for the ANN model trained using Sentinel-6A Sigma0 and SWH, one can notice that the same spatial distribution features are seen in both maps. However, the areas with low SDD values (shades of blue) are getting larger and darker when the off-nadir angle was introduced (Figure 43). The size and intensity of the yellow-orange-red (high SDD values) are getting smaller due to the inclusion of the off-nadir angle.

Maps of the wind speed bias, with respect to the ECMWF model wind, of the ANN model that utilises Sentinel-6A Sigma0, SWH and Offnadir is shown in Figure 49. Comparing this map to that from the lower panel of Figure 46, which shows the wind bias of the ANN model trained using Sentinel-6A Sigma0 and SWH pair, one can notice that the overall bias has been decreased with more white areas, indication bias close to zero.

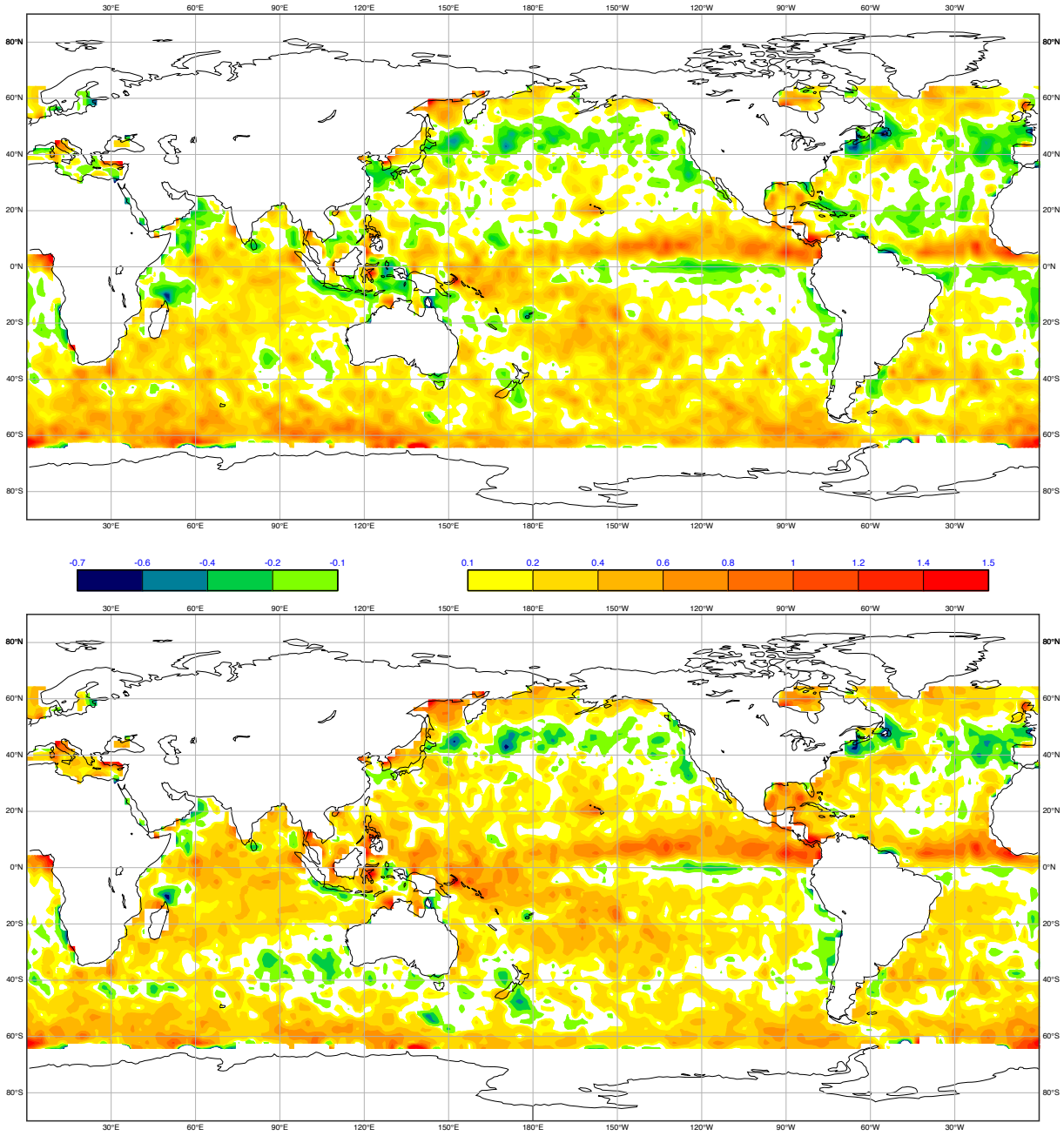

Figure 46: Bias of filtered Sentinel-6A altimeter wind speed, in m/s, compared to IFS model during the period from 17 June to 11 December 2023. The upper panel is from Sigma0 only ANN model while the lower panel is from Sigma0-SWH ANN model.

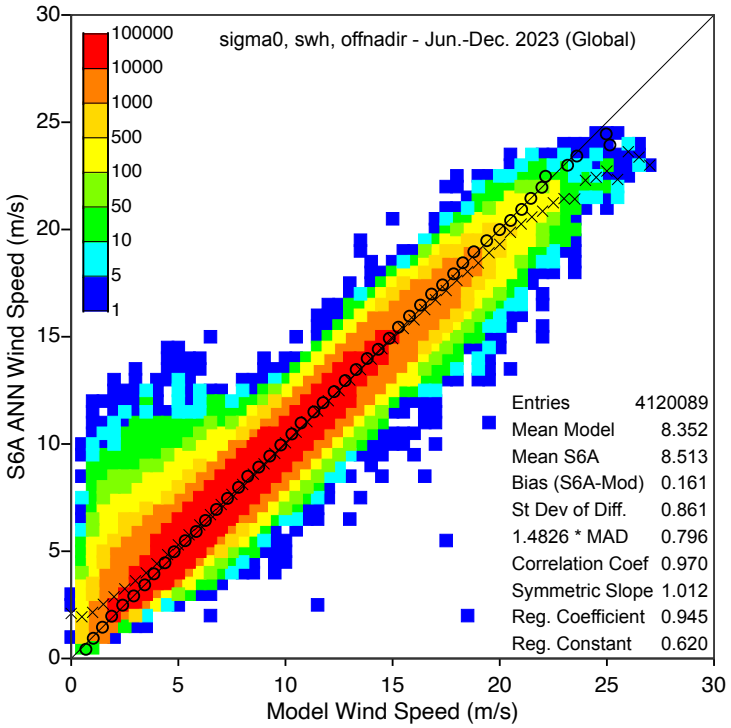

Figure 47: Same as Figure 44 but with the ANN model utilising Sigma0, SWH and off-nadir angle from Sentinel-6A altimeter.

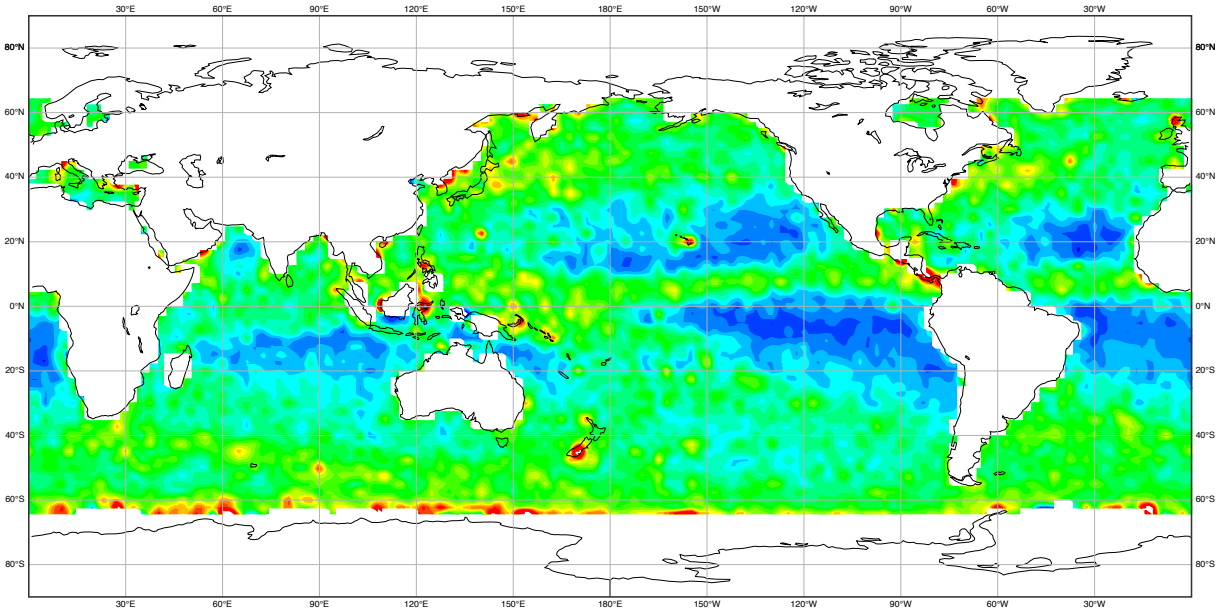

Figure 48: SDD of filtered Sentinel-6A altimeter wind speed, in m/s, computed using the Sigma0, SWH and off-nadir angle ANN model compared to ECMWF model during the period from 17 June to 11 December 2023.

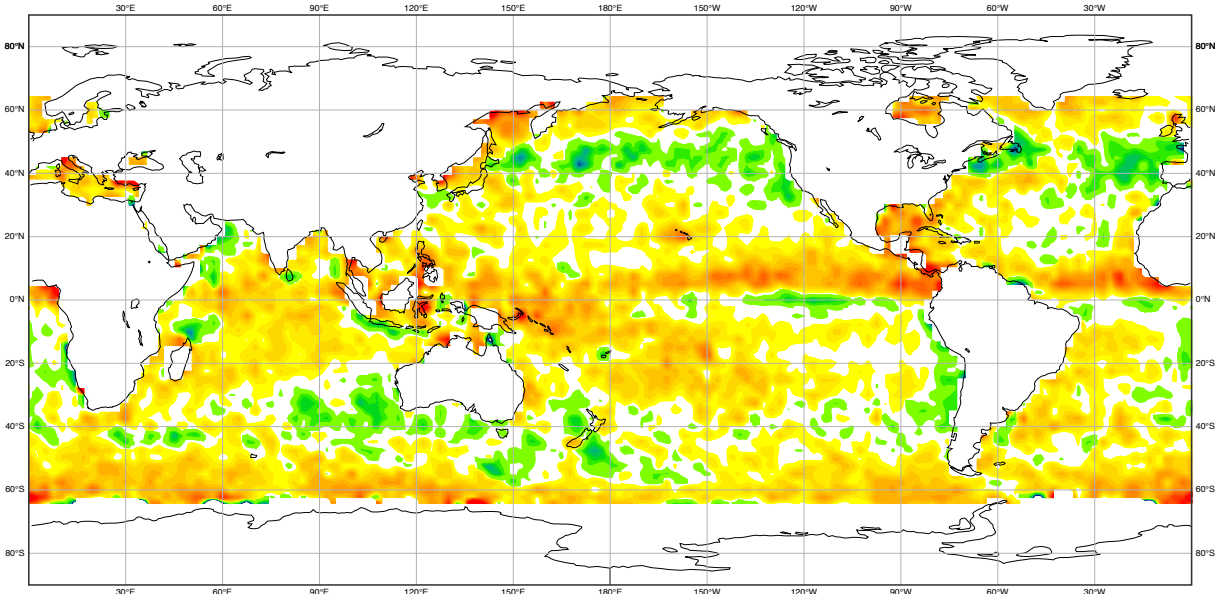

Figure 49: Bias of filtered Sentinel-6A altimeter wind speed, in m/s, computed using the Sigma0, SWH and off-nadir angle ANN model compared to ECMWF model during the period from 17 June to 11 December 2023.

2.6. Discussion

2.6.1. Positive Impact of Including Altimeter Mis-pointing

The importance of including the altimeter mis-pointing expressed in terms of the squared of off-nadir angle derived from the trailing edge of the altimeter waveform (off-nadir angle) to Sigma0 and SWH in the ANN model was demonstrated in Section 2.5.3. To further test the impact of including the off-nadir angle, an ANN model trained using only Sigma0 and the off-nadir angle (i.e. SWH is not included). The comparison of the results of this model against the ECMWF model wind is shown in Figure 50 for the whole global ocean during the period from 17 June to 11 December 2023 (independent validation period). Only filtered data were used. Comparing Figure 50 (Sigma0 and Offnadir without SWH) to Figure 47 (Sigma0, SWH and Offnadir), it is clear that there is a degradation for not including SWH. On the other hand, comparing Figure 50 (Sigma0 and Offnadir) to the upper panel of Figure 42 (Sigma0 and SWH), one can notice that utilising Sigma0 and the off-nadir angle produces better results than utilising Sigma0 and SWH. A possible explanation is that the off-nadir angle reflects the mis-pointing of the altimeter as well as the existence of the long swell (or other long ocean waves) which causes a tilt of the water surface.

Including the off-nadir angle also introduces few (10's of) very low wind cases in more agreement with the model.

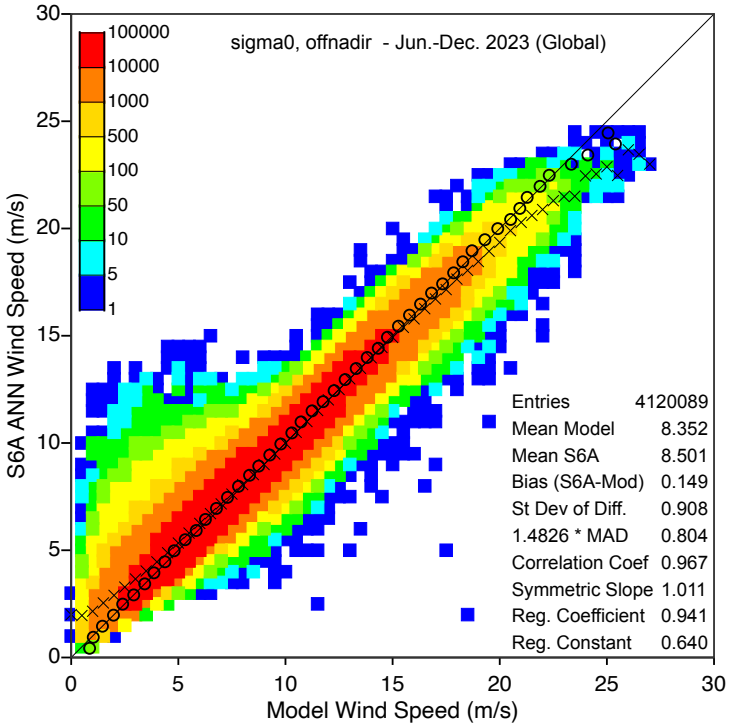

Figure 50: Same as Figure 44 but with the ANN model utilising Sigma0 and off-nadir angle from Sentinel-6A altimeter.

2.6.2. Impact of Including C-Band Sigma0

The intensity of backscatter depends on the wavelength of the radar signal. In a sense, Ku-band (~2 cm wavelength) and C-band (~ 5 cm) altimeters do not see the same details of the sea-surface roughness. Training an ANN model that utilises the backscatter from both bands (Sigma0 and Csigma0) was tried.

The comparison of the results of the ANN model that utilises backscatter from both bands against the ECMWF model wind is shown in Figure 51 for the whole global ocean during the period from 17 June to 11 December 2023 (independent validation period). Only filtered data were used. Comparing Figure 51 (Sigma0 and Csigma0) to the upper panel of Figure 42 (Sigma0 and SWH), one can notice that the former model (utilising both backscatters) produces comparable results to those produced by utilising Sigma0 and SWH. Including the C-band backscatter introduces few (10's of) very low wind cases in more agreement with the model.

Including SWH to both (Ku- and C-band) backscatter values, improves the agreement with the ECMWF model winds as can be seen in Figure 52.

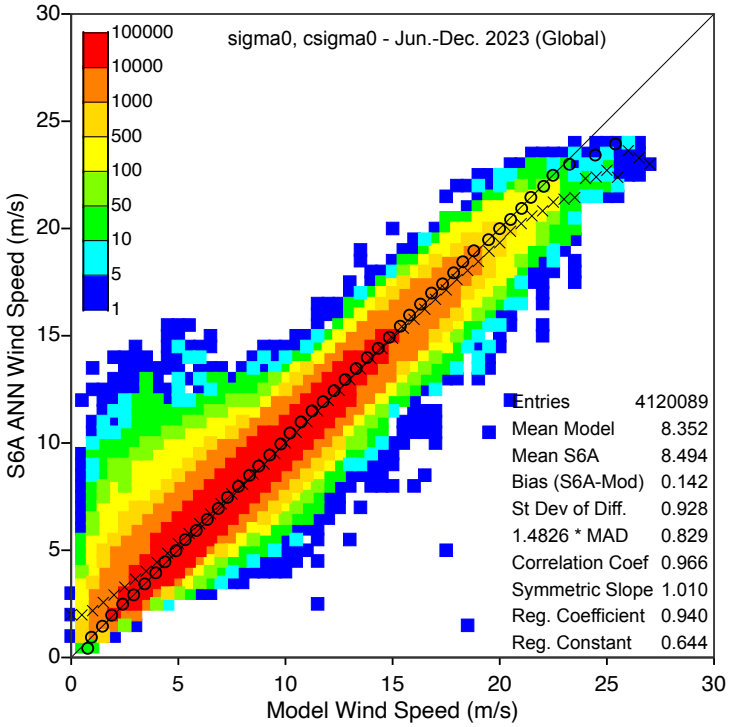

Figure 51: Same as Figure 44 but with the ANN model utilising both Ku-band and C-band Sigma0 values from Sentinel-6A altimeter.

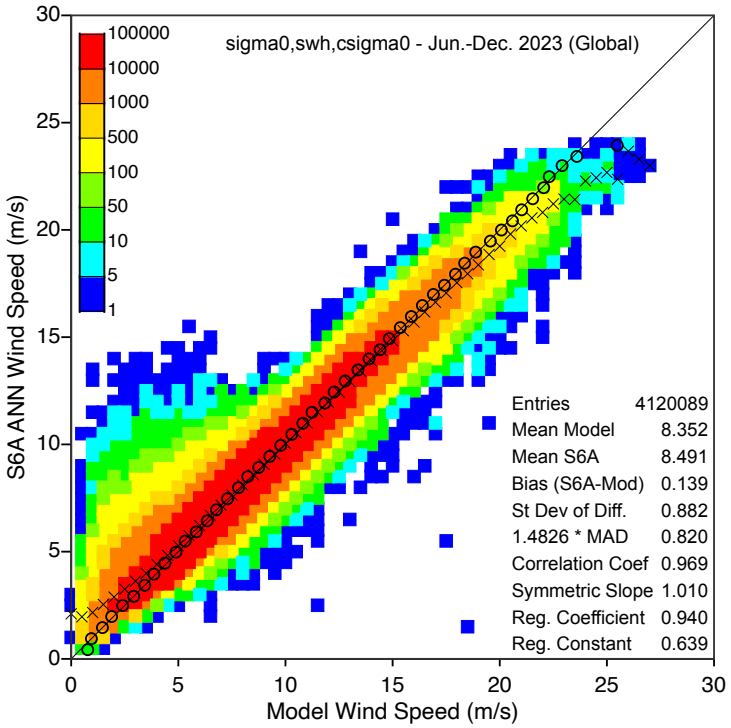

Figure 52: Same as Figure 44 but with the ANN model utilising SWH in addition to both Ku-band and C-band Sigma0 values from Sentinel-6A altimeter.

2.6.3. *Impact of Including 10 Altimeter Variables*

The impact of including many variables that are measured by Sentinel-6A altimeter was also tested. The following altimeter measurements were included:

- Ku-band
  - backscatter, *sigma0*;
  - significant wave height (SWH), *swh*;
  - standard deviation (SD) of SWH, *swhsd*;
  - SD of sigma0, *sigma0sd*;
  - SD of range, *rangesd*;
- C-band
  - backscatter, *csigma0*;
  - SD of SWH, c*swhsd*;
  - SD of sigma0, *csigma0sd*;
  - SD of range, c*rangesd*;
- Mis-pointing of altimeter from nadir as derived from the trailing edge of the Ku-band waveform, also known as offnadir angle, *offnadir*.

The comparison of this model against ECMWF model wind is shown in Figure 53 for the whole global ocean during the period from 17 June to 11 December 2023 (independent validation period). Only filtered data were used. The agreement with ECMWF model wind is the best with low bias (0.148 m/s), SDD (0.852 m/s), and scaled MAD (0.793 m/s) and high correlation coefficient (0.971). However, the improvement compared to the case of Sigma0-SWH-Offnadir ANN model is marginal.

2.6.4. *Impact of Various Combinations of Altimeter Variables*

Several combinations of the altimeter variables mentioned earlier were used for training. The results from each case were compared against the ECMWF model winds over the whole global ocean during the period from 17 June to 11 December 2023 (independent validation period). Only filtered data were used. The correlation coefficients from each ANN model are displayed in the bar chart shown in Figure 54. The standard deviation of the difference (SDD) and the reduction in SDD are shown in Figure 55and Figure 56, respectively. Ku-band backscatter (sigma0) is the basic variable and retained in all ANN models. Including significant wave height (swh), the C-band backscatter (csigma0) and the mis-pointing (offnadir) separately or together, introduces a positive jump in statistics. The combination of Ku-band sigma0, SWH and C-band sigma0 introduced a significant positive impact. Slightly better positive impact comes from using the combination of Ku-band sigma0, SWH and off-nadir angle. Including SWH from both bands does not introduce any benefit. Using all possible variables, produces the best results.

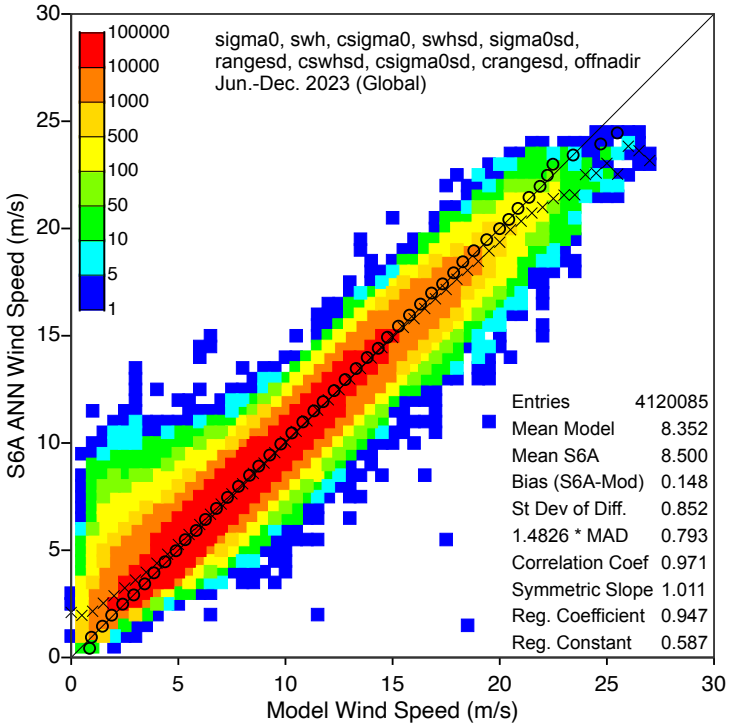

Figure 53: Same as Figure 44 but with the ANN model utilising SWH in addition to both Ku-band and C-band Sigma0 values from Sentinel-6A altimeter.

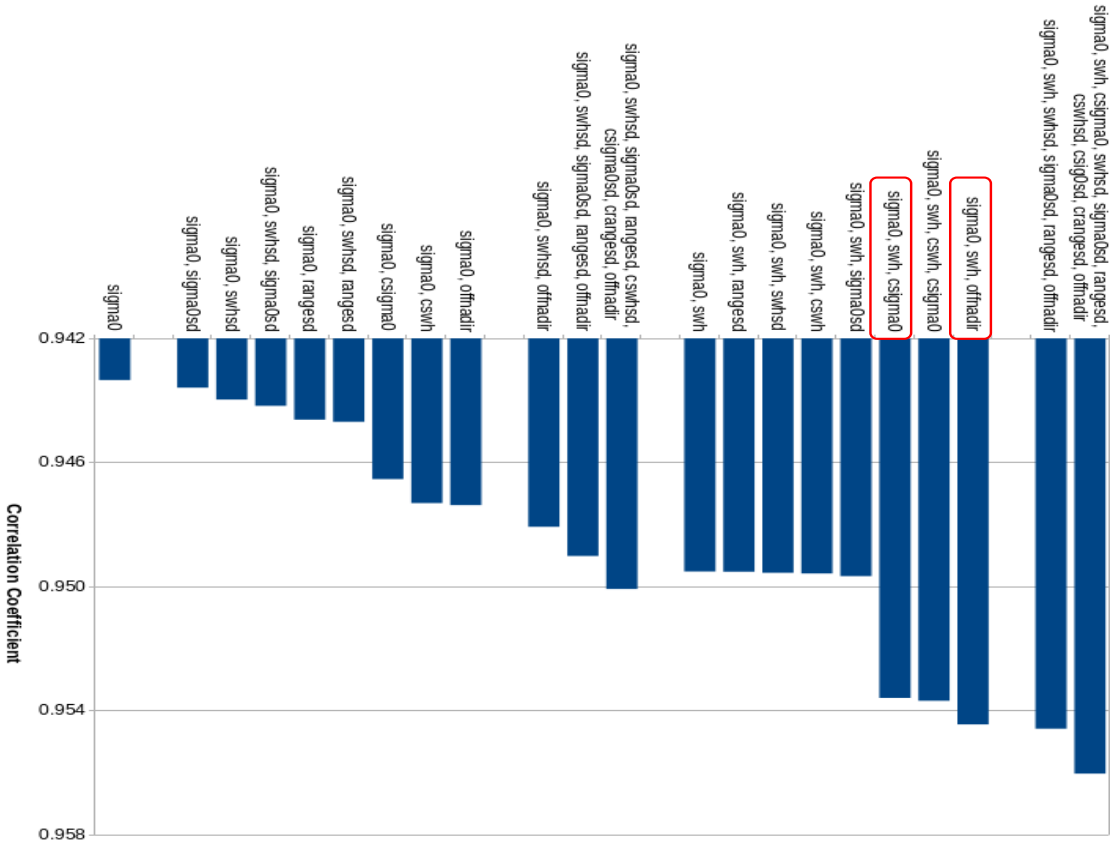

Figure 54: The correlation coefficients of the ANN models utilising different combinations of Sentinel-6A altimeter measurements for filtered Sentinel-6A altimeter data over the whole global ocean during the period from 17 June to 11 December 2023.

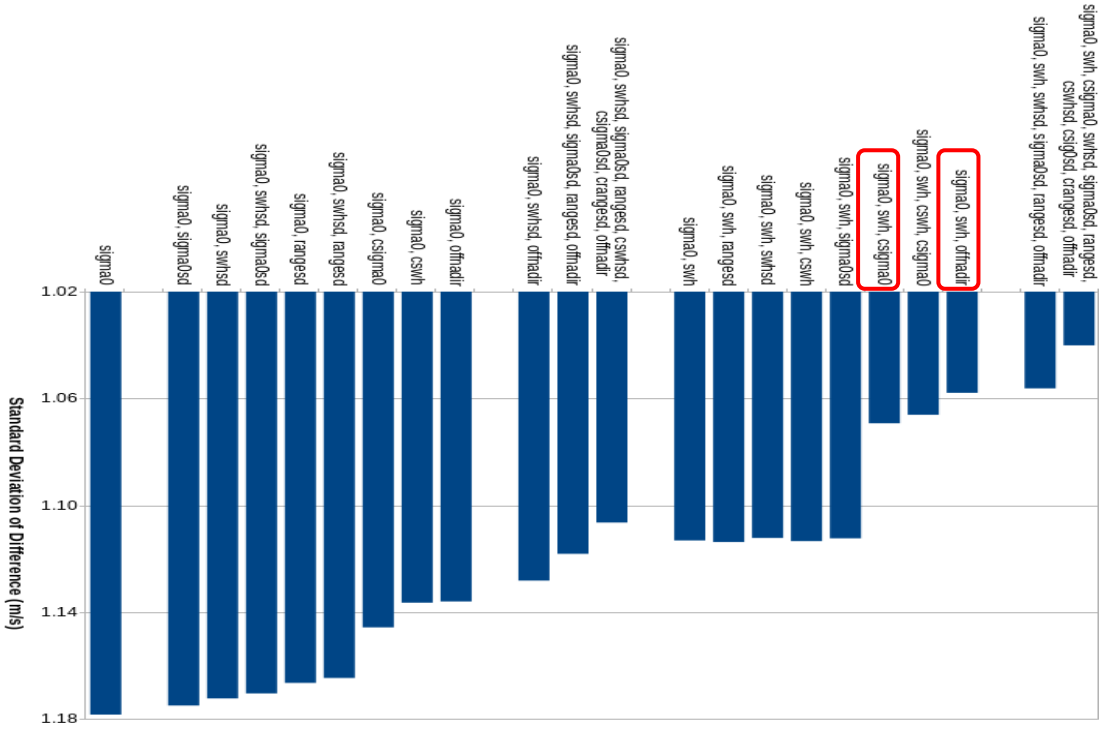

Figure 55: Same as Figure 54 but for the standard deviation of the difference (SDD).

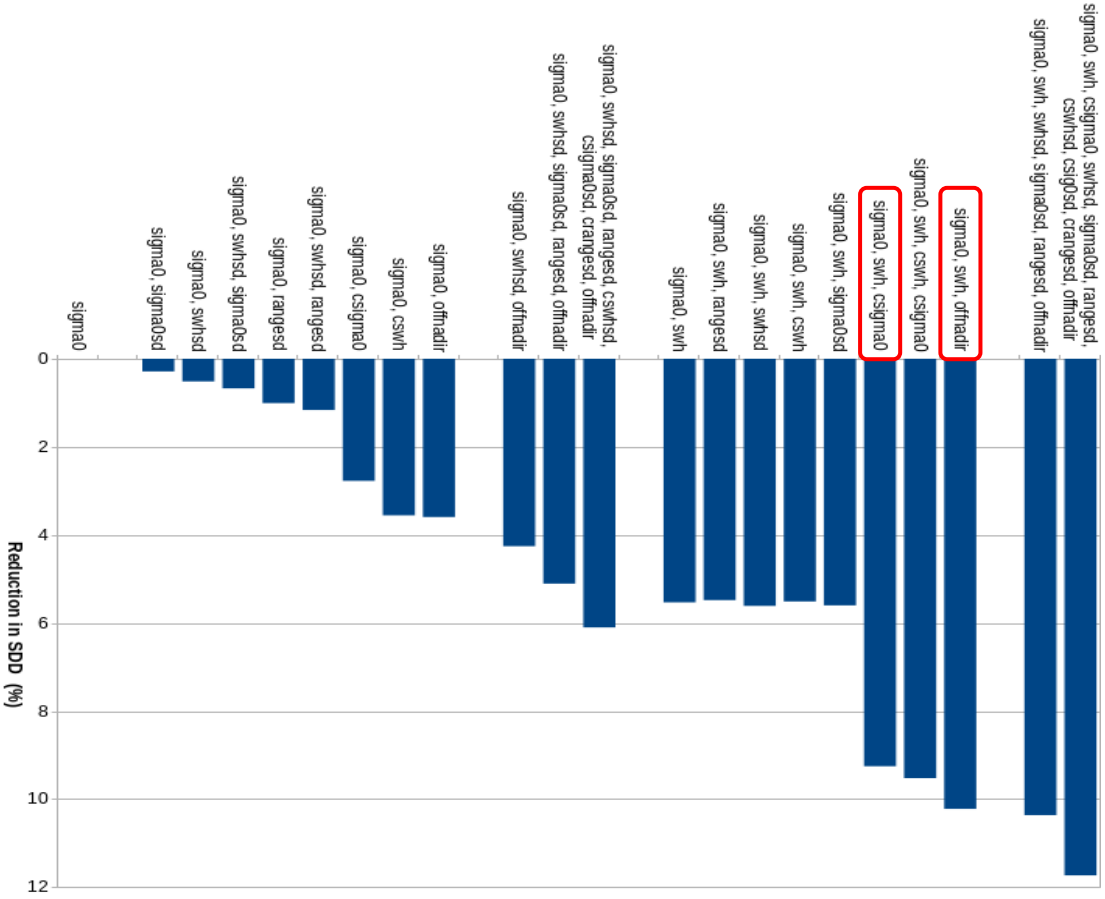

Figure 56: Same as Figure 54 but for the reduction of SDD in percent compared to the model that utilises Ku-band Sigma0 only.

2.7. Summary and Conclusions

As stated in Section 1.6, artificial neural networks (ANN) is an attractive tool that can be used to develop numerical models based on the data without the need for a deep understanding of the detailed physical laws nor the functional dependence. Its flexibility to include extra features (input variables) with minimal effort is another strength. This has been proved for the altimeter wind retrieval as well.

Data cleaning is very essential for the success of ANN. A procedure to clean altimeter data was proposed. Although there was effort to optimise the procedure, its results are very satisfactory.

The 1-Hz Sentinel-6A conventional Low-Resolution Mode (LRM) altimetry measurements, including the backscatter (Sigma0), significant wave height (SWH) and the standard deviation of the their and the range 20-Hz (within each 1 Hz) from both altimeter channels (Ku- and C-bands) and the altimeter square of off-nadir angle over a period of about 18 months (17 June 2022 to 11 December 2023) were collocated with the ECMWF model 10-m wind analysis. The first year of collocations were used for ANN model training. The remaining 6 month of collocations were used for the independent validation of the models.

Several ANN models were trained. Additional Combinations of Sentinel-6A altimeter measurements were utilised for model training with Ku-band backscatter maintained in all combinations. The inclusion of variables like SWH and off-nadir angle improves the skill of the trained ANN models. The inclusion of backscatter from both channels (Ku- and C-bands) shows improvements as well.

Utilisation of Ku-band backscatter and SWH together with the square of off-nadir angle is recommended for use in altimeter wind retrievals. The combination of backscatter from both channels (Ku- and C-bands) and Ku-band SWH is the second-best combination.

3. Development of the Tangent Linear and the Adjoint Models (WP 3)

3.1. Introduction

Neglecting model error, and absorbing the model integration and interpolation to the observation time and location into the observation operator, H, the 4D-Var cost function, J, can be written as,

$$J(\mathbf{x}) = \frac{1}{2}(\mathbf{x}-\mathbf{x_b})^T\mathbf{B^{-1}}(\mathbf{x}-\mathbf{x_b}) + \frac{1}{2}(\mathbf{y}-H(\mathrm{x}))^{\mathbf{T}}\mathbf{R^{-1}}(\mathbf{y}-H(\mathbf{x}))$$

where $\mathbf{x}$ is the estimate of the atmospheric state, $\mathbf{x_b}$ is a short-range forecast valid at the start of the assimilation window, $\mathbf{y}$ is the vector of observations and ($\mathbf{B}$ and $\mathbf{R}$) are the short-range forecast error and observation error covariance matrices, respectively. In order to minimise the 4D-Var cost function, we also need both the tangent-linear and adjoint of the observation operator H, which can be denoted as $\mathbf{H}$ and $\mathbf{H^T}$, respectively. The tangent-linear represents the derivative of the observed values with respect to the state vector elements. For example, in this work it computes the derivative of simulated sigma0 values with respect to the 10 m neutral equivalent winds. The adjoint, $\mathbf{H^T}$, arises because we need to compute the derivative of the cost function with respect to the state vector, $\mathbf{x}$,

$$J'(\mathbf{x}) = \mathbf{B^{-1}}(\mathbf{x}-\mathbf{x_b}) - \mathbf{H^T R^{-1}}(\mathbf{y}-H(\mathbf{x}))$$

during the 4D-Var minimisation, noting the use of $\mathbf{H^T}$matrix multiplied by a vector, $\mathbf{R^{-1}}(\mathbf{y}-H(\mathbf{x}))$. The tangent-linear code is also needed during the minimisation because ECMWF uses the incremental formulation of 4D-Var ([6]).

3.2. Implementation

The tangent-linear is usually computed first by manually differentiating each line of the observation operator code, H. This tangent-linear code is then transposed manually line-by-line, to form the adjoint version of the code. Although the rules for adjoint coding are relatively straightforward given sufficient experience, the resulting code is often not intuitive and it can be extremely difficult to debug.

The use of an ANN approach can simplify the forward modelling and the subsequent tangent-linear and adjoint coding steps considerably. This is because the same general structure of an ANN can be applied to a diverse set of problems. Fundamentally, the ANN is defined by the chosen architecture, the weight matrices, $\mathbf{W_i}$, and the bias vectors, $\mathbf{b_i}$. Recently, [23] demonstrated the flexibility of ANNs in the context of data assimilation by showing how forward models, tangent-linear and adjoint models can be built with ANN to emulate a gravity wave drag scheme. As part of that work, they also produced useful FORTRAN90 code that was effectively a translation of an ANN python code produced with Keras/TensorFlow to the F90 code required in the ECMWF 4D-Var. We deliberately selected the same hyperbolic tan (*tanh*) activation function as used by [23] when constructing the sigma0 forward operator. This meant we were able to reuse much of their gravity wave Fortran90 code by simply selecting the appropriate weight matrices ($\mathbf{W_i}$) and bias vectors ($\mathbf{b_i}$) estimated during the training of the

sigma0 ANN (Section 1). This simplified the work on the sigma0 tangent-linear and adjoint considerably.

The implementation of the ANN based assimilation code was tested in a series of short technical experiments designed to demonstrate that the 4D-Var system converged correctly when the new scatterometer sigma0 data was being assimilated. One example is shown in Figure 57, where the spatial variation of the mean and standard deviation of both the sigma0 (o-b) and (o-a) departure statistics are presented. These statistics are computed over 30 days, between March 1-30, 2022. As expected, there is a clear reduction in both the standard deviation and mean of the departures as a result of assimilating the sigma0 data in the 4D-Var. The globally averaged mean (o-b) value is only 0.02 dB but this masks significant spatial variations. The mean absolute departure is close to 1 dB. The globally averaged mean absolute departure of the (o-a) is reduced to 0.7 dB. The globally averaged standard deviation of the (o-b) departures shown here is 1.6 dB, and the standard deviation of the (o-a) departures is reduced to 1.2 dB. We note that 1.6 dB for the (o-b) statistics is larger than obtained in either the ANN training or validation (Section 1). However, as part of the testing phase we found that this can be reduced to around 1.3 dB by replicating some of the quality control (QC) checks performed in the ASCAT Level 2 wind assimilation system because checks are automatically incorporated in the training and validation datasets. These QC checks include screening based on the following information provided with the observation:

- The land fraction flag
- The sigma0 quality flag
- The "Kp" quality flag

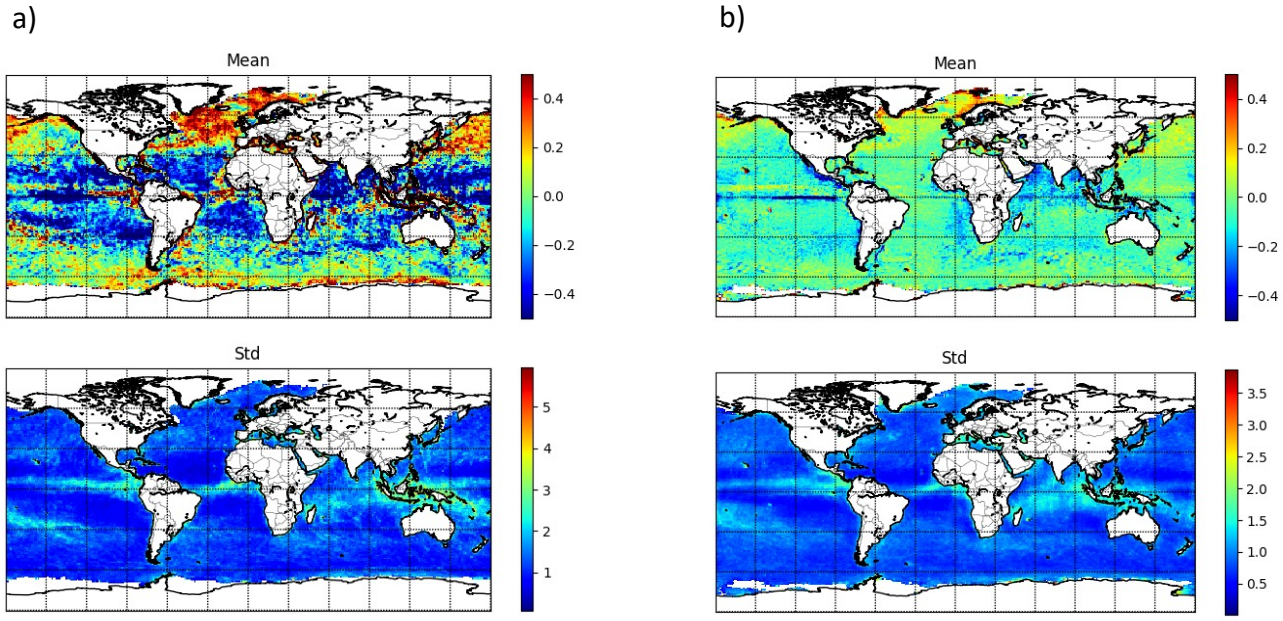

Figure 57: The mean (upper) and standard deviation (lower) of the ASCAT σ^0 departure statistics for a) observation minus background; and b) observation minus analysis. The statistics are computed over 1 month, for March 1-30, 2022.

4. Assimilation Experiments (WP 4)

4.1. Experimental Set-up

The main experiments reported here are run for the period January 1 to April 30, 2022. A second period from April 1 to October 31, 2023 has also been tested, but these results will be reported in the context of tropical cyclone impact in Section 4.7. All experiments use ECMWF's IFS cycle 48R1 which is currently used operationally. We use the 4D-Var assimilation approach with a 12-hour assimilation window, and the forecast model used in the assimilation experiments is run at Tco399 which corresponds to a spatial grid of 29 km. In general, all observation types used operationally for this period are assimilated with the exceptions outlined below.

The key experiments for this period are the following:

- **CTL**: The control experiment, assimilating Metop-B and C ASCAT L2 wind retrieval information produced with CMOD5.n at ECMWF during the assimilation experiments as part of the pre-processing step.
- **No SCATT**: As CTL, but not assimilating the ASCAT level 2 wind retrievals.
- **KNMI-R1**: Assimilating the KNMI "selected" wind retrievals, produced with CMOD7 and their 2D-Var ambiguity removal approach. The "selected" KNMI wind vector is the one closest to the 2D-Var analysis.
- **SIG0**: Assimilating Metop-B and C sigma0 values using the ANN approach, that computes sigma0 as a function of the neutral equivalent 10 m wind vector (plus geometry: angles of incidence and azimuth).

Note that we only assimilate scatterometer wind information from Metop-B and Metop-C satellites in these experiments.

Both the scatterometer wind vectors and sigma0 values are assimilated on a 50 km by 50 km spatial grid, after measurement thinning. The retrieved winds used in the CTL and KNMI-R1 experiments are assigned an uncertainty of 2.25 ms^{-1} for both the zonal and meridional (u,v) components. The KNMI-R1 winds are assimilated as neutral equivalent winds rather than "stress equivalent" winds ([12]). This is not optimal, but the Met Office currently make the same assumption in their NWP system. The ambiguity removal is performed and updated during the 4D-Var trajectory calculations, by selecting the scatterometer wind solution closest to the latest estimate of the atmospheric state. In the KNMI-R1 experiment this step is effectively removed because the selected solution is duplicated in the observation database, meaning that only the KNMI selected option is available for assimilation.

The SIG0 experiment is based on the observation operator which takes the neutral equivalent 10 m wind vector as input (plus geometry). For the observation uncertainty, we use the largest value of either 1.6 dB or 10% of the observed value. Spatial error correlations and error correlations between the beams are neglected (assumed equal to 0). Some sensitivity experiments changing the uncertainty values have been performed, but this appears to be a reasonable approach for these initial experiments. Observation values less than -30 dB are "blocklisted", meaning they are not active in the assimilation experiments.

4.2. Verification of short-range forecasts

A useful method for testing the impact of observations on short-range (up to 12 hours) forecasts is to look at the changes in the observation minus background (o-b) departure statistics. In this section, we provide a summary of the results for a range of surface and upper-air observing systems. For example, Figure 58 shows the percentage change in the standard deviation of the (o-b) departures when compared to the CTL experiment for a set of surface observations, including wave heights, winds, surface pressure and humidity. Values below 100% indicate that the configuration is an improvement relative to the control (CTL) and conversely values above 100% indicate that the short-range forecasts are degraded. These statistics are averaged globally. Perhaps the most striking feature is the improved fit (red line: a reduction of > 2.5%) to the ASCAT wind retrievals when using the KNMI-R1 CMOD7 information rather than the CMOD5.n winds used in the CTL experiment. This indicates that the CMOD7 wind retrievals have lower noise than the CMOD5.n wind retrievals used in the CTL experiment. There is also a small improvement in the SARAL and Jason-3 significant wave height (SWH) statistics when using KNMI wind retrievals. We note that the SWH information provided by wave forecasting system is sensitive to the surface wind information provided by the atmospheric forecasts integrated over time.

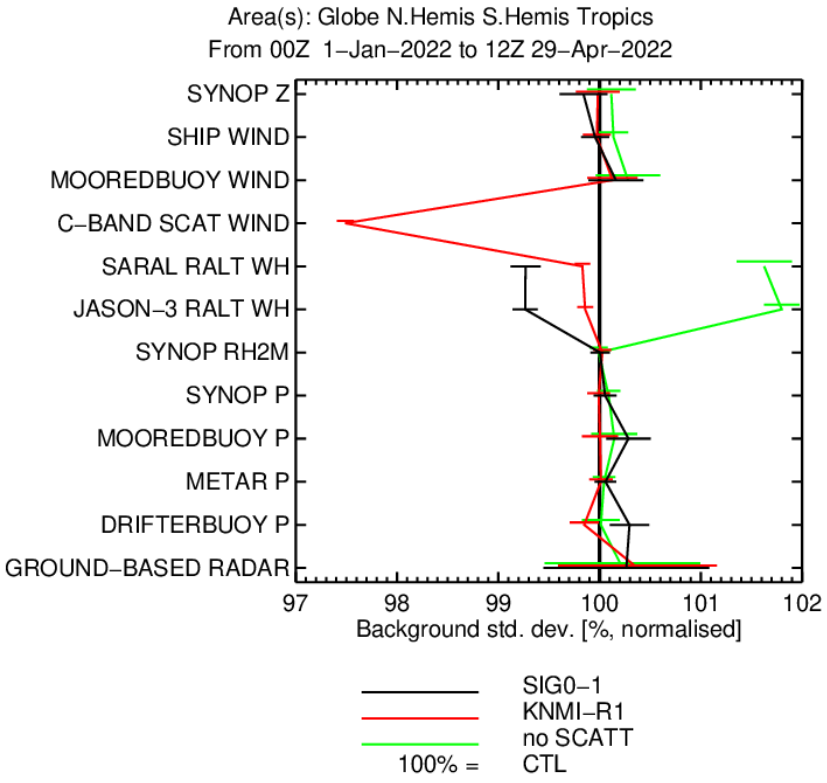

Figure 58: The percentage reduction in the standard deviation of the (o-b) departures for a selection of surface-based observations, when compared with the CTL experiment. Values less than 100% indicate that the departure statistics are improved when compared with CTL. The error bars indicate the 95% confidence interval. These results are globally averaged and cover the period January 1 to April 29, 2022.

There is a clear degradation in the SARAL and Jason-3 SWH departure statistics in the No SCATT experiment (green line), meaning that the scatterometer measurements are improving the forecast fit to these observations. There is also a small degradation in buoy and ship winds, but this is not statistically significant over this period. The use of sigma0 (black line) produces a 0.7% improvement in the SWH statistics relative to the CTL and, consequently, a larger improvement relative to No SCATT. The SWH improvements in the SIG0 experiment are largest in the tropics, where there is a 2% reduction in the (o-b) standard deviation relative to CTL. These SWH results are the clearest example of sigma0 assimilation being potentially better than assimilating wind retrieval information in the short-range departure statistics, but this picture is not uniform across all observation types. For example, the drifting buoy statistics shown in Figure 58 are slightly degraded for SIG0. In addition, Figure 59 shows the departure statistics for the SATOB wind retrievals. The assimilation of sigma0 degrades the departures at 850 hPa and 1000 hPa. Similarly, it appears that scatterometer measurements in the CTL experiment are also degrading the fit to SATOB wind information at these levels (green line: the departures are improved at 850 hPa and 1000 hPa when the scatterometer data is removed). The apparent inconsistency of the scatterometer and SATOB wind information in the ECMWF system has been an issue for some time. In contrast, the KNMI winds produce an improvement below 700 hPa compared to the CTL, but are similar to no SCATT at 850 hPa and 1000 hPa.

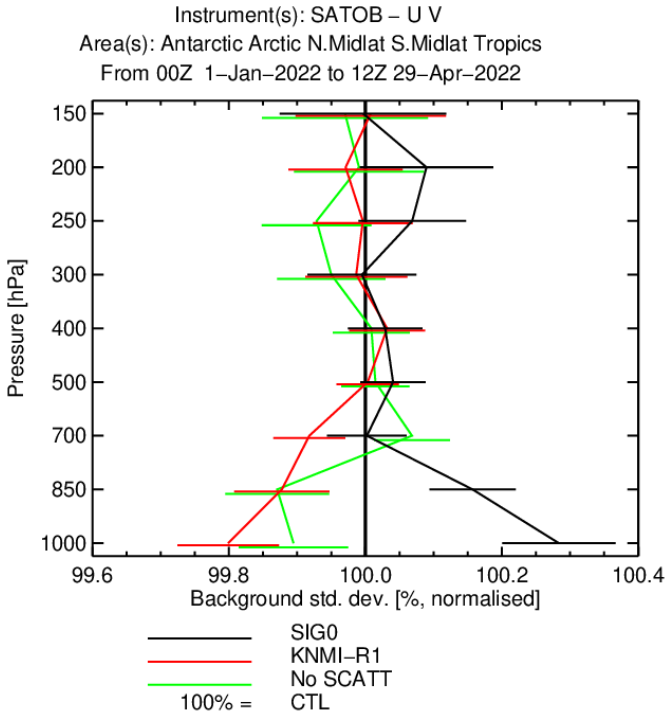

Figure 59: Globally averaged SATOB wind (o-b) departure statistics over the period from January 1 to April 29, 2022, where CTL is 100%.

We do not see much impact on the radiosonde and aircraft wind departure statistics, but Figure 60 shows the globally averaged Aeolus Mie wind departure statistics, where there is a clear degradation below 700 hPa when the scatterometer data is removed, compared to the other experiments. The SIG0 is slightly degraded relative to the CTL, and the KNMI winds are slightly improved, but the statistical significance in both cases is borderline. The impact on Aeolus Rayleigh clear wind departures is neutral.

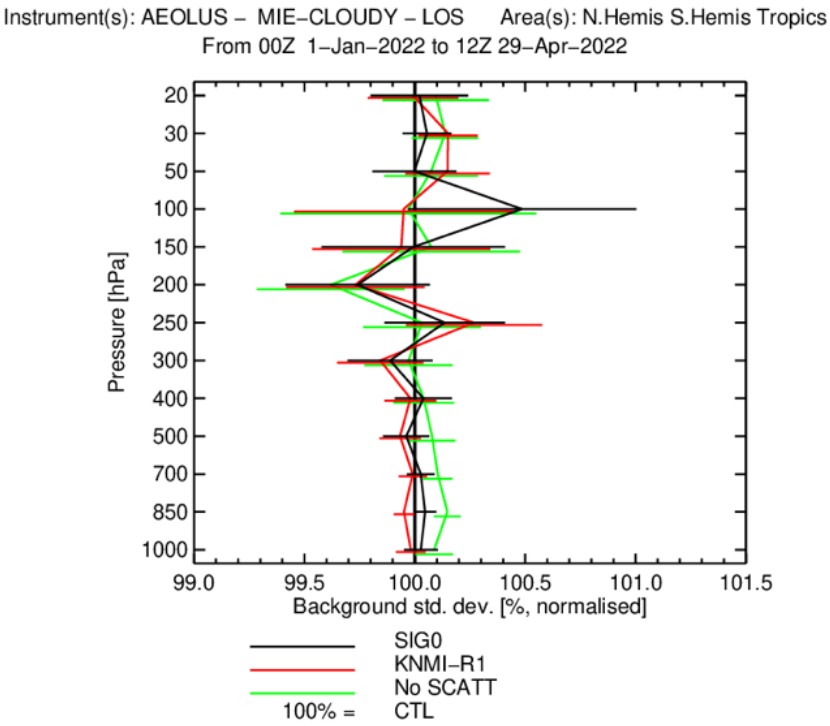

Figure 60: Globally averaged Aeolus Mie wind (o-b) departure statistics over the period from January 1 to April 29, 2022, where CTL is 100%.

Radiances can provide wind information through the 4D-Var tracer effect (e.g. [32]), whereby the wind field is adjusted within the 4D-Var assimilation window, in order to move humidity features and fit the observed radiances more closely. Conversely wind information can improve radiance departure statistics by improving the locations of humidity features within the 4D-Var window. For example, we see significant degradations in the departure statistics for all microwave imagers when scatterometers are removed, as illustrated in Figure 61. However, the impact of scatterometer information in the KNMI-R1, SIG0 and CTL experiments is broadly similar, and there is no indication that the sigma0 approach is losing information compared to the level 2 retrieval assimilation in these results.

4.2.1. Summary

Only a selection of departure statistics results has been presented here, and there are undoubtably some variations in the results across the different observing systems. However, overall the performance of the level 2 assimilation and sigma0 assimilation is broadly similar for short-range forecasts. In general, as expected, the largest degradations are seen in the No SCATT experiment, but the scatterometer performance in the CTL, SIG0 and KNMI-R1 experiments is similar.

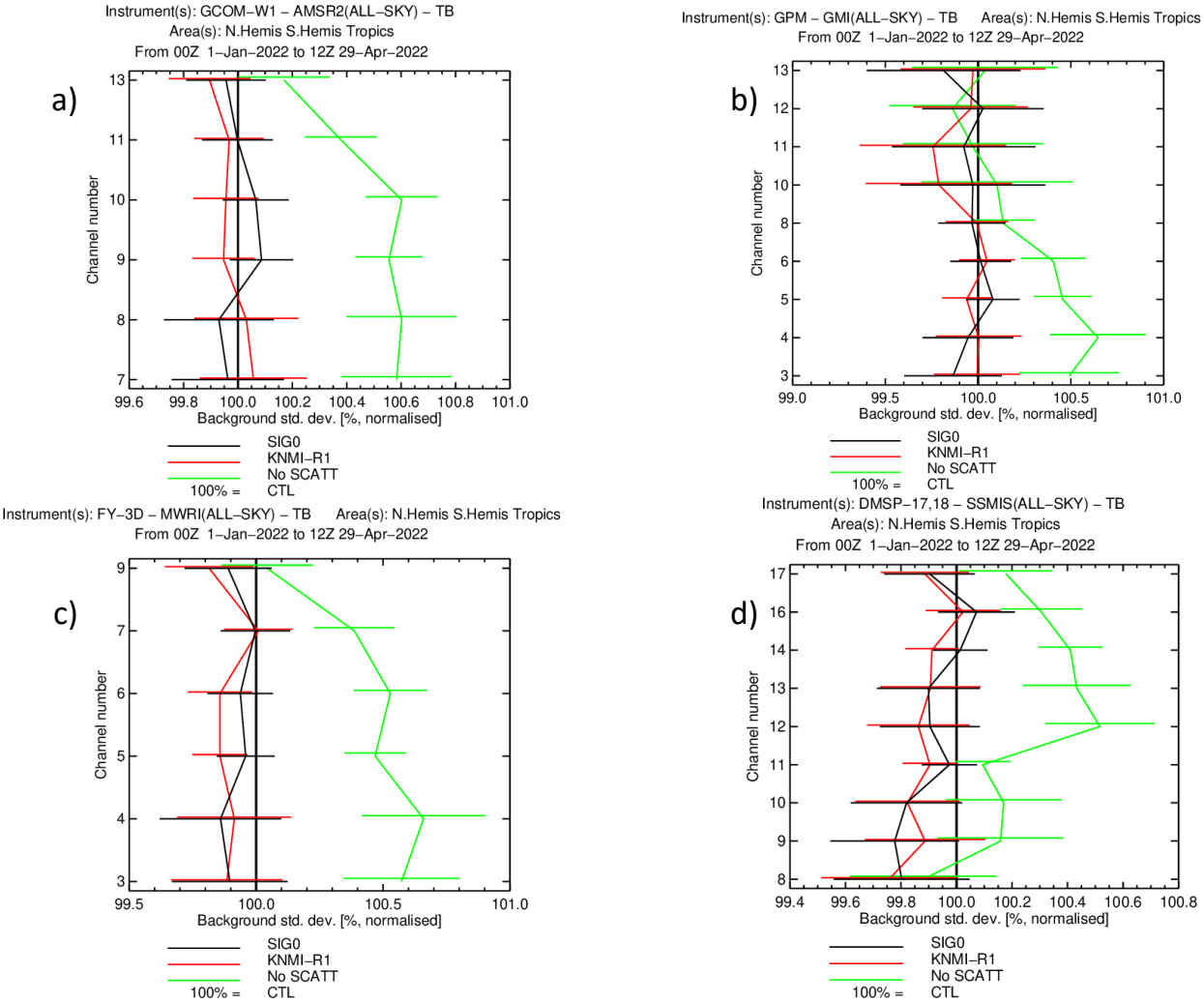

Figure 61: The (o-b) departure statistics for the microwave imagers a) AMSR2, b) GMI, c) MWRI and d) SSMIS. These results are globally averaged and span the period from January 1 to April 29, 2022.

4.3. Verification against operational and own analyses

Verifying against operational analyses can overestimate the impact of datasets already used in operations, which in this case are the CMOD5.n wind retrievals used in the CTL experiment. On the other hand, verifying forecasts against "own analyses" generated during each experiment can also be problematic at short-range because they often penalise increments introduced by the new observations. In fact, verifying against operational and own analyses can provide contradictory results at short-range, and this is why we also look at the (o-b) departure statistics alongside the verification against analyses for short-range forecasts.

Figure 62 and Figure 63 show the change in RMS vector wind forecast errors on pressure levels between 1000 hPa and 200 hPa, verified against own and operational analyses, respectively. The error bars give the 95% confidence interval. The lines are below 0 in these figures indicate that the configuration being tested is better than the CTL experiment. Therefore, Figure 62 appears to show that removing the scatterometer measurements produces a large reduction in the RMS of the vector wind forecast errors (green line), meaning that the scatterometer information in the CTL experiment is degrading the vector wind forecasts. For example, at 1000 hPa in the tropics the RMS is reduced by almost 15% at 12 hours in the No SCATT experiment. However, in Figure 63 the corresponding RMS error is increased by almost 6% meaning an improved forecast impact, clearly illustrating the difficulties in verifying the impact of scatterometers at short-range.

Given the observation departure statistics shown above we can be fairly confident that scatterometers are not degrading the short-range wind forecasts in the CTL experiment, so we give more weight to the verification against operations here. The impact of KNMI retrievals is slightly better than either the CTL and SIG0 experiments at short-range in Figure 63. These improvements with KNMI data are consistent with the lower retrieval noise produced with CMOD7, reducing the size of the increments. In the medium-range, KNMI statistics also tend to be slightly better but the differences are not statistically significant beyond day 1.

Figure 64 shows the change in the fraction change RMS forecast errors relative to the CTL experiment for both the zonal and meridional 10 m winds, verified against operations (0001). Again, it could be argued that KNMI retrievals are providing slightly larger impact than the scatterometer information used in either the CTL and SIG0 experiments, but these improvements are only statistically significant for the first 12 hours. Figure 65 shows the change in mean sea level pressure RMS errors, and the results are neutral after 12 hours. Figure 66 is the change in relative humidity RMS errors on the 1000, 925 and 850 hPa pressure levels. The No SCATT experiment is clearly degraded for day-1 and day-2 in the tropics at 1000 hPa, but beyond day 1 the results are generally neutral.

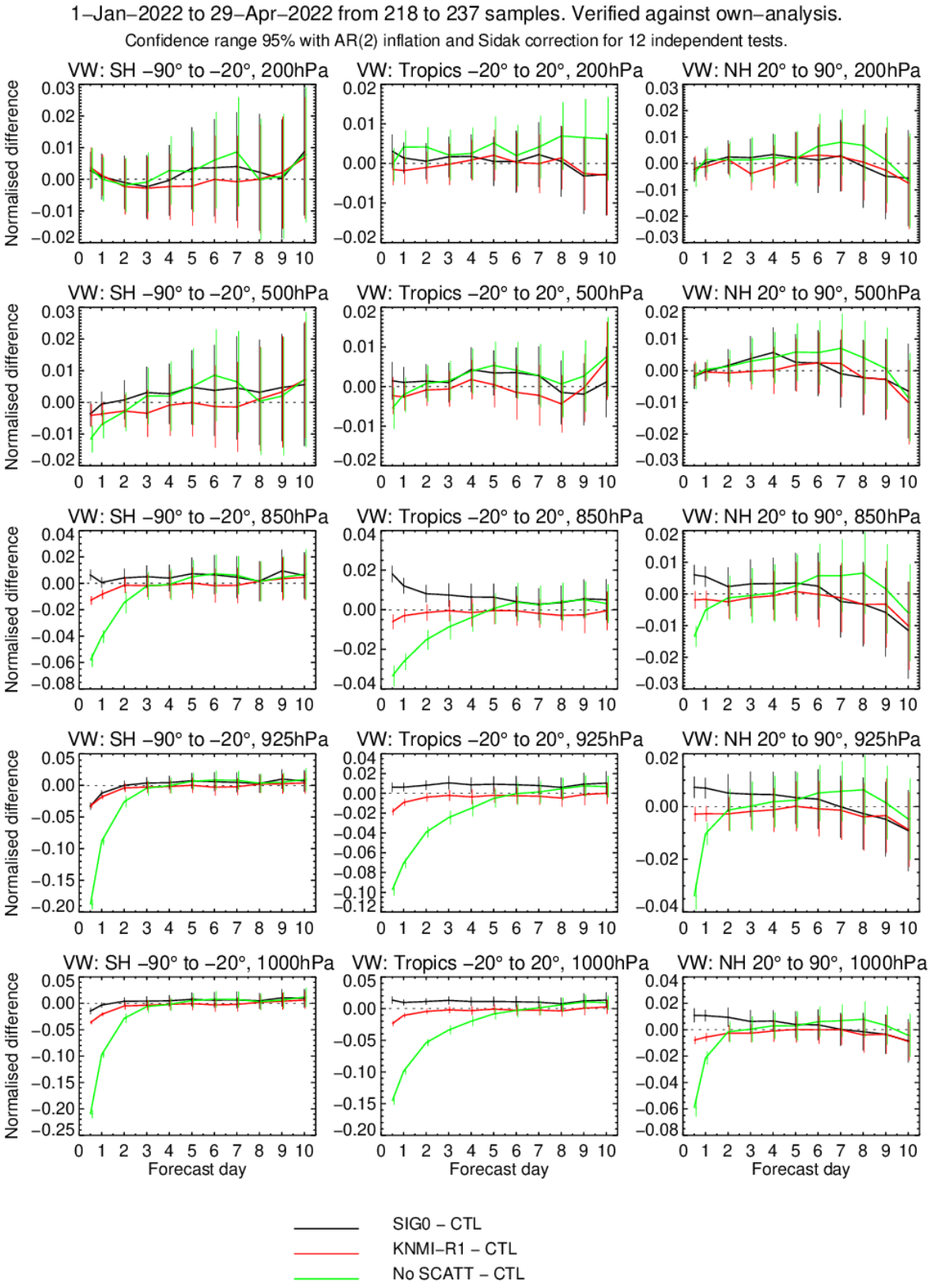

Figure 62: Normalised change in the RMS of vector wind forecast errors on pressure levels as a function of forecast range. The verification is against "own analysis". Below 0 indicates that the RMS forecast error statistics are smaller than in the CTL experiment. The period is from January 1 to April 29, 2022.

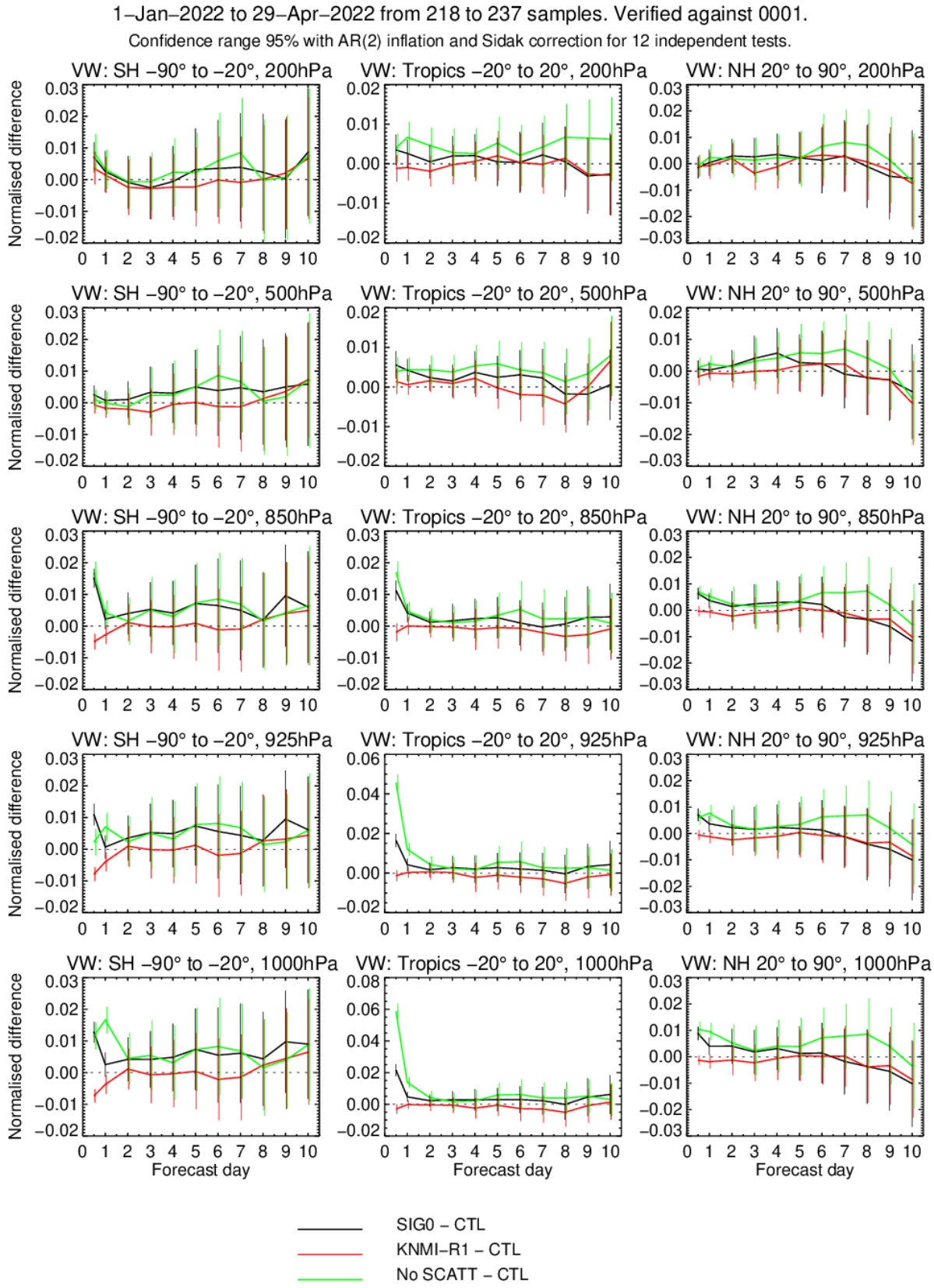

Figure 63: As Figure 62, showing the change in vector wind RMS forecast errors, but verified against operational analyses (0001). Below 0 indicates that the RMS forecast error statistics are smaller than in the CTL experiment.

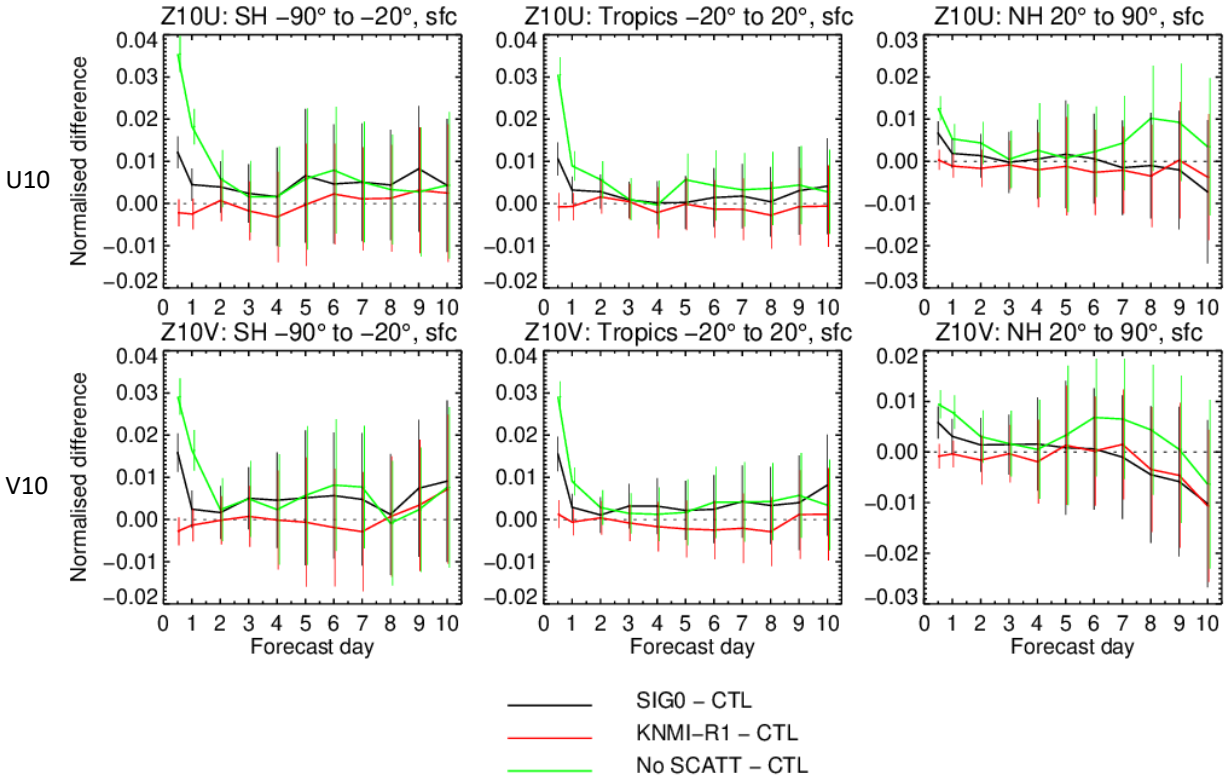

Figure 64: The change in zonal (upper) and meridional (lower) 10 m wind RMS errors as a function of forecast range, verified against ECMWF operations (0001). Below 0 indicates that the RMS forecast error statistics are smaller than in the CTL experiment.

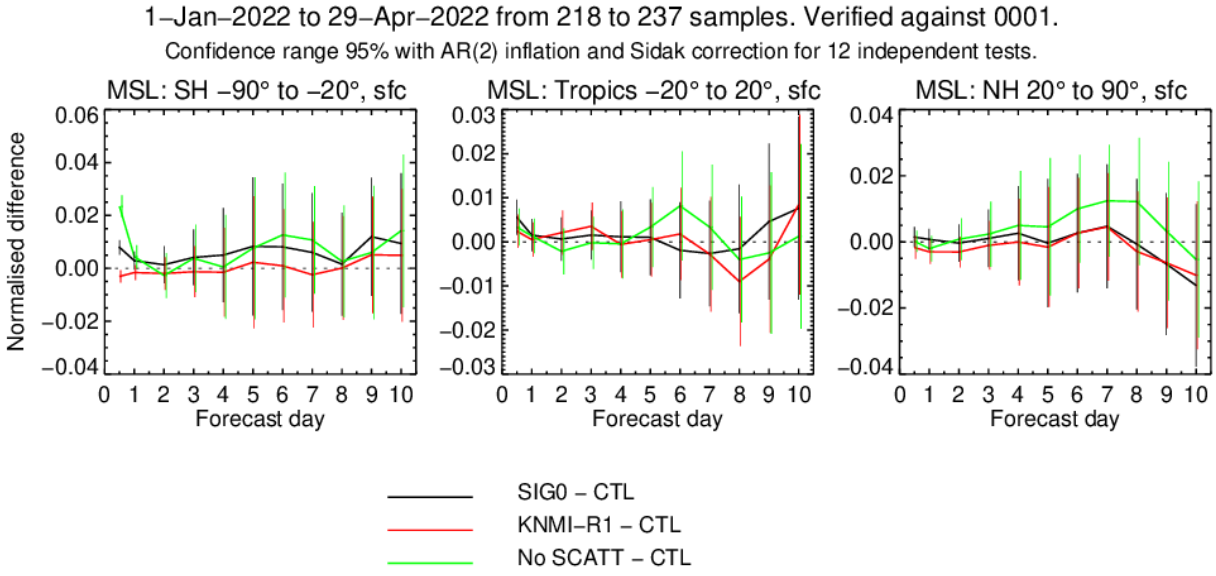

Figure 65: The change in the RMS of the mean sea level pressure errors relative to the CTL experiment. Verification is against ECMWF operations. Below 0 indicates that the RMS forecast error statistics are smaller than in the CTL experiment.

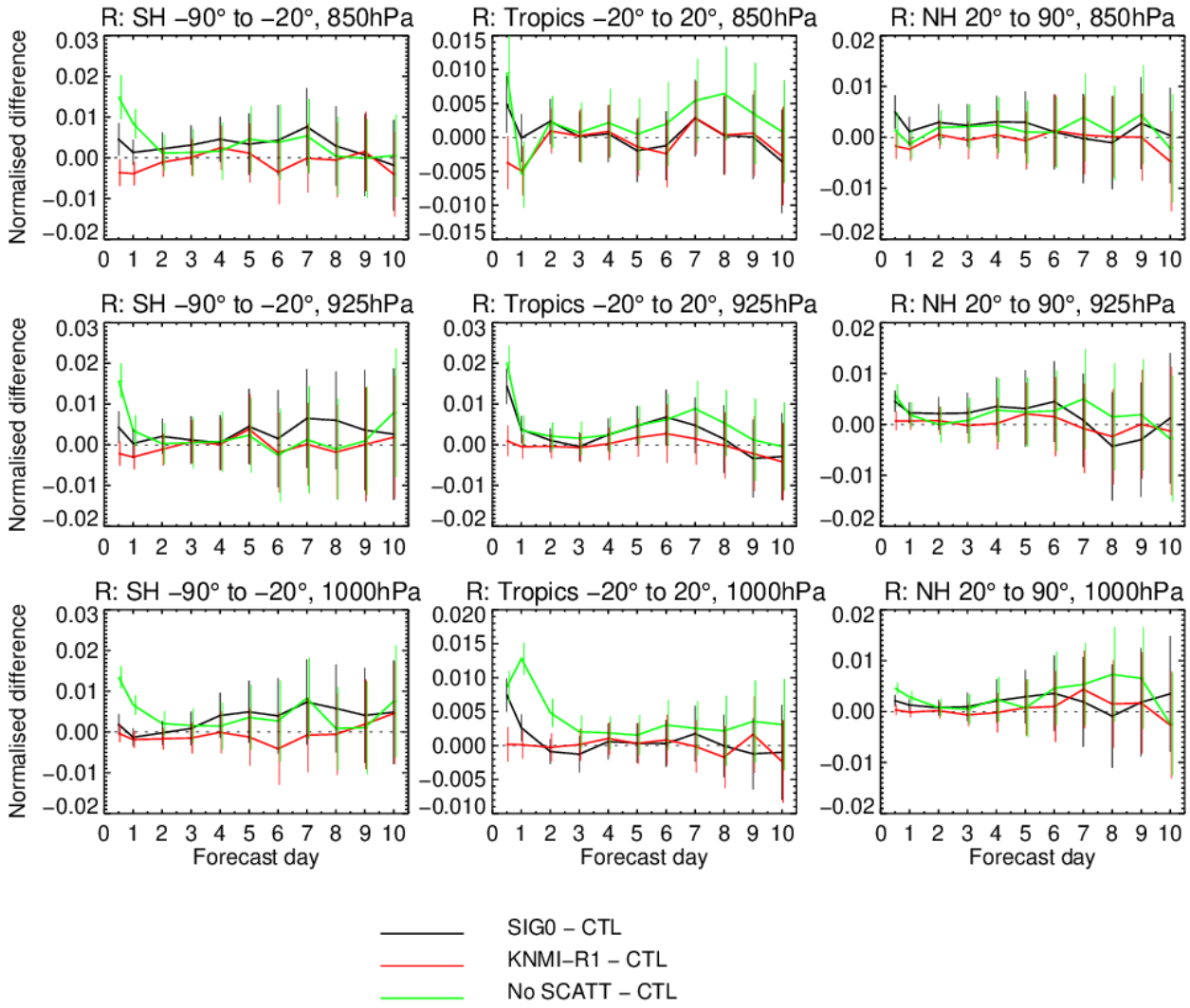

Figure 66: The change in the RMS of the relative humidity errors, given relative to the CTL experiment. The forecasts are verified against ECMWF operations. Below 0 indicates that the RMS forecast error statistics are smaller than in the CTL experiment.

4.4. Verification against observations

In addition to verifying against operational and own analyses, we can also verify these experiments against a trusted set of moored buoy measurements used in the official ECMWF verification package, QUAVER. Figure 67 shows the fractional change in the standard deviation of the 10 m wind speed errors verified against the buoys for the No SCATT experiment when compared to CTL. In the tropics (right panel), there is a clear degradation in the 10 m wind speed of more than 5% at the analysis time, falling to around 1.5% at day 1. The degradation is smaller in the northern hemisphere, around 1% at the analysis time. The corresponding plots for the KNMI-R1 and SIG0 experiments are shown in Figure 68 and Figure 69, respectively. The clear No SCATT degradation in the tropics is effectively reversed in the KNMI and SIG0 experiments recovering the performance of the CTL, indicating that useful wind speed information is being retrieved with both assimilation approaches. The KNMI results are slightly

better in the tropics out to day 2, but the results do not appear to be statistically significant. The SIG0 results appear to be slightly better in the northern hemisphere at the analysis time, but more generally KNMI and SIG0 results appear very similar for longer forecast ranges.

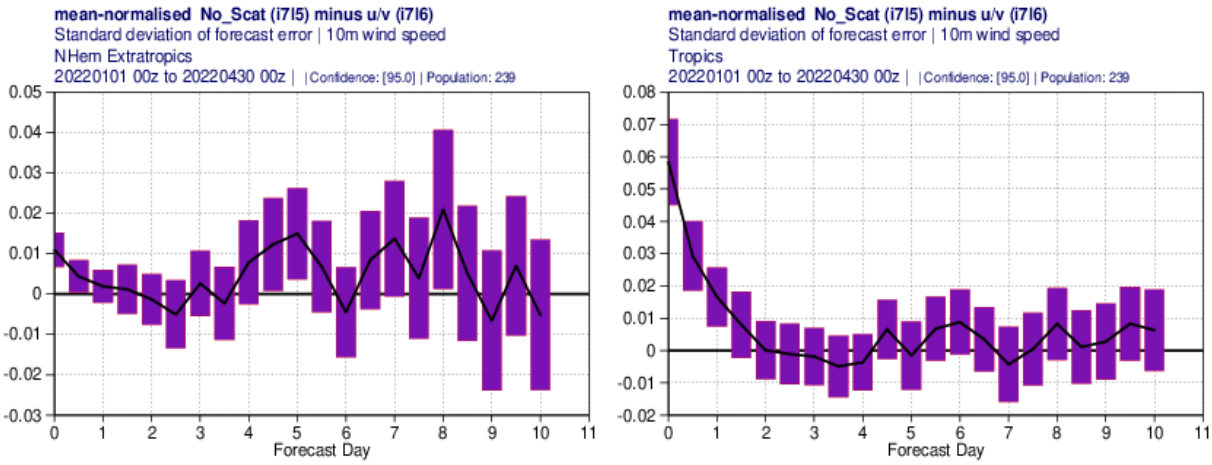

Figure 67: The change in the standard deviation of the 10 m wind speed error given as function of forecast range for the northern hemisphere (left) and tropics (right), comparing the No SCATT to the CTL experiment. Below 0 indicates that the forecast error statistics are better than the CTL.

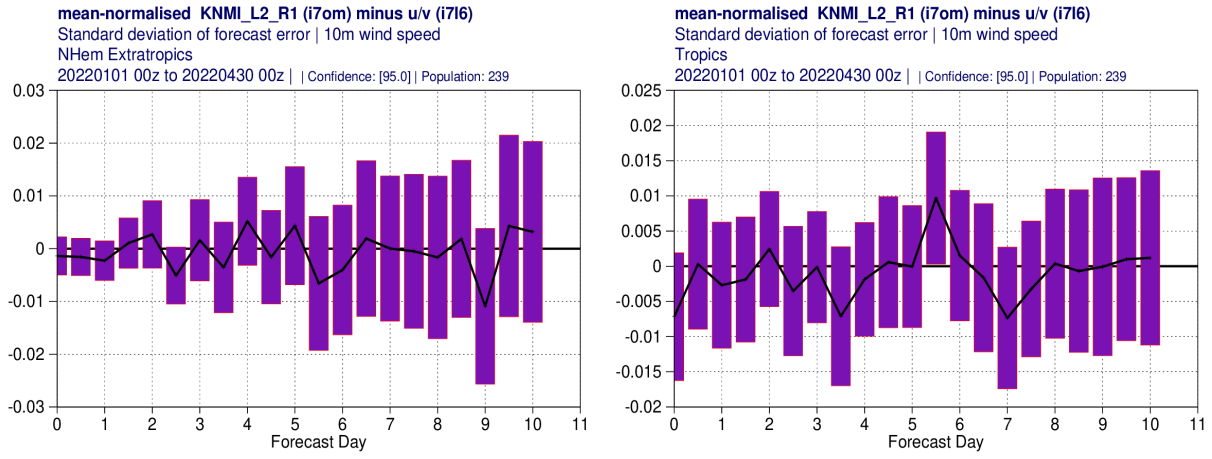

Figure 68: As Figure 67, showing the change in the standard deviation of the 10 m wind speed error given as function of forecast range for the northern hemisphere (left) and tropics (right), but comparing the KNMI-R1 to the CTL experiment. Below 0 indicates that the KNMI-R1 forecast error statistics are better than the CTL.

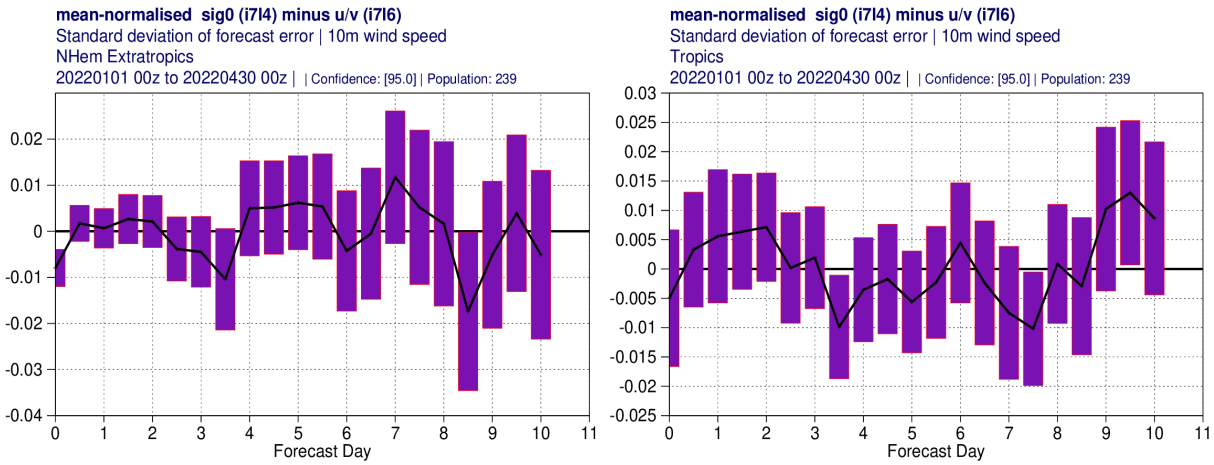

Figure 69: As Figure 67, showing the change in the standard deviation of the 10 m wind speed error given as function of forecast range for the northern hemisphere (left) and tropics (right), but comparing the SIG0 to the CTL experiment. Below 0 indicates that the SIG0 forecast error statistics are better than the CTL.

We have performed a similar analysis for SWH forecast errors verified against buoys, and the general picture is the same, with degradations in the No SCATT experiment largely corrected in both the KNMI and SIG0 experiments. For example, Figure 70 shows the change in standard deviation of the SWH error comparing the SIG0 against the CTL experiment. In the southern hemisphere (lower) we see an improvement relative to the CTL of around 1% out to day 2.5. The results are less clear in the northern hemisphere and tropics.

4.5. Verification against altimeter SWH and wind speed retrievals

Altimeters retrievals provide additional verification datasets for both wind speed and SWH forecasts. We use retrievals from Jason-3 and Sentinel-3A/3B for this verification. No altimeter wind speeds are assimilated in the 4D-Var system, and so they can be considered independent of the 4D-Var analyses and forecasts. The Jason-3 SWH information is the ECMWF wave data assimilation system, but not Sentinel-3A/3B during this period.

Figure 71 shows the standard deviation of the wind speed errors verified against the altimeter retrievals, given as a function of forecast range (hours). In this case, the SIG0, CTL ("U-V" in the figure legend) and KNMI-R1 experiments are compared with the No SCATT, and values above 0 indicate that the error statistics are better than No SCATT. Unfortunately, this verification package does not provide an estimate of statistical significance, but it is clear that the SIG0 experiment performs best at short-range. For example, in the tropics the standard deviation of the (analysis – altimeter retrieval) differences is 4% smaller in the SIG0 experiment than in KNMI-R1 and CTL (a 12% reduction in SIG0 versus 8%). The corresponding SWH scores are shown in Figure 72, where again the SIG0 experiment is best at short-range. The SWH results are more mixed for longer ranges. For example, in the northern

hemisphere the KNMI-R1 SWH results are better than either CTL or SIG0 after about 24 hours. The altimeter verification statistics are clearly encouraging for the sigma0 assimilation, and we are not aware of any reason why verifying with the altimeter retrievals would erroneously penalise the level 2 approach.

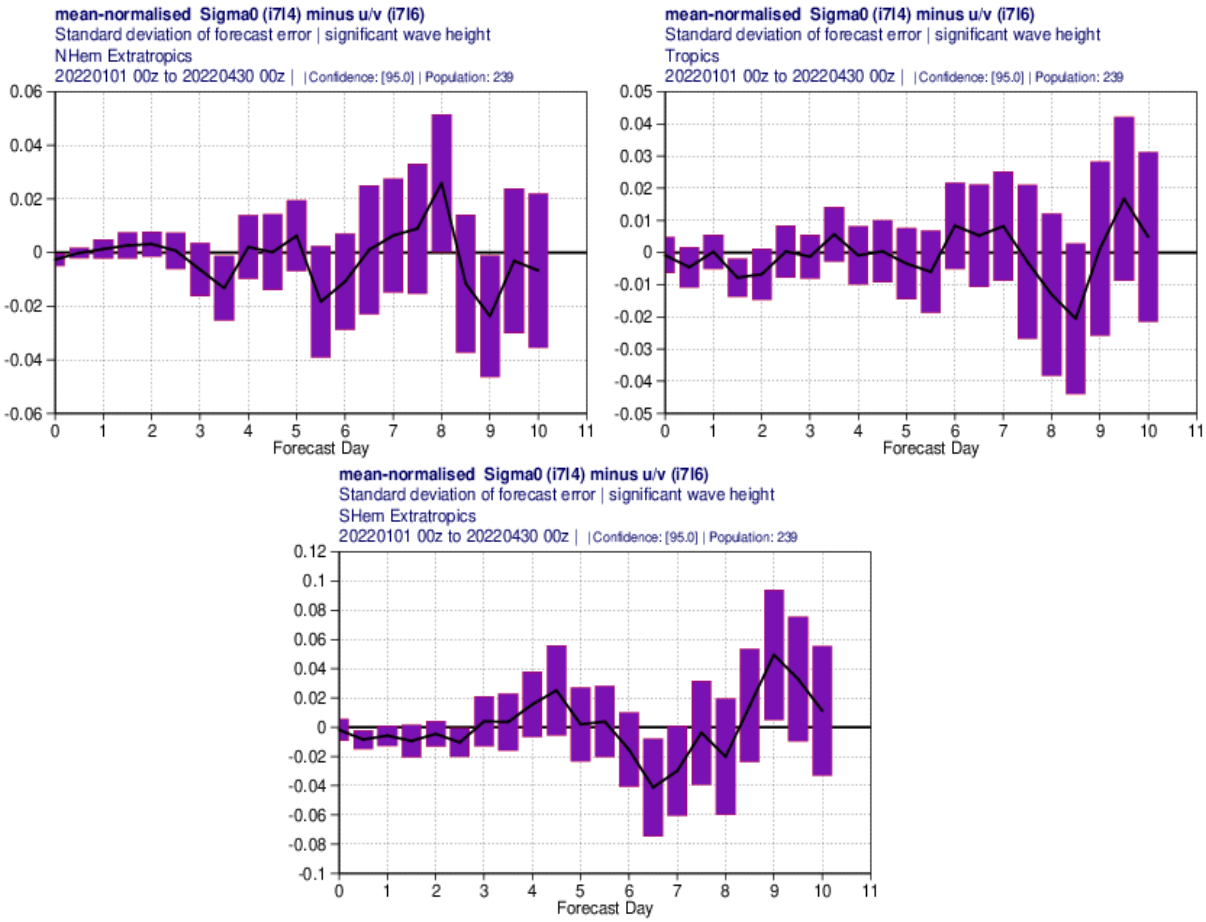

Figure 70: The change in standard deviation of the SWH, comparing SIG0 with the CTL experiment. The verification is against moored buoys. Below 0 indicates the SIG0 has better error statistics than CTL.

4.6. Sigma0 as a function of stress

One of the advantages of developing forward operators based on ANNs is that we can develop and test multiple versions, using on different physical variables as inputs. For example, one sigma0 forward operator developed in Section 1.4.6 computes sigma0 as a function of surface stress, and we have tested this version in OSEs. This is of interest because in a previous phase of this project we were considering the direct assimilation of ambiguous surface stress values derived indirectly from the observed sigma0's, via the wind retrieval. Here we are effectively reversing the approach, assimilating sigma0 given as a function of stress, $\boldsymbol{\tau}$.

Neglecting ocean currents, the surface stress vector can be written as,

$$\boldsymbol{\tau} = \rho C_D |u(z_l)| \mathbf{u}(z_l)$$

where $\mathbf{u}(z_l)$ is the two-dimensional wind vector on the lowest model level, $|u(z_l)|$ is the wind speed, ρ is the air density at the sea surface and C_D is the drag coefficient [18]. Therefore, use of stress in the forward operator explicitly introduces a dependence on the atmospheric density at the surface, similar to the use of stress equivalent winds. It also implicitly introduces a dependence on the local sea state via the roughness length in the drag coefficient. We have found that the use of stress reduces the biases in the (o-b) departure statistics, as illustrated in Figure 73, where the magnitudes of positive and negative biases are reduced. Most of the improvement in the biases appears to be related to the inclusion of density. This result is promising, but it does not appear to translate into an improved forecast impact.

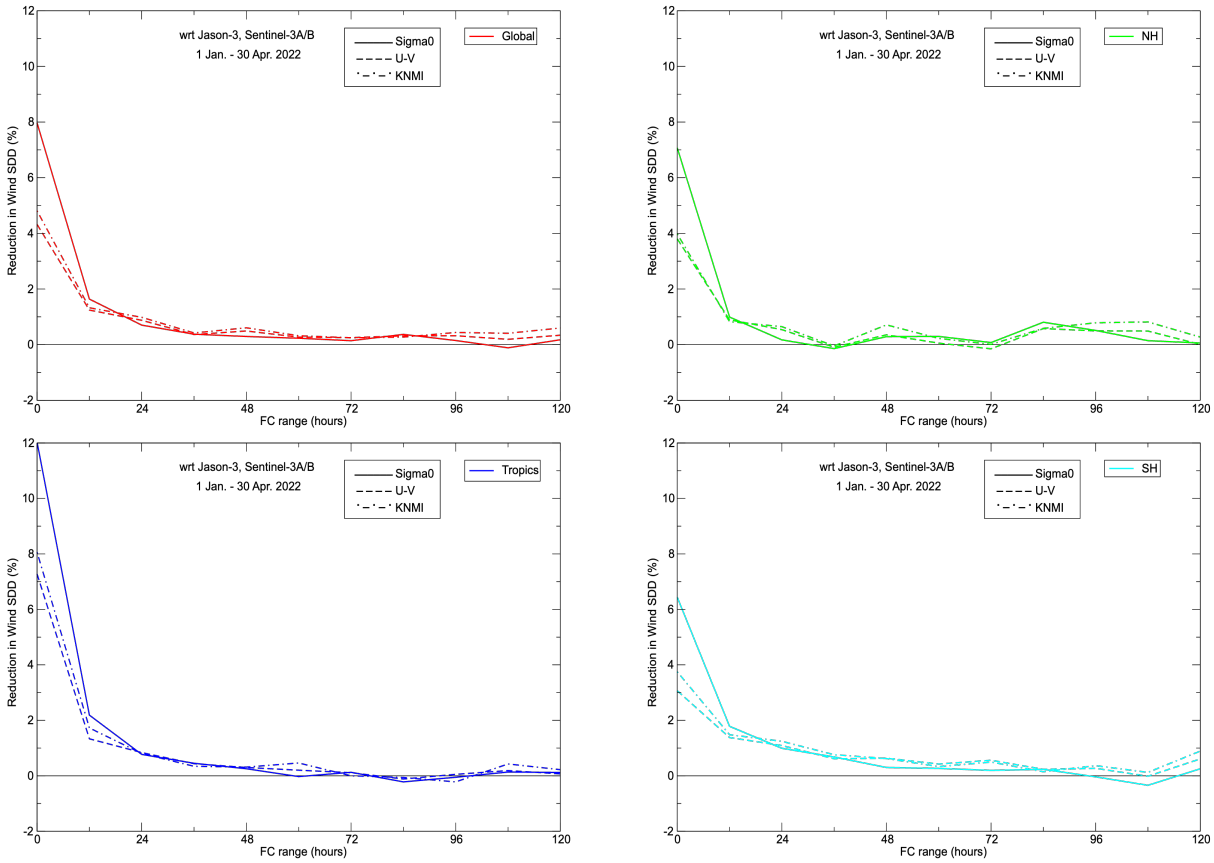

Figure 71: The reduction in standard deviation of the wind speed forecast errors verified against altimeter retrievals as a function of forecast range (hours). The comparisons are against the No SCATT experiment, and values above 0 indicate that the configuration is better than No SCATT: Global (top left), northern hemisphere (top right), tropics (bottom left), southern hemisphere (bottom right).

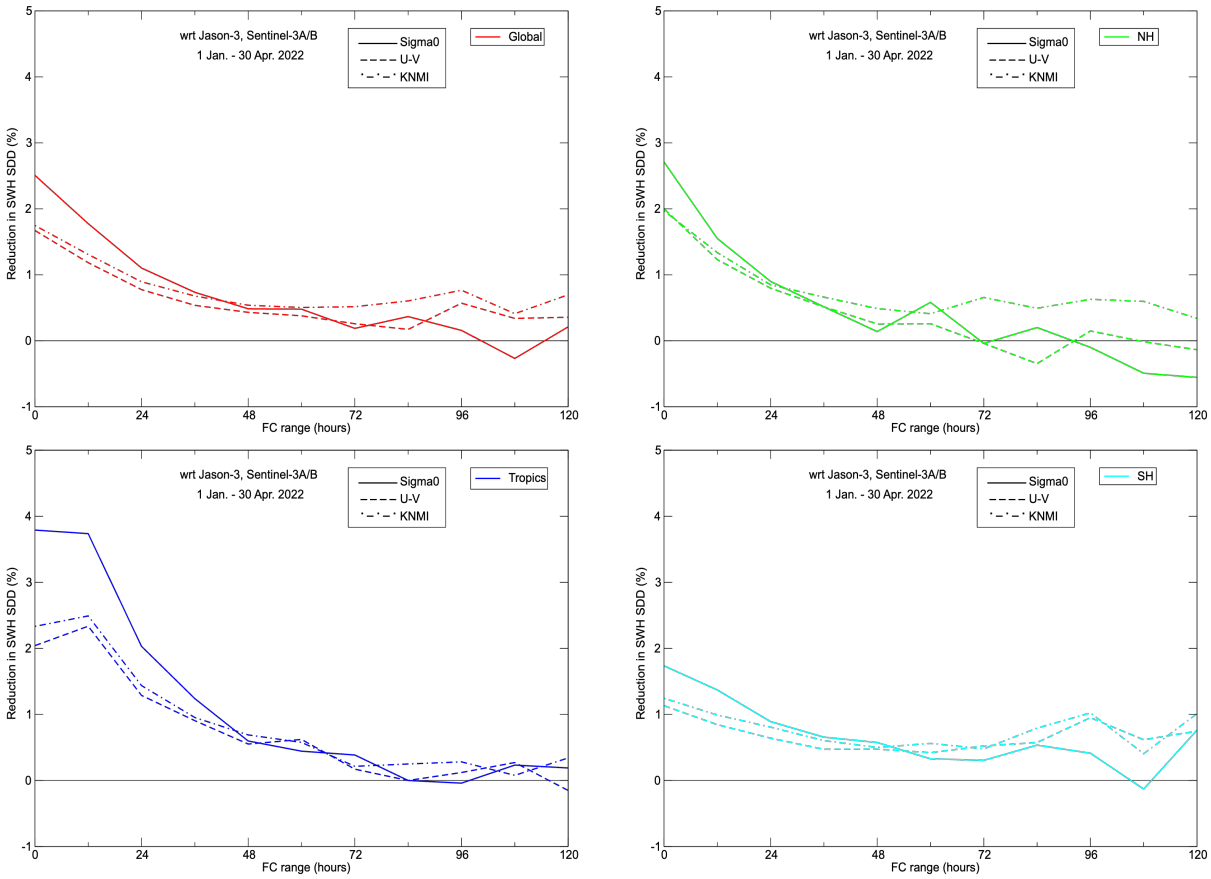

Figure 72: The reduction in standard deviation of the SWH forecast errors verified against altimeter retrievals as a function of forecast range (hours). The comparisons are against the No SCATT experiment and values above 0 indicate that the configuration is better than No SCATT: Global (top left), northern hemisphere (top right), tropics (bottom left), southern hemisphere (bottom right).

4.7. Tropical Cyclone Impact

The impact of assimilating retrieved scatterometer winds or backscatter (over the ocean) on tropical cyclone analysis and forecast errors has been also assessed. The period under evaluation so far (January-February 2022) is not ideal for tropical cyclones since not many storms usually occurs. To have a larger number of case studies, a new set of OSEs, with the same configuration explained in Section 4.1, was run over the period from the 1 April 2022 until 31 October 2022. This period covers the Atlantic and north-east Pacific tropical cyclone season with more cases to compute the statistics.

The following OSEs were run:

- **CTL**: The control experiment, assimilating Metop-B and C ASCAT L2 wind retrieval information produced with CMOD5.n at ECMWF during the assimilation experiments as part of the pre-processing step.
- **No SCATT**: As CTL, but not assimilating the ASCAT winds.

- **SIG0**: Assimilating Metop-B and C sigma0 values over the ocean using the ANN approach, that computes sigma0 as a function of the neutral equivalent 10 m wind vector (plus geometry: angle of incidence/azimuthal).

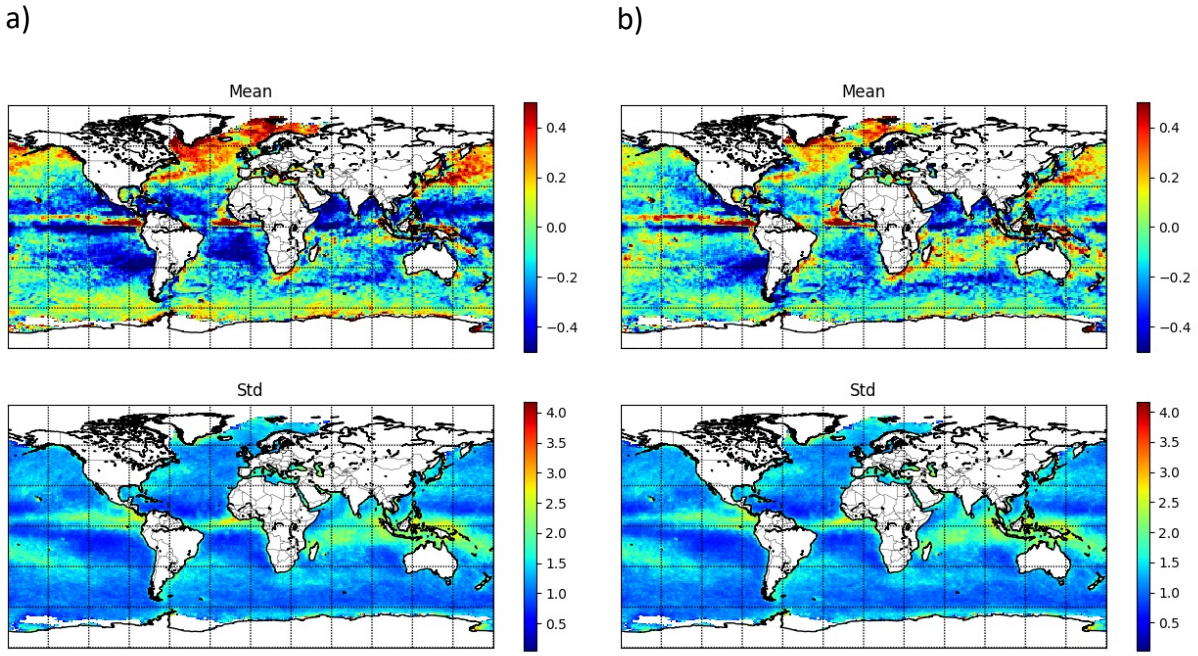

Figure 73: The spatial maps of the mean (upper) and standard deviation (lower) of the (o-b) sigma0 departure statistics for a) the "standard" forward operator based on neutral equivalent 10 m winds and b) using the surface stress values. The statistics are computed from January 1 – April 29, 2022.

The tropical cyclones position error and central pressure error were computed for all the common storms that occurred globally in the three experiments. For this evaluation we consider the *CTL* (similar to the operational assimilation) the reference experiment and we assess the change in performances if ASCAT data are assimilated as backscatter (*SIG0*) instead of wind or if we do not assimilate ASCAT data over the ocean at all (*No SCAT*).

Figure 74 shows the average position error (left-hand panels) and intensity error (right-hand panel) as function of the forecast step for *CTL* (black line), *SIG0* (red line), *No SCAT* (blue line). The top panels present the absolute error, the bottom ones the normalized differences of the *SIG0* and *No SCAT* versus *CTRL*. Negative values indicate a reduction in error as a result of assimilating ASCAT backscatter or not assimilating ASCAT data at all.

SIG0 and *No SCAT* show higher position error than the *CTL* at analysis time and out to 48-hour forecasts, with the *SIG0* experiment having a larger error than the *No SCAT*. After that the signal is not statistically significant (i.e. the confidence intervals cross the zero line). An impact on day-1 to day-3 forecasts is typically related to the local steering flow, while an impact from day-5 to day-7 is related to hemispheric skill.

The signal is opposite for the central pressure error. The assimilation of backscatter instead of wind (*SIG0*), is reducing the intensity error up to 3% at analysis time and 2.5% at 12-hour forecast. A 2% improvement is seen at day-2. The impact is neutral on the other forecast steps. Removing ASCAT observations (*No SCAT*) is slightly increasing the central pressure error, but the signal is not statistically significant.

Previous studies performed to assess the impact on tropical cyclones of other observing systems have showed that the impact depends a lot on the model horizontal resolution used to run the OSEs [11].

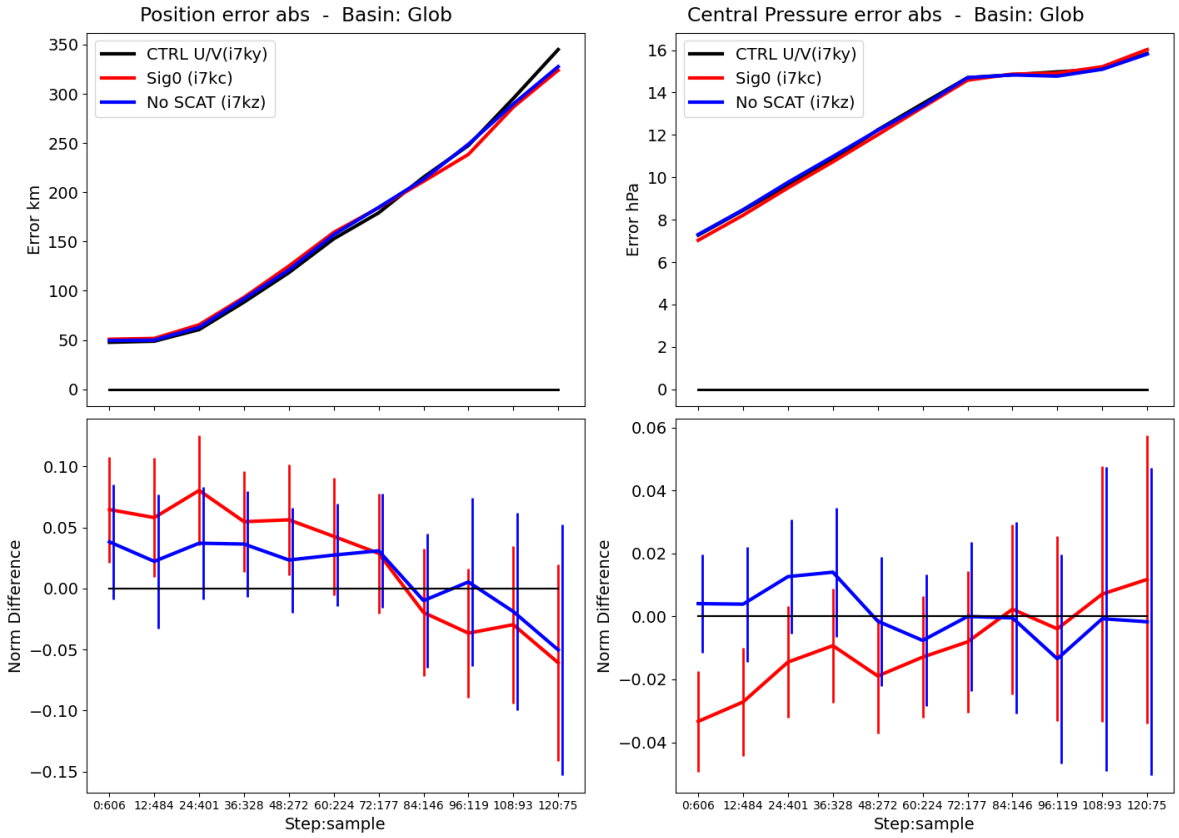

Figure 74: The impact on tropical cyclone from assimilating scatterometer observations over the ocean as either surface winds or backscatter. Mean absolute position errors (km) on the top-left plot and minimum sea level pressure error (hPa) on the top-right plot for the CTL (in black), Sig0 (in red), No SCAT (in blue) for the period from 1 April 2022 to 31 October 2022. In the bottom panels the lines are the normalised difference of the two OSEs minus CTL (Sig0 minus CTL in red, No SCAT minus CTRL in blue, with 95% confidence interval plotted as error bars: negative values indicate a reduction in error from assimilating ASCAT as backscatter or for not assimilating ASCAT at all. On the x-axes the forecast step (from 0 to 120 hours) and the number of cases is displayed. The verification is done against observation derived best estimate of TC position and central pressure.

4.8. Summary

The ASCAT scatterometer observations over the ocean from Metop-B and Metop-C have been assimilated as either ambiguous wind vectors or as backscatter (sigma0) values using the ANN forward operator developed in Section 1 (*SIG0*). Two versions of the Level 2 wind products have been tested. The first follows the operational approach used at ECMWF, using CMOD5.n in pre-processing step of the 4D-Var (*CTL*). The second uses the selected wind retrievals provided by KNMI, based on CMOD7 and their 2D-Var ambiguity removal approach (KNMI-R1). However, note that the KNMI wind retrievals are assimilated as "neutral equivalent" winds rather than the recommended "stress equivalent" winds.

The short-range forecast departure statistics for ASCAT indicate that the KNMI retrievals have lower noise than the CMOD5.n retrievals currently used operationally at ECMWF. This is despite interpreting the KNMI information as neutral equivalent winds in the experiments. This is a potentially useful result when planning ahead for the assimilation EPS-SG SCA data. The sigma0 approach improves the short-range departure statistics for altimeter SWH retrievals when compared to the level 2 approaches and the *No SCATT* experiment. The largest improvements are found in the tropics. This is the clearest example where sigma0 assimilation appears better than the level 2 approach, but we do not see this improvement across all observing systems. For example, the SATOB wind departures below 700 hPa are best with the KNMI wind retrievals, with both the sigma0 approach and CMOD5.n degrading the departures near the surface. This is a known issue in the ECMWF system.

We see a clear degradation in the microwave image departure statistics in the No SCATT experiment, but the differences between *SIG0*, KNMI-R1 and *CTL* are small, indicating that the assimilation of sigma0 is able retrieve similar wind information content to the level 2 approaches.

The verification against operational and own analyses supports the KNMI data impact in the short-range, but the differences in the forecast error statistics are not generally statistically significant beyond day-2 when assessing surface and upper-air winds, humidity and surface pressure information. In general, the scatterometer impact on these is small and so seeing the differences that arise from the assimilation approach is challenging. However, there is no clear evidence that the sigma0 assimilation is significantly worse than the wind experiments.

The verification of 10-m wind speed forecasts against moored buoys in the *No SCATT* experiment illustrates the importance of scatterometer measurements more clearly than verification against analyses, particularly in the tropics. The impact of the retrieved wind and the sigma0 is similar, with both compensating for the degradation in the *No SCATT* experiment. There is some improvement in the SWH forecast error statistics out to day 2.5 in the southern hemisphere when assimilating sigma0. The verification against altimeter wind speed and SWH retrievals is also encouraging for the sigma0 assimilation. The analysis and short-range forecasts from the *SIG0* experiment are more consistent with the altimeter retrievals than the wind assimilation experiments, but this improvement is not sustained for longer forecasts. It should be noted that the altimeter verification does not include statistical significance tests.

Assimilating sigma0 as a function of stress improves the (o-b) biases, but this does not appear to translate into improved forecast scores.

The impact of assimilating sigma0 on tropical cyclone forecasts has been assessed for the period 1 April 2022 until 31 October 2022. The assimilation of sigma0 produces a statistically significant degradation of the position errors out to day-2. The central pressure error statistics are improved out to 12 hours. We have found previously that tropical cyclone impact can be very sensitive the resolution of the forecast model.

As is often the case with the forecast impact experiments, both positive and negative signals are mixed when considering a range of factors like forecast-range, meteorological variables and verification method. However, overall there is no clear evidence that sigma0 assimilation does not work, and that the scatterometer measurements have to be assimilated as level 2 wind products over the ocean. Indeed, aspects of these results are clearly positive with respect to the wind assimilation and they would support further research work in this area.

5. Summary and Recommendations

In this study, we have used artificial neural networks (ANNs) to develop new forward operators that enable the direct assimilation scatterometer sigma0 (backscatter) observations. The central question we have tried address is whether scatterometer information has to be assimilated as ambiguous Level 2 products, or whether developments in data assimilation methodology in recent years mean that the direct assimilation of sigma0 is now a viable approach. Overall, we have demonstrated in extended observing system experiments (OSEs) that the direct assimilation of sigma0 is now a viable assimilation approach, with a comparable performance to the Level 2 assimilation. In fact, the verification against altimeter wind speed and significant wave height (SWH) retrievals suggest that the sigma0 approach may be better. However, this is not the case for verification against own and operational analyses, and overall we believe that further work would be required to demonstrate conclusively if sigma0 assimilation can be superior to Level 2 assimilation before, for example, using this new approach operationally at ECMWF.

The study has been completed in just over a year and it has encompassed a diverse range of activities. These include the development and testing of the new scatterometer ANN forward models, the implementation of the new operators in the ECMWF 4D-Var data assimilation system and performing the first extended forecast impact experiments with ASCAT sigma0 values. (We have also developed a new altimeter wind speed retrieval as part of this work - see below.). Although the main study questions have been addressed, there are aspects of the work that could be improved with more time. In the context of the forward model development these improvements include;

- The performance of the ANN sigma0 operator is good belew 20 m/s, but it is not as good as established GMFs, like CMOD7, above 20 m/s. More generally, the ANN performance outside its training space can be unphysical, and CMOD7 is a more accurate simulation code for general applications.
- The input to the ANN is the neutral equivalent 10 m wind vector (u, v). There may be advantages training the operator to ingest the wind components parallel and perpendicular to the beam direction.
- Currently, we have trained the ANN with single sigma0 values at a given location. We have not tried to train against the triplet at that location. Could that provide any additional benefit?

A number of ANN sigma0 forward models have been tested, but only two versions have been tested in the NWP system. Significantly, the flexibility of the ANN architecture has enabled us to adapt existing tangent-linear and adjoint code, developed initially as gravity wave emulator, when implementing the sigma0 code in the ECMWF NWP system.

The sigma0 assimilation experiments have been successful, but there are areas that could be improved:

- The uncertainty model used in the sigma0 assimilation is relatively crude. The error is assumed to be the largest of either 10 % of the observed values or 1.6 dB. For context, a Gaussian 1 m/s wind speed error maps to around 1.2 dB. Further sensitivity tests to the assumed sigma0 uncertainty values would be useful.
- We have not attempted any bias correction of the sigma0 values, but there are clearly large spatial variations in the (o-b) biases. It would be useful to implement the sigma0 assimilation within a variational bias correction scheme.
- The results assimilating sigma0 as a function of stress, rather than as a function of neutral equivalent wind, appears to improve the (o-b) biases. This promising result should be pursued further. In addition, parallel work at ECMWF coupling the ocean current to atmospheric system appears to have a big impact on the scatterometer impact. This coupling work should be combined with both the sigma0 and the sigma0 as a function of stress assimilation approach.
- Quality control for sigma0. To date, we have tried to use the basic quality control used for the ambiguous wind assimilation. We have not explored whether this can be improved for sigma0.

In addition to the scatterometer work, we have also developed a new ANN based wind speed retrieval for altimeter measurements. Unlike the scatterometer work, which is based on "used" data that had passed quality control checks needed to be assimilated, the altimeter training required more emphasis on quality control and "data cleaning". A number of ANN configurations have been tested, but we recommend the retrieval based on the Ku-band backscatter and SWH, together with the square of off-nadir angle. The performance of this retrieval is comparable with the existing operational product.

To conclude, we have explored many questions as part of this study. Perhaps most significantly, the viability of the direct assimilation of scatterometer backscatter (sigma0) has been clearly demonstrated. We have also exploited the flexibility of the ANN approach when developing the sigma0 forward models. Overall, the results are very encouraging but further research and development will be needed to move to sigma0 assimilation in routine operational applications.

References

1 Abadi, M., Agarwal, A., Barham, P., Brevdo, E., Chen, Z., Citro, C., Corrado, G. S., Davis, A., Dean, J., Devin, M., Ghemawat, S., Goodfellow, I., Harp, A., Irving, G., Isard, M., Jozefowicz, R., Jia, Y., Kaiser, L., Kudlur, M., Levenberg, J., Mané, D., Schuster, M., Monga, R., Moore, S., Murray, D., Olah, C., Shlens, J., Steiner, B., Sutskever, I., Talwar, K., Tucker, P., Vanhoucke, V., Vasudevan, V., Viégas, F., Vinyals, O., Warden, P., Wattenberg, M., Wicke, M., Yu, Y., and Zheng, X., TensorFlow: Large-scale machine learning on heterogeneous systems (2015), Software available from tensorflow.org

2 Abdalla, S. (2012), Ku-Band Radar Altimeter Surface Wind Speed Algorithm. *Marine Geodesy*, 35:sup1, 276-298. https://doi.org/10.1080/01490419.2012.718676

3 Aires, F, Weston, P, de Rosnay, P, Fairbairn, D. (2021), Statistical approaches to assimilate ASCAT soil moisture information – I. Methodologies and first assessment. *Q J R Meteorol Soc.*, 1823–1852. https://doi.org/10.1002/qj.3997

4 Chollet, F. et al. (2015), Keras. GitHub. Retrieved Sep 22, 2022 from https://github.com/fchollet/keras

5 Cornford, D., Nabney, I. T., and Ramage, G. (2001), Improved neural network scatterometer forward models. *J. Geophys. Res.*, 106(C10), 22331– 22338. https://doi.org/10.1029/2000JC000417

6 Courtier, P., Thépaut, J-N. and Hollingsworth, A. (1994), A strategy for operational implementation of 4D-Var, using an incremental approach. *Q.J.R. Meteorol. Soc.*, 120: 1367-1387. https://doi.org/10.1002/qj.49712051912

7 De Chiara, G. (2013), *Preparation for the Assimilation of ASCAT-B Scatterometer Winds*. ECMWF Research Department Memorandum, RD13-294.

8 De Chiara, G., Abdalla, S., Isaksen, L. and Healy, S. (2022), *Characterization of Ocean Surface Roughness in NWP*. Task 4 report, Contract No. EUM/CO/18/4600002207/SLi https://www-cdn.eumetsat.int/files/2020-06/pdf_ss_nwp_winds_task1.pdf

9 De Chiara, G., English, S., Janssen, P. A. E. M. and Bidlot, J.-R. (2016), *ASCAT Ocean Surface Wind Assessment*. ECMWF Technical Memorandum 776. https://doi.org/10.21957/6wqfjq02c

10 De Chiara G., Isaksen, L. and English, S. (2018), *ECMWF Support for EPS/ASCAT – Ocean Wind Assessment*. Final Report Contract No. EUM/CO/15/4600001497/JF. https://www.eumetsat.int/media/42715

11 De Chiara, G., Magnusson, L., Rennie, M., Abdalla, S., and Healy, S. (2023), *The Contribution of Aeolus to the Prediction of Extreme Weather Events*, Contract Report to the European Space Agency, ESA ESTEC contract No. 4000134449/20/NL/FF/tfd, Ref: AE-TN-ECMWF-GS-175, Version 1.2, 16 June 2023.

12 de Kloe, J., Stoffelen, A. and Verhoef, A. (2017), Improved Use of Scatterometer Measurements by Using Stress-Equivalent Reference Winds. *IEEE Journal of Selected Topics in Applied Earth Observations and Remote Sensing*, 10(5), 2340-2347. https://doi.org/10.1109/JSTARS.2017.2685242

13 Dinnat, E., English, S., Prigent, C., Kilic, L., Anguelova, M., Newman, S., Meissner, T., Boutin, J., Stoffelen, A., Yueh, S., Johnson, B., Weng, F., and Jimenez, C. (2023), PARMIO: A reference quality model for ocean surface emissivity and backscatter from the microwave to the infrared. *Bull. Amer. Meteor. Soc.*, 104, E742–E748. https://doi.org/10.1175/BAMS-D-23-0023.1

14 Donelan, M. A., and Plant, W. J. (2009), A threshold for wind-wave growth. *J. Geophys. Res.*, 114, C07012. https://doi.org/10.1029/2008JC005238

15 ECMWF (2020), *Data Handling System*. ECMWF web page. Retrieved Sep 22, 2022 from https://www.ecmwf.int/en/computing/our-facilities/data-handling-system

16 ECMWF (2023a), *IFS Documentation CY48R1 - Part VII: ECMWF Wave Model*. ECMWF web page. doi: 10.21957/cd1936d846 , Retrieved Jul 11, 2023. https://www.ecmwf.int/en/elibrary/81373-ifs-documentation-cy48r1-part-vii-ecmwf-wave-model

17 ECMWF (2023b), *Parameter Database*. ECMWF web page, Retrieved Nov 16, 2023. https://codes.ecmwf.int/grib/param-db/

18 Edson, J. B., Jampana, V., Weller, R. A., Bigorre, S. P., Plueddemann, A. J., Fairall, C. W., Miller, S. D., Mahrt, L., Vickers, D. and Hersbach, H. (2013), On the exchange of momentum over the open ocean. *J. Phys. Oceanogr.*, 43, 1589–1610. https://doi.org/10.1175/JPO-D-12-0173.1

19 Freilich, M. H. and Challenor, P. G. (1994), A new approach for determining fully empirical altimeter wind speed model functions. *J. Geophys. Res.*, 99, 25051-25062. https://doi.org/10.1029/94JC01996

20 Geer, A. J., Lonitz, K., Weston, P., et al. (2018), "All-sky satellite data assimilation at operational weather forecasting centres. *Q. J. R. Meteorol. Soc.*, 144, 1191– 1217. https://doi.org/10.1002/qj.3202

21 Glazman, R. and Greysukh, A. (1993), Satellite altimeter measurements of surface wind. *J. Geophys. Res.*, 98, 2475-2483. https://doi.org/10.1029/92JC02659

22 Gourrion, J., Vandemark, D., Bailey, S., Chapron, B., Gommenginger, G. P., Challenor, P. G. and Srokosz, M. A. (2002), A two-parameter wind speed algorithm for Ku-band altimeters. *J. Atmos. Oceanic Technol.*, 19, 2030-2048. https://doi.org/10.1175/1520-0426(2002)019<2030:ATPWSA>2.0.CO;2

23 Hatfield, S., Chantry, M., Dueben, P., Lopez, P., Geer, A. and Palmer, T. (2021), Building tangent-linear and adjoint models for data assimilation with neural networks. *Journal of Advances in Modeling Earth Systems*, 13, e2021MS002521. https://doi.org/10.1029/2021MS002521

24 Hersbach, H. (2007), *Preparation for assimilation of surface-wind data from ASCAT at ECMWF*. ECMWF Research Department Memorandum R60.9/HH/075.

25 Hersbach, H. (2008), *CMOD5-N: A C-band geophysical model function for equivalent neutral wind*. ECMWF Technical Memorandum 554. https://doi.org/10.21957/mzcfm6jfl

26 Hwang, P., Teague, W., Jacobs, G. and Wang, D. (1998), A statistical comparison of wind speed, wave height and wave period derived from satellite altimeters and ocean buoys in the Gulf of Mexico region. *J. Geophys. Res.*, 103, 10451-10468. https://doi.org/10.1029/98JC00197

27 Isaksen, L. and Stoffelen, A. (2000), ERS scatterometer wind data impact on ECMWF's tropical cyclone forecasts. *IEEE Transactions on Geoscience and Remote Sensing*, 38(4), 1885-1892. https://doi.org/10.1109/36.851771

28 Isaksen, L. and Janssen, P. A. E. M. (2004), Impact of ERS scatterometer winds in ECMWF's assimilation system, *Q. J. R. Meteorol. Soc.*, 130, 1793-1814. https://doi.org/10.1256/qj.03.110

29 Janssen, P. A. E. M., Wallbrink, H., Calkoen, C. J., van Halsema, D., Oost, W. A., and Snoeij, P. (1998), VIERS-1 scatterometer model. *J. Geophys. Res.*, 103(C4), 7807– 7831. https://doi.org/10.1029/97JC02911

30 Laloyaux, P., M. Balmaseda, D. Dee, K. Mogensen, P. A. E. M. Janssen (2016), CERA: A coupled data assimilation system for climate reanalysis. *Q. J. R. Meteorol. Soc.*, 142, 65-78. https://doi.org/10.1002/qj.2629

31 Lillibridge, J., Scharroo, R., Abdalla, S., and Vandemark, D. (2014), One- and two-dimensional wind speed models for Ka-band altimetry. *J. Atmos. Oceanic Technol.*, 31:3, 630-638. https://doi.org/10.1175/JTECH-D-13-00167.1

32 Peubey, C. and McNally, A.P. (2009), Characterization of the impact of geostationary clear-sky radiances on wind analyses in a 4D-Var context. *Q. J. R. Meteorol. Soc.*, 135: 1863-1876. https://doi.org/10.1002/qj.500

33 Stoffelen, A. and Anderson, D. (1997), "Ambiguity removal and assimilation of scatterometer data". *Q. J. R. Meteorol. Soc.*, 123: 491-518. https://doi.org/10.1002/qj.49712353812

34 Stoffelen, A., Verspeek, J. A., Vogelzang, J. and Verhoef, A. (2017), The CMOD7 geophysical model function for ASCAT and ERS wind retrievals. *IEEE Journal of Selected Topics in Applied Earth Observations and Remote Sensing*, 10 (5), 2123-2134. https://doi.org/10.1109/JSTARS.2017.2681806

35 Thépaut, J., Hoffman, R. N., & Courtier, P. (1993), "Interactions of dynamics and observations in a four-dimensional variational assimilation", *Monthly Weather Review*, *121*(12), 3393-3414. Retrieved Sep 16, 2022, from https://journals.ametsoc.org/view/journals/mwre/121/12/1520-0493_1993_121_3393_iodaoi_2_0_co_2.xml

36 Witter, D. L. and Chelton, D. B. (1991), A Geosat altimeter wind speed algorithm and a method for altimeter wind speed algorithm development. *J. Geophys. Res.*, 96, 8853-8860. https://doi.org/10.1029/91JC00414

37 Wu, J. (1999), On wave dependency of altimeter sea returns – weak fetch influence on short ocean waves. *J. Atmos. Oceanic Technol.*, 16, 373-378. https://doi.org/10.1175/1520-0426(1999)016<0373:OWDOAS>2.0.CO;2